FACULTE DES SCIENCES AIN CHOCK
UNIVERSITE HASSAN II DE CASABLANCA

MOHAMMED VI POLYTECHNIC UNIVERSITY

Light-by-light scattering in the ATLAS detector at the LHC

Mohamed Reda Mekouar

A dissertation submitted in partial fulfilment of the requirements for the Master's degree
Computing and Scientific Instrumentation for High Energy Physics (IISPHE),
Specialisation Area of High Energy Physics

Supervisor: Prof. Driss Benchekroun
Prof. Abdelouahed El Fatimy
Prof. Yahya Tayalati
Dr. Hicham Atmani

Casablanca, September 5, 2023

Dedicatory

To my mother Dounia without whom I would have never ever been the man I am today.

Abstract

This memorandum reports the study of the light-by-light scattering process, $\gamma\gamma \rightarrow \gamma\gamma$, in Pb+Pb collisions at the ATLAS experiment. The study uses 2.2 nb^{-1} of integrated luminosity collected in 2015 and 2018 at $\sqrt{s_{NN}} = 5.02\ TeV$. Light-by-light scattering candidates are selected in events with two photons produced exclusively, each with transverse energy $E_T^\gamma > 2.5\ GeV$ and pseudorapidity $|\eta| < 2.37$, diphoton invariant mass above 5 GeV, and small diphoton transverse momentum and acoplanarity. After applying all selection criteria, 97 candidate events are observed for a background expectation of 27 ± 5 events. The integrated and differential cross sections are measured and compared with theoretical predictions. The measured fiducial cross section is 121.53 ± 17.03 (stat.) ± 9.51 (syst.) ± 3.83 (lumi.) nb. The observed excess of events over the expected background has a significance of 12.45 standard deviations. The diphoton invariant mass distribution is used to set limits on the production of axion-like particles. This result provides the most stringent limits to date on axion-like particle production for masses in the range 6–100 GeV. Cross sections above 2 to 200 nb are excluded at the 95% CL in that mass interval.

Keywords: Heavy ions, photons scattering, ALPs

Résumé

Ce mémoire relate l'étude du processus de diffusion lumière par lumière, $\gamma\gamma \rightarrow \gamma\gamma$, dans les collisions Pb+Pb à l'expérience ATLAS. L'étude utilise 2.2 nb^{-1} de luminosité intégrée collectée en 2015 et 2018 à $\sqrt{s_{NN}} = 5.02\ TeV$. Les candidats à la diffusion lumière par lumière sont sélectionnés dans les événements avec deux photons produits exclusivement, chacun avec une énergie transverse $E_T^{\gamma} > 2.5\ GeV$ et une pseudorapidité $|\eta| < 2.37$, ainsi qu'un moment transverse des diphotons et une acoplanarité faibles. Après application de tous les critères de sélection, 97 événements candidats sont observés pour une estimation du bruit de fond de 27 ± 5 événements. Les sections efficaces intégrées et différentielles sont mesurées et comparées aux prédictions théoriques. La section efficace fiduciale mesurée est de 121.53 ± 17.03 (stat.) ± 9.51 (syst.) ± 3.83 (lumi.) nb. L'excès d'événements observé par rapport au bruit de fond attendu a une signification de 12.45 écarts-types. La distribution de la masse invariante du diphoton est utilisée pour établir des limites sur la production de particules de type axion. Ce résultat fournit les limites les plus contraignantes à ce jour sur la production de particules de type axion pour des masses dans la plage de 6 à 100 GeV. Les sections efficaces supérieures à 2 à 200 nb sont exclues à 95 % de niveau de confiance dans cet intervalle de masse.

Acknowledgement

I would like to express my sincere appreciation to Professor **Driss Benchekroun** for his invaluable support, guidance, and expertise throughout my academic journey and this project. His unwavering commitment to academic excellence and dedication to my growth and development have been truly inspiring. I am grateful for his insightful feedback, which has greatly enriched my work. I consider myself fortunate to have learned from Prof. **Driss Benchekroun** and am truly grateful for his contributions to my academic and personal growth.

I am also thankful to Professors **Abdelouahed El Fatimy** and **Yahya Tayalati** for their extensive knowledge and guidance. Their contributions have played a pivotal role in shaping my research. I am especially grateful to Dr. **Hicham Atmani** for his constant support, encouragement, timely guidance, and mentorship throughout this course of this project. His dedication to excellence has been truly inspiring, and his expertise and constructive feedback have significantly enhanced the quality of my work.

I am grateful to the faculty members and staff of both **University Hassan II of Casablanca** and **Mohammed VI Polytechnic University** for their contributions to my education and their dedication to creating a nurturing academic environment.

Furthermore, I would like to express my heartfelt appreciation to my colleagues, Mr. **Amine Meskar**, Miss **Ghizlane Ezzobayr**, and Mr. **Yassin Bimgdi**. Their support, collaboration, and enthusiasm have made this journey rewarding and fulfilling. I am grateful for the stimulating discussions and valuable exchange of ideas. The camaraderie and friendship we have developed have created a supportive and inspiring environment that has made the journey more enjoyable. I am also grateful to all my other colleagues for their contributions, encouragement, and for making this journey enriching and memorable.

My deepest gratitude goes to my beloved mother, Ms. **Dounia Masdouri**, who has fought so much for me, and my beautiful sister, Mrs. **Sobha Adnan**, who has always been a role model for me, along with her small family (husband and children), they have brought immense love and support into my life. I am deeply grateful for my family's unwavering love, support, and guidance throughout my academic journey. They have been my pillars of strength, providing the motivation and confidence to pursue my goals.

I am also grateful to my friends, Mr. **Othman Ghafiri**, Mr. **Mohamed Amine Kartout**, and Mr. **Zakaria Chafchaouni**, who have been not only friends but brothers to me. They have been my constant source of support, offering unwavering encouragement and shared experiences that inspire and motivate me. I am grateful for their understanding during challenging times and their ability to bring joy and balance to my life.

I am grateful to all the individuals mentioned above for their contributions and support, which have been crucial to the success of this work. Without their guidance and belief in me, this achievement would not have been possible.

Contents

Introduction

The study of light-by-light scattering, a process where two photons interact and transform back into two photons, has captivated scientists for many years. In classical electromagnetism, such interaction is not expected to occur in a vacuum [1], but within the framework of quantum electrodynamics (QED), a component of the Standard Model (SM) of particle physics, the interaction of two photons is indeed possible [2] through a loop involving charged fermions or $W^{\pm}$ bosons. Besides investigating this interaction, various experiments have sought to detect the effects of new physics beyond the Standard Model (BSM) that could mediate light-by-light scattering. Studies of light-by-light scattering have been conducted using photon scattering in the Coulomb field of a nucleus (Delbrück scattering) [3–6] and in the photon splitting process [7]. These experiments employ electromagnetic fields to observe light-by-light scattering, and additional background studies and related experiments are detailed in Ref. [8, 9].

Currently, high-energy colliders are the only environments where the Schwinger limit of $10^{18}\ V \cdot m^{-1}$ is exceeded [10]. At the Large Hadron Collider (LHC), the electromagnetic fields between colliding hadrons are sufficiently strong to generate high-energy virtual photon fluxes. These virtual photons can then interact with each other, allowing for light-by-light scattering. In 2016, the ATLAS collaboration reported the first direct evidence of high-energy light-by-light scattering without the application of additional electromagnetic fields [11]. This experiment utilized Pb+Pb collisions, involving the collision of lead ion beams at the LHC. The electromagnetic fields surrounding the colliding lead ions can be treated as quasi-real photons with low virtuality [12–14], and these photons can collide with each other in what is known as an ultra-peripheral collision (UPC) [15, 16]. Therefore, the ATLAS observation signifies that the LHC was effectively functioning as a photon-photon ($\gamma\gamma$) collider. Figure 1 illustrates the Feynman diagram depicting such an event. Importantly, light-by-light scattering can occur in collisions involving charged particles in general. Further developments in measuring light-by-light scattering at the LHC are discussed in subsection 1.10.3.

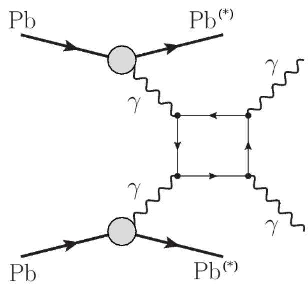

Figure 1: Feynman diagram of SM light-by-light scattering in Pb+Pb collisions. The potential electromagnetic excitation of the lead ion is denoted by $(*)$ [17].

In this measurement, the final-state signature of interest is the exclusive production of two photons, where the diphoton final state is measured in the detector surrounding the Pb+Pb interaction region, and the incoming Pb ions survive the EM interaction, possibly with an EM excitation [18], denoted by $(*)$. Consequently, two low-energy photons are expected to be detected with no additional activity in the central detector. In particular, no reconstructed charged-particle tracks originating from the Pb+Pb interaction point are anticipated.

The ATLAS and CMS collaborations provided the initial direct evidence of light-by-light scattering in Pb+Pb UPC at the LHC [11, 19]. This evidence was based on Pb+Pb data collected in 2015, with a center-of-mass energy of $\sqrt{s_{NN}} = 5.02\ TeV$. Building on this, the ATLAS collaboration conducted a new analysis using a data sample from Pb+Pb collisions in 2018, which had 3.5 times more integrated luminosity at the same center-of-mass energy. The observation measurement made by the ATLAS collaboration yielded a significance of 8.2σ [20]. This analysis followed the approach proposed in Ref. [21] and utilized the same methodology as the previous measurements.

In this memorandum, we present a measurement of the fiducial cross-section for Pb+Pb $(\gamma\gamma) \rightarrow$ Pb$(*)$ + Pb$(*)$ $\gamma\gamma$ production at a center-of-mass energy of $\sqrt{s_{NN}} = 5.02\ TeV$. This measurement is based on a combination of Pb+Pb collision data recorded during Run 2 in 2015 and 2018 by the ATLAS experiment. The combined data set corresponds to an integrated luminosity of 2.2 nb^{-1}.

In the first chapter, we introduce the theoretical framework that underpins our study, with a primary focus on the standard models. Understanding the elementary particles involved in our process (photons, leptons, etc.) and the key interactions, such as Quantum Electrodynamics (QED), is crucial. We also discuss the limitations of this model, which motivate our search for phenomena beyond it. Next, we delve into Heavy Ion collisions, followed by a closer examination of Ultra Peripheral Collisions, as they hold significant importance for our study. Finally, we conclude the chapter by providing a more detailed explanation of the light-by-light process and presenting relevant previous results.

In the second chapter, our primary focus is on the experimental setup required to study our process. We start by discussing the acceleration chain within particle accelerators and colliders in general, providing an overview of the LHC (Large Hadron Collider) and offering a detailed explanation. Then, we shift our attention to the ATLAS experiment, where we delve into its major components in depth, with a particular emphasis on those relevant to our study, such as the electromagnetic calorimeter.

Finally, in the third chapter, we discuss the data analysis conducted on both the data and Monte Carlo (MC) samples for our process and its background. We begin by focusing on the cut-flow and major selections applied, followed by an examination of the systematic uncertainties. These steps allow us to generate kinematic distributions that provide insights into the agreement between our model and the data. Additionally, we present the fiducial cross section and differential cross sections obtained through bin-by-bin unfolding. Then, we delve into the fit performed using a profile likelihood function with the TRExFitter software, highlighting the main results of this statistical study with a particular emphasis on the significance. Lastly, we employed the same TRExFitter framework to execute a profile likelihood fit on data by employing instead an ALP hypothetical signal. This was done to set limits on the cross section for the production of these Axion-Like Particles.

Chapter 1

Theoretical Framework

1.1 Introduction

The Standard Model of Particle Physics [22][23][24] is a widely accepted theoretical framework that offers a comprehensive understanding of the behavior of subatomic particles. It encompasses elementary particles, including fermions (quarks and leptons), as well as bosons, and successfully describes three of the four fundamental interactions: the strong force, the weak force, and the electromagnetic force. However, it has not been able to incorporate the gravitational force into its framework.

1.2 Elementary Particles

The Standard Model is the currently accepted theory of particle physics, which states that all observable matter in the universe is composed of 12 fundamental fermions: six quarks and six leptons. These fermions possess half-integer spin and are governed by Pauli's exclusion principle [25], which prohibits two fermions in a system from occupying the same quantum state. In addition, the Standard Model includes 12 vector bosons that mediate the fundamental forces between fermions, along with the Higgs boson, which imparts mass to particles. While the Standard Model has successfully explained numerous natural phenomena, it does not incorporate the force of gravity.

1.2.1 Fermions

Fermions [26] are a type of elementary particle that make up the building blocks of matter. They have a property called spin, which is a measure of their intrinsic angular momentum. Fermions are subject to the Pauli exclusion principle, which states that no two fermions in a system can have the exact same set of quantum numbers. This principle leads to the behavior of fermions in materials such as metals, where their exclusion from occupying the same quantum state leads to the phenomenon of electron degeneracy pressure, which helps to support the material against gravitational collapse. Fermions are divided into two main groups: quarks and leptons. Quarks are the fundamental building blocks of protons and neutrons, which in turn make up atomic nuclei. Leptons include particles such as electrons and neutrinos, which are fundamental to the structure of atoms and the interactions between them.

Quarks

There are six types of quarks [27] (u, d, c, s, t, and b) with charges that are fractions of the charge of an electron (±1/3e and ±2/3e). Quarks are affected by strong interaction and have a color charge that distinguishes them from one another. They cannot exist freely and are confined in hadrons due to an effect similar to the screen effect. The model originally contained three quark flavors (u, d, and s) until the discovery of the charm quark (c) in 1974 and later the bottom quark (b) in 1977. The top quark (t) was observed in 1996. Quarks are arranged in pairs (u, d), (c, s) and (t, b).

Leptons

The family of leptons is a group of elementary particles that are categorized as fermions and have a spin of 1/2. The leptons do not interact via the strong nuclear force, which is one of the four fundamental forces of nature.

The leptons include electrons (e), muons (μ), tauons (τ), and their corresponding neutrinos (ν), each with their own antiparticle. The electron is the lightest lepton, and it is a negatively charged particle that orbits around the nucleus of an atom. Muons and tauons are heavier and short-lived particles that can be created in high-energy collisions. They both have the same charge as an electron and decay quickly into other particles.

The neutrinos are neutral leptons that have almost no mass and can pass through matter without interacting. Neutrinos come in three flavors, corresponding to the three charged leptons (electron, muon, and tauon). When they interact with matter, they can change flavor and transform into each other. Neutrinos are produced in a variety of astrophysical and nuclear processes, and their study has provided important insights into the properties of matter and the evolution of the universe.

Generation	Type	Flavor	Symbol	Mass [GeV]	Charge
First generation	Lepton	Electron	e^-	$0.511x10^{-3}$	-1
		Electron Neutrino	ν_e	$< 2x10^{-9}$	0
	Quark	up	u	$2.2x10^{-3}$	2/3
		down	d	$4.7x10^{-3}$	-1/3
Second generation	Lepton	Muon	μ^-	0.106	-1
		Muon Neutrino	ν_μ	$< 0.19x10^{-3}$	0
	Quark	charm	c	1.275	2/3
		strange	s	0.104	-1/3
Third generation	Lepton	Tauon	τ^-	1.78	-1
		Tau Neutrino	ν_τ	$< 18.2x10^{-3}$	0
	Quark	top	t	171	2/3
		bottom	b	4.2	-1/3

Table 1.1: The list of fermions constituting the matter in the SM and their characteristics [28].

1.2.2 Bosons

Elementary bosons play a significant role in our understanding of fundamental interactions in the universe. Among them, there are 12 known gauge bosons: the photon, 8 gluons, and the $W^{\pm}$ and Z^0 bosons. The latter two were discovered at CERN in 1983 [29, 30], expanding our knowledge of particle physics.

Another noteworthy boson is the Higgs boson, which was detected at CERN in 2012[31]. It possesses unique characteristics as a scalar boson with spin-0, and its discovery shed light on the mechanism responsible for giving mass to other particles.

Bosons, in general, serve as mediators or carriers of the fundamental interactions governing the universe. They facilitate the exchange of energy and momentum between particles involved in electromagnetic, weak, and strong interactions.

In the realm of quantum physics, interactions occur through the exchange of particles. Gauge bosons, or interaction bosons, have a crucial role in conveying forces between particles, embodying the intricate nature of our understanding of the fundamental laws of nature.

1.3 The 3 fundamental interactions in the Standard Model

The three fundamental interactions - electromagnetic, weak, and strong - play a crucial role in our understanding of the behavior of particles and their interactions. The electromagnetic interaction is responsible for the attraction or repulsion between electrically charged particles. It has an infinite range because the photon, the carrier particle of this interaction, is massless. This means that charged particles can interact with each other even if they are very far apart. In atoms, the electromagnetic interaction is responsible for the cohesive force that binds electrons to the nucleus, forming stable atoms.

The weak interaction is responsible for processes that change one type of particle into another. For example, it causes beta decay, where a neutron in a nucleus is transformed into a proton, emitting an electron and a neutrino in the process. The weak interaction has a very short range, about one hundredth of a femtometer, and is mediated by the massive gauge bosons $W^{\pm}$ and Z^0.

The strong interaction acts between particles that have a color charge, such as quarks and gluons, which are found inside hadrons like protons and neutrons. It is responsible for the strong force that holds the nucleus of an atom together. The strong interaction is mediated by the eight types of massless gluons, which are exchanged between quarks and are responsible for confining quarks within hadrons. The range of the strong interaction is also very short, about a femtometer.

Interaction	Gauge boson	Mass [GeV]	Charge
electromagnetic	photon (γ)	0	electrical
strong	8 gluons (g)	0	colours (r, g, b)
weak	Z^0	$\sim$91.2	weak isospin
	$W^{\pm}$	$\sim$80.4	

Table 1.2: The list of gauge bosons and the interactions they mediate [28].

1.4 Electromagnetic interaction: QED (Quantum ElectroDynamics)

The electromagnetic interaction, which occurs between charged particles, is widely recognized as one of the most extensively studied interactions in physics. James Clerk Maxwell made significant contributions to our understanding of this interaction during the 19th century through his formulation of Maxwell's equations [32]. It an infinite range, enabling it to act over any distance, while its strength is determined by the charge of the particles and the separation between them. The exchange of virtual photons serves as a crucial concept in describing the interaction between charged particles.

Quantum Electrodynamics (QED) [33], a quantum field theory rooted in the principles of quantum mechanics and incorporating the relativistic Lagrangian formalism, provides a framework for comprehending and calculating the electromagnetic interaction. Within QED, the U(1) symmetry group, specifically the U(1) gauge symmetry, assumes a fundamental role in its formulation and is closely associated with the conservation of electric charge.

The Lagrangian $\mathcal{L}$ that describes the equation for a free elemental charged fermion with a rest mass m, which is represented by the field ψ, can be expressed as follows:

$$\mathcal{L} = \bar{\psi}(x)(i\gamma^{\mu}\partial_{\mu} - m)\psi(x) \tag{1.1}$$

where γ^{μ} are the Dirac matrices, $\bar{\psi} = \psi\gamma^{0}$ is the Dirac adjoint. Under the transformation $\psi \to e^{-i\theta(x)}\psi$ corresponding to the abelian symmetry group U(1), the Lagrangian becomes:

$$\mathcal{L}' = \bar{\psi}(x)\left[(i\gamma^{\mu}\partial_{\mu} - m + \gamma^{\mu}\left(\partial_{\mu}\theta(x)\right)\right]\psi(x) \tag{1.2}$$

The principle of local gauge invariance imposes the replacement of the partial derivative by a covariant derivative, since the new Lagrangian $\mathcal{L}'$ is not a gauge invariant anymore:

$$D_{\mu}\psi(x) \to [D_{\mu}\psi(x)]' = e^{-i\theta(x))}D_{\mu}\psi(x) \tag{1.3}$$

$$D_{\mu} = \partial_{\mu} + iqA_{\mu} \tag{1.4}$$

where q is the electric charge and A_{μ} is a static field that transforms under U(1) as follows:

$$A_{\mu} \to A'_{\mu} = A_{\mu} + \frac{1}{q}\partial_{\mu}\theta(x) \tag{1.5}$$

In order to allow the propagation of the gauge field, a kinetic term must be added. The simplest gauge-invariant corresponding term is the following:

$$\mathcal{L}_{\text{propagation}} = -\frac{1}{4}F_{\mu\nu}F_{\mu\nu} \qquad \text{where} \qquad F^{\mu\nu} = \partial_{\mu}A_{\nu} - \partial_{\nu}A_{\mu} \tag{1.6}$$

Finally, we obtain the expression of the Lagrangian of quantum electrodynamics:

$$\begin{aligned}
\mathcal{L}_{\text{QED}} &= \bar{\psi}(x)\left(i\gamma^{\mu}D_{\mu} - m\right)\psi(x) - \frac{1}{4}F_{\mu\nu}F^{\mu\nu} \\
&= \underbrace{\bar{\psi}(x)\left(i\gamma^{\mu}\partial_{\mu} - m\right)\psi(x)}_{\text{free Lagrangian}} - \bar{\psi}(x)q\gamma^{\mu}A_{\mu}\psi(x) - \frac{1}{4}F_{\mu\nu}F^{\mu\nu} \\
&= \bar{\psi}(x)i\gamma^{\mu}\partial_{\mu}\psi(x) - m\bar{\psi}(x)\psi(x) - \bar{\psi}(x)q\gamma^{\mu}A_{\mu}\psi(x) - \frac{1}{4}F_{\mu\nu}F^{\mu\nu}
\end{aligned} \tag{1.7}$$

where:

$\bar{\psi}(x)i\gamma^{\mu}\partial_{\mu}\psi(x)$; Propagation of the fermion

$m\bar{\psi}(x)\psi(x)$: Mass of the fermion

$\frac{1}{4}F_{\mu\nu}F^{\mu\nu}$: Propagation of the boson

$q\bar{\psi}(x)\gamma^{\mu}A_{\mu}\psi(x)$: Boson-fermion interaction

1.5 The strong interaction: QCD (Quantum ChromoDynamics)

Quantum Chromodynamics (QCD) [34] is a fundamental theory that encompasses the study of nuclei and their constituents. It specifically deals with the interactions between particles that possess color charge, and it constitutes the $SU(3)_C$ component of the Standard Model. QCD is responsible for describing the strong nuclear force, which governs the behavior of quarks and gluons within atomic nuclei.

In the realm of QCD, there exist different types or flavors of Dirac fermions known as quarks. Each quark flavor is associated with three distinct colors: red, blue, and green. Consequently, a quark, such as an up quark, can be envisioned as a composite of three individual quark field components, all possessing equal mass. This tripartite nature of quarks reflects the underlying principles of QCD and the intricate dynamics that govern the behavior of elementary particles at the subatomic level. The fermions' Lagrangian density in a free-field configuration can be expressed as:

$$\mathcal{L} = \bar{\psi}(x)i\gamma^{\mu}\partial_{\mu}\psi(x) \tag{1.8}$$

where $\psi(x)$ is now an $SU(3)_C$ triplet of the quark fields. The local gauge invariance can be noted as:

$$\psi(x) \to e^{\frac{i}{2}g_s\lambda^a\theta_a(x)}\psi(x) \tag{1.9}$$

where λ^a are the eight ($3^2 1 = 8$) Gell-Mann matrices generated according to the $SU(3)_C$ group and it also produces the 8 vector Gluon fields G_{μ}. Here g_s is related to the strong coupling constant $\alpha_s = \frac{g_s^2}{4\pi}$. Similarly to QED, the normal derivative is substituted with the covariant derivative, which is defined as:

$$D_{\mu} = \partial_{\mu} + \frac{i}{2}g_s\lambda^a G_a^{\mu} \tag{1.10}$$

The expression for the field strength tensor can be formulated as:

$$G_{\mu\nu}^a = \partial_{\mu}G_{\nu}^a - \partial_{\nu}G_{\mu}^a + g_s f^{abc}G_{\mu}^b G_{\nu}^c \tag{1.11}$$

Now, we can represent the QCD Lagrangian under the $SU(3)_C$ gauge group as:

$$
\begin{aligned}
\mathcal{L}_{QCD} &= \bar{\psi}\left(i\gamma_\mu D^\mu - m\right)\psi - \frac{1}{4}G^{\mu\nu}G_{\mu\nu} \\
&= \underbrace{i\bar{\psi}\gamma_\mu\partial^\mu\psi}_{\mathcal{L}_q^{\text{kin}}} - \underbrace{m\bar{\psi}\psi}_{\mathcal{L}_q^{m}} - \underbrace{g_s\bar{\psi}\gamma_\mu t^a G_a^\mu\psi}_{\mathcal{L}_q^{\text{int}}g} - \underbrace{\frac{1}{4}\left(\partial_\mu G_\mu^a\right)\left(\partial^\mu G_a^\nu - \partial^\nu G_a^\mu\right)}_{\mathcal{L}_g^{\text{kin}}} \\
&- \underbrace{-\frac{g_s}{2}f^{abc}\left(\partial_\mu G_{\nu a} - \partial_\nu G_{\mu a}\right)G_b^\mu G_c^\nu}_{\mathcal{L}_{3g}^{\text{int}}} - \underbrace{\frac{g_s^2}{4}f^{abc}f^{ade}G_{b\mu}G_{c\nu}G_d^\mu G_e^\nu}_{\mathcal{L}_{4g}^{\text{int}}}
\end{aligned}
\tag{1.12}
$$

under the transformation of gluon fields as:

$$
G_\mu^a \to G_\mu^a - \frac{1}{g_s}\partial_\mu\alpha^a - f^{abc}\alpha_b G_{c\mu} \tag{1.13}
$$

The components $\mathcal{L}_q^{\text{kin}}$ and $\mathcal{L}_g^{\text{kin}}$ refer to the propagators associated with quarks and gluons, respectively. $\mathcal{L}_q^{\text{int}}g$ represents the interactions between quarks and gluons, as illustrated by a representative Feynman diagram depicted in Figure 1.1. The terms $\mathcal{L}_{3g}^{\text{int}}$ and $\mathcal{L}_{4g}^{\text{int}}$ describe the interactions involving three and four gluons respectively, with corresponding Feynman diagrams displayed in the middle and right of Figure 1.1.

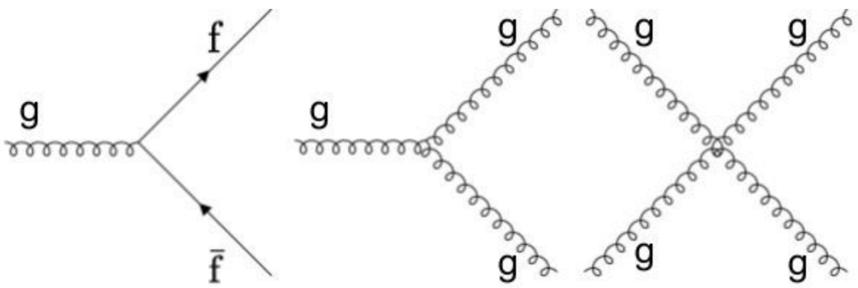

Figure 1.1: Feynman diagrams SU(3) QCD: quark-gluon interaction vertex (left), three-gluon vertex (middle), four-gluon vertex (right) [35].

QCD, exhibits two key properties: asymptotic freedom and quark confinement. Asymptotic freedom describes the weakening of the interaction between quarks at large distances. Quark confinement, on the other hand, explains how quarks are bound within composite particles called hadrons. These properties shape our understanding of strong interactions and the behavior of quarks in QCD.

1.6 Electroweak unification

Within the framework of the Standard Model (SM), the unification of the electromagnetic and weak interactions into a single electroweak (EW) interaction represents a significant achievement. This unified theory, known as the Glashow-Weinberg-Salam (GWS) theory [36], revolutionized our understanding of fundamental forces. By treating the electromagnetic and weak forces as different manifestations of the same underlying interaction, the GWS theory provides a coherent description of the fundamental forces of nature.

The electroweak theory is mathematically formulated using an $SU(2)_L \times U(1)_Y$ gauge group, where $SU(2)_L$ represents the weak isospin symmetry group and $U(1)_Y$ represents the hypercharge symmetry group. This gauge group framework allows for a unified treatment of the electromagnetic and weak interactions. In this theory, particles interact by exchanging mediator bosons.

The photon, the mediator of the electromagnetic interaction, is responsible for the transmission of electromagnetic forces between charged particles. It is the carrier of the electromagnetic force and plays a fundamental role in the interactions between charged particles.

The W^+ and W^- bosons, along with the Z^0 boson, serve as the mediators of the weak interaction. These bosons are responsible for the processes involving the decay and transformation of elementary particles, such as the conversion of one type of quark into another or the decay of a heavy particle.

By unifying the electromagnetic and weak interactions into the electroweak theory, the GWS theory provides a comprehensive framework that successfully describes a wide range of experimental observations and phenomena. The electroweak theory is described by the following Lagrangian:

$$\mathcal{L}_{\text{EW}} = \sum_{\Psi} \bar{\Psi} \left[i\gamma^\mu D_\mu \right] \Psi - \frac{1}{4} W^a_{\mu\nu} W^{\mu\nu}_a - \frac{1}{4} B_{\mu\nu} B^{\mu\nu} \tag{1.14}$$

$$D_\mu = \partial_\mu + igT^a W^a_\mu + ig' \frac{1}{2} T_Y B_\mu \tag{1.15}$$

where T^a and T_Y are the generators of $SU(2)_L$ and $U(1)_Y$ respectively while g and g' are the respective coupling constants. The interactions between particles mediated by gauge bosons are described by the first two terms, while the interactions between the gauge fields themselves are described by the last two terms. Gauge antisymmetric tensors constructed from the gauge fields B_μ and W^a_μ are represented by $F^A_{\mu\nu}$ and $B_{\mu\nu}$.

The gauge bosons can be written as linear combinations of the gauge fields:

$$\gamma : A_\mu = \cos\theta_W B_\mu + \sin\theta_W W^3_\mu \tag{1.16}$$

$$Z^0 : Z_\mu = -\sin\theta_W B_\mu + \cos\theta_W W^3_\mu \tag{1.17}$$

$$W^\pm : W^\pm_\mu = \frac{1}{\sqrt{2}} \left(W^1_\mu \mp i W^2_\mu \right) \tag{1.18}$$

where θ_W is the weak mixing (Weinberg) angle and can be represented as a factor of the coupling constants as follows :

$$\begin{aligned} \cos\theta_W &= \frac{g}{\sqrt{g^2 + g'^2}} \\ \sin\theta_W &= \frac{g'}{\sqrt{g^2 + g^2}} \end{aligned} \tag{1.19}$$

According to the electroweak Lagrangian 1.14, in order to preserve the $SU(2)_L \times U(1)_Y$ gauge symmetry, it is necessary that the fermionic and bosonic fields (W, Z) are massless. However, experimental observations have shown the existence of massive bosons and fermions, which poses a problem.

1.7 Spontaneous symmetry breaking in the Higgs mechanism

Observations from experiments have confirmed the existence of massive fermions and bosons, which is inconsistent with previous theories. In 1964, the British physicist Peter Higgs and the two Belgian theorists Robert Brout and François Englert offered a possible solution to this problem: symmetry $SU(2)_L \times U(1)_Y$ must be broken, while maintaining a conserved $U(1)_{EM}$ symmetry. The mechanism of this break, called Brout-Englert-Higgs mechanism which involves introducing a new scalar boson, the Higgs boson, and creating a "Higgs field" that interacts with W and Z bosons, providing them with masses. This process is known as "spontaneous symmetry breaking".

This mechanism requires the introduction of a new doublet of complex scalar fields:

$$\begin{aligned} \Phi_H &= \begin{pmatrix} \Phi^+ \\ \Phi^0 \end{pmatrix} \\ \Phi^+ &= \frac{\phi_1 + i\phi_2}{\sqrt{2}} \\ \Phi^0 &= \frac{\phi_3 + i\phi_4}{\sqrt{2}} \end{aligned} \tag{1.20}$$

where ϕ_i are real fields. The Lagrangian describing this doublet is given by :

$$\mathcal{L}_{\text{scalar}} = \left(D_\mu \Phi_H\right)^\dagger \left(D^\mu \Phi_H\right) + V\left(\Phi_H\right) \tag{1.21}$$

where $\left(D^\mu \Phi_H\right)^\dagger \left(D_\mu \Phi_H\right)$ contains the interaction between the Higgs and gauge bosons, and the second term is a potential of the following form:

$$V\left(\Phi_H\right) = -\mu^2 \Phi_H^\dagger \Phi_H + \lambda \left(\Phi_H^\dagger \Phi_H\right)^2 \tag{1.22}$$

where μ and λ are two free parameters.

The mass term of the Higgs boson is expressed as follows: $m_H^2 = 2|\mu|^2 = 2\lambda v^2$, while the masses of the gauge bosons are written as follows:

$$m_W^2 = \frac{1}{4} g^2 v^2, \quad m_Z^2 = \frac{1}{4}(g^2 + g'^2) v^2 \tag{1.23}$$

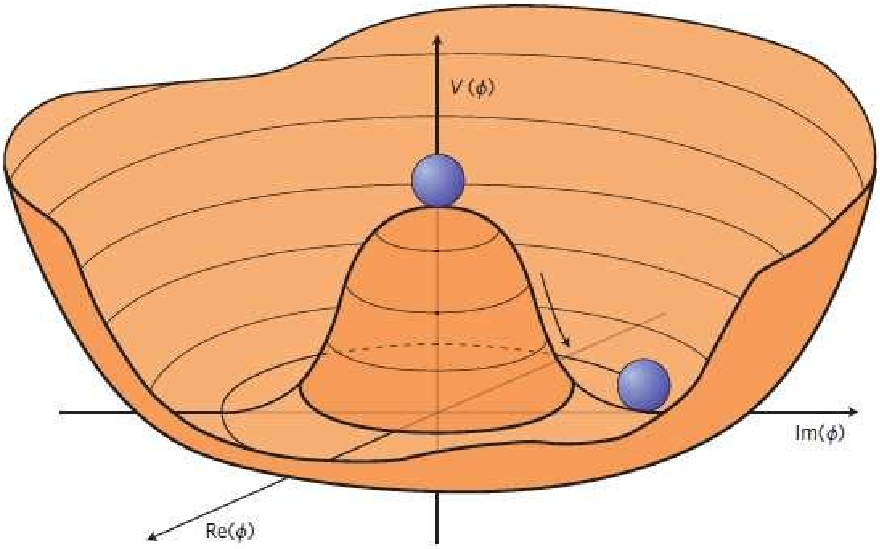

Figure 1.2: The Higgs potential as a function of the complex scalar field [37].

1.8 The limits of the Standard Model

The Standard Model has demonstrated remarkable resilience and a predictive nature that has often been confirmed through experimentation. Notably, the existence of the W and Z bosons was postulated prior to their experimental discovery in 1983 [29, 30]. Experimental measurements of cross sections for various processes, such as the production of top-antitop pairs or gauge bosons, align with the expectations of the Standard Model.

However, the treatment of neutrinos as massless particles in the Standard Model conflicts with observations of neutrino oscillations, which indicate that neutrinos indeed possess non-zero masses. The Standard Model also presents other issues, such as the unexplained existence of multiple families (generations) of fermions. For example, the top quark is approximately 35,000 times heavier than the up quark, despite both being members of the same particle family. This hierarchy poses a challenge for understanding the underlying mechanisms responsible for fermion masses and raises questions about the origin of these mass differences within the framework of the Standard Model.

Additionally, the model lacks an explanation for the presence of dark matter, despite substantial observational evidence supporting its existence. Observations, such as galaxy rotation patterns, gravitational lensing, and cosmic microwave background measurements, strongly suggest the existence of dark matter, which constitutes a significant portion of the universe's mass [38]. This discrepancy between the Standard Model's predictions and observational data has motivated the search for new theoretical frameworks and exotic particles such as Axion-Like-Particles that can provide a satisfactory explanation for the nature of dark matter.

1.9 Heavy Ions Physics

Heavy-ion collisions primarily aim to probe the quark-gluon plasma (QGP), a state predicted by quantum chromodynamics (QCD) in which quarks and gluons move freely. This state resembles the conditions shortly after the Big Bang [39]. While the ALICE experiment at the LHC is the main avenue for studying the QGP, the ATLAS and CMS experiments have also made significant contributions in this field. In this memorandum, our focus is to explore a distinct aspect of these collisions within the framework of the ATLAS experiment. Specifically, we investigate ultra-peripheral collisions involving lead nuclei, where the nuclei do not collide head-on.

When analyzing heavy-ion collisions, researchers have precise control over two key factors: the choice of colliding nuclei and the collision energy. These factors are known with exceptional precision. However, it is crucial to differentiate between understanding the overall colliding systems and solely knowing the individual colliding nuclei.

Two primary experimental setups are typically employed for heavy-ion collisions: fixed target and collider configurations. In a fixed target setup, a beam of accelerated particles is directed towards a stationary target. This approach is renowned for its ability to deliver high luminosities, allowing for a large number of collisions to be observed. Conversely, colliders are better suited for achieving higher collision energies, making them ideal for studying the properties of the QGP.

Heavy-ion collisions are primarily defined by three quantities:

- The impact parameter, which indicates the centrality of the collision. Based on this parameter, we can categorize the collisions into three types, as outlined in Table 1.3
- The number of participant nucleons.
- The number of collisions.

Collision type	Impact Parameter	Properties
Central	Small (b $<$ R)	Almost heads-on collision
Peripheral	Large (b $>$ R)	Partial collision
Ultra peripheral	Very large (b $>$ 2R)	Occurs solely through the photons generated by the strong electromagnetic field produced by the ions

Table 1.3: Collisions types and their properties

For our study, we primarily utilize heavy ions due to their high number of participant nucleons, particularly protons, which significantly enhance the cross section compared to proton-proton (pp) collisions, as explained in the subsection 1.10.3.

Manipulating the impact parameter to achieve ultra-peripheral collisions aims to suppress the hadronic interactions.

1.9.1 UPCs (Ultra-Peripheral nuclear Collisions)

Ultra-peripheral collisions (UPC) [40] (Figure 1.3) occur when the colliding ions pass each other with an impact parameter that is large enough (at least twice the radii of both nuclei) to avoid hadronic interactions, yet small enough to allow for electromagnetic interactions. These collisions provide an opportunity to investigate photo-nuclear and two-photon interactions at energies surpassing those achievable in fixed target experiments. The motivation for studying such interactions in heavy ions stems from the fact that the photon flux scales with the square of the atomic number (Z^2). In the case of heavy ions, the couplings are sufficiently strong to allow for multi-photon interactions, which is why they are used at ATLAS to study light-by-light scattering [41].

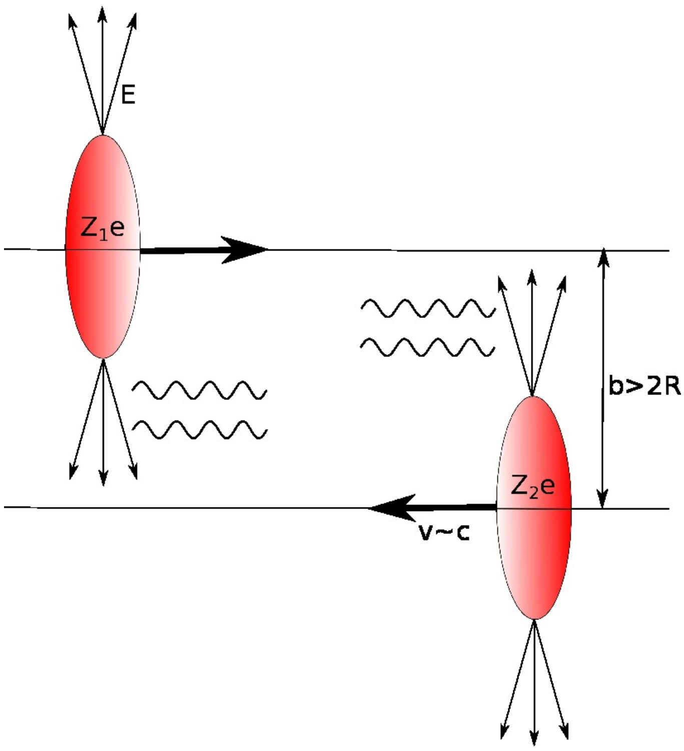

Figure 1.3: The impact parameter, denoted as b, exceeds twice the radius (R) of the colliding hadrons. The photon flux originating from each nucleus is directly proportional to the square of the atomic number (Z) [42].

1.10 Light-by-Light scattering

1.10.1 Theoretical background

Initially, the concept of photon-photon interaction seemed unexpected. According to Maxwell's equations, there is no direct prediction of photon-to-photon interaction. When two beams of light intersect, they do not interact in the conventional sense. While they may exhibit local interference due to the superposition of their electromagnetic fields, they continue along their paths without undergoing any modification. From the perspective of classical electrodynamics, the principle of superposition holds, which implies that direct interaction between electromagnetic fields is prohibited within this framework. The superposition principle is described with the following equation:

$$\begin{aligned} \mathcal{L}_0 &= -\frac{1}{4\mu_0} F^{\mu\nu} F_{\mu\nu} = \frac{1}{2}\varepsilon_0 \left(\mathbf{E}^2 - c^2\mathbf{B}^2\right) = \frac{1}{2}\left(\varepsilon_0 \mathbf{E}^2 - \frac{1}{\mu_0}\mathbf{B}^2\right), \\ F^{\mu\nu} &= \begin{pmatrix} 0 & -\frac{1}{c}E_1 & -\frac{1}{c}E_2 & -\frac{1}{c}E_3 \\ \frac{1}{c}E_1 & 0 & -B_3 & B_2 \\ \frac{1}{c}E_2 & B_3 & 0 & -B_1 \\ \frac{1}{c}E_3 & -B_2 & B_1 & 0 \end{pmatrix}, \end{aligned} \tag{1.24}$$

where $F^{\mu\nu}$ is the electromagnetic field strength tensor and the velocity of light (squared) is given by $c^2 = 1/(\varepsilon_0\mu_0)$ with μ_0, ε_0 being the the magnetic permittivity and dielectric permeability of the vacuum, respectively.

In the 1940s, with the advancement of quantum physics, scientists formulated the theory of electromagnetism in its quantized form known as quantum electrodynamics (QED). However, as early as 1934, Heisenberg and Euler had proposed a theory that foreshadowed the future development of QED. They suggested that through non-linear effects, two photons could interact.

In the framework of QED, the process is described as follows: Two electrons interact by exchanging one or more photons. This quantum representation captures the essence of electromagnetic interaction. Similarly, two photons can interact by exchanging an electron (or any other particle carrying an electric charge), as depicted in Figure 1.4. The crucial aspect is that electrons possess an electric charge, which remains a fundamental requirement in these interactions.

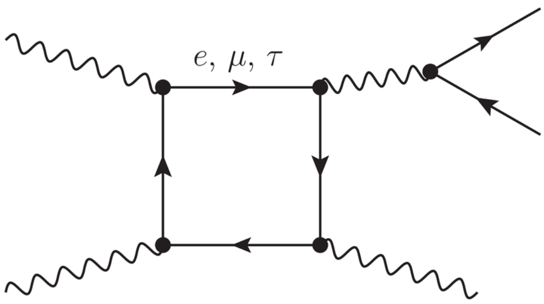

Figure 1.4: Generic QED diagram for the light-by-light scattering process [43].

As a result, the initial photon must return the electron it received from the second photon, resulting in an exchange of electrons. Within the framework of QED, this process is referred to as a box-shaped (or looped) exchange, involving both electrons and their antiparticles (positrons). In this purely quantum phenomenon, the exchanged particles manifest only fleetingly for the duration of the interaction, leading to what is known as virtual particles.

In 1935, Euler and Kockel [44] calculated the primary perturbative correction to the Lagrange density $\mathcal{L}_0$ of the Maxwell field. Their analysis focused on small field strengths and photon frequencies significantly below the threshold for electron-positron pair production. The result they obtained was as follows:

$$\begin{aligned} \mathcal{L} &= \mathcal{L}_0 + \frac{2\alpha^2}{45}\frac{\lambda_e^4}{\hbar c}\left[-10\mathcal{L}_0^2 + \frac{7}{4}T^{\mu\nu}T_{\mu\nu}\right] \\ &= \mathcal{L}_0 + \frac{2\alpha^2}{45}\frac{\lambda_e^4}{\hbar c}\left[-10\mathcal{L}_0^2 + 7\left((T_{00})^2 - \frac{1}{c^2}\mathbf{S}^2\right)\right] \end{aligned} \tag{1.25}$$

$$T^{\mu\nu} = \frac{1}{\mu_0}\left[F^{\mu\alpha}F^{\nu}_{\alpha} - \frac{1}{4}g^{\mu\nu}F^{\alpha\beta}F_{\alpha\beta}\right] \tag{1.26}$$

where $T^{\mu\nu}$ (equation 1.26) is the stress-energy-momentum tensor of the free electromagnetic field, α is the fine structure constant, $\lambda_e = \frac{\hbar}{m_e c}$ is the (reduced) Compton wavelength of the electron with mass m_e, and S is the Poynting vector given by:

$$\mathbf{S} = \frac{1}{\mu_0}\mathbf{E} \times \mathbf{B} \tag{1.27}$$

As a consequence, the resulting Lagrangian exhibits non-linearity, giving rise to non-linear corrections in the classical Maxwell equations. Examining equation 1.25, we can observe that the Poynting vector provides an interaction term between electromagnetic fields (photons). Additionally, Euler and Kockel made the pioneering calculation of the cross section for photon-photon scattering, yielding the following result for photons of frequency $\hbar\omega << m_e c^2$:

$$\sigma \sim \alpha^4 \lambda_e^8 \left(\frac{\omega}{c}\right)^6 \tag{1.28}$$

As a result, it was found that this cross section is extremely small, measuring approximately 10^{-30} cm^2 for γ-rays and 10^{-70} cm^2 for visible light. Euler noted that this minuscule value poses a significant challenge in terms of experimental observation of this phenomenon.

1.10.2 Experimental approach

The experimental quest to detect light-by-light scattering began as early as 1928 [45], prior to the calculations by Euler and Kockel. Various attempts were made using sunlight and other methods, but no conclusive evidence of photon-photon collisions was found. However, an upper limit for the cross section (σ) of photon-photon scattering was established, with $\sigma < 3 \times 10^{20}$ cm^2 [46]. Subsequent experimental efforts, including those using high-power lasers [47] and Compton back-scattering, also yielded no clear detection of the process [48]. Indirect measurements, such as studying the anomalous magnetic moment of particles, provided some evidence of its existence the LbyL it is predicted to contribute substantially [49, 50]. The $\gamma\gamma \rightarrow \gamma\gamma$ reaction has been measured in photon scattering in the Coulomb field of a nucleus (Delbrück scattering) [3–6] and in the photon splitting process [7]. However, direct observation of the process, as originally predicted by Euler and Heisenberg, remains extremely challenging due to the very small cross section involved.

1.10.3 Light-by-light scattering evidence at the LHC

In fundamental physics, there are often long gaps between predictions and experimental confirmations. Examples include the Higgs boson and gravitational waves, which were predicted decades before their discoveries. The magnetic birefringence of the vacuum, proposed by Heisenberg and Euler, took nearly 80 years to be demonstrated. It also predicted elastic photon-photon scattering, but verifying this process is challenging due to the low probability of photon interactions. Even the most powerful lasers lack the intensity required for reliable photon-photon interactions.

In 2013 [21], a new approach was proposed to search for light-by-light (LbyL) scattering at the LHC, utilizing the large quasi-real photon fluxes generated in electromagnetic interactions of protons (p) and lead (Pb) heavy ions 1.5. This approach takes advantage of the fact that charges accelerated at high energies generate electromagnetic fields. In particular, lead ions are accelerated to speeds close to that of light, leading to the relativistic contraction of their electromagnetic fields. This contraction allows them to be treated as a beam of photons in the equivalent photon approximation (EPA), with an energy scale of $Q^2 < 1/R^2$, where

R represents the radius of the charge distribution. By convolving the photon flux with the elementary cross section for the process, it becomes possible to calculate the cross section for the reaction $Pb + Pb(\gamma\gamma) \rightarrow Pb + Pb\gamma\gamma$. The cross section in a collider involving hadrons (A and B) and employing the equivalent photon approximation (also known as the Weizsäcker-Williams method) can be expressed as follows:

$$\sigma^{\text{excl}}_{\gamma\gamma\rightarrow\gamma\gamma} = \sigma(\text{AB} \xrightarrow{\gamma\gamma} \text{A}\gamma\gamma\text{B}) = \int \mathrm{d}\omega_1 \, \mathrm{d}\omega_2 \frac{\text{f}_{\gamma/\text{A}}(\omega_1)}{\omega_1} \frac{\text{f}_{\gamma/\text{B}}(\omega_2)}{\omega_2} \sigma_{\gamma\gamma\rightarrow\gamma\gamma}\left(\sqrt{\text{S}_{\gamma\gamma}}\right) \tag{1.29}$$

The high electrical charge of lead ions, with 82 protons in their nuclei, results in an intensified electromagnetic field, leading to a significantly enhanced cross section compared to proton-proton collisions.

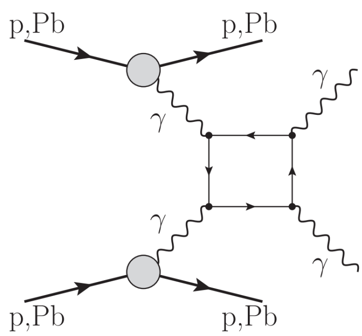

Figure 1.5: Schematic diagram of elastic $\gamma\gamma \rightarrow \gamma\gamma$ collisions in electromagnetic proton and/or ion interactions at the LHC. The initial-state photons are emitted coherently by the protons and/or nuclei which survive the electromagnetic interaction [21].

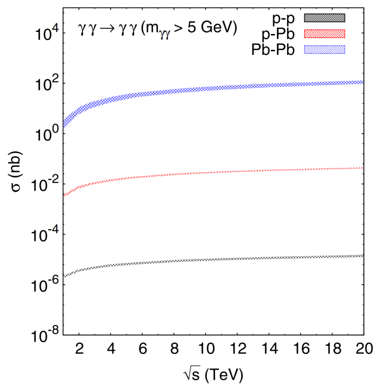

Figure 1.6: Cross sections for exclusive $\gamma\gamma \rightarrow \gamma\gamma$, with pair masses above 5 GeV, in ultraperipheral Pb-Pb (top curve), p-Pb (middle) and p-p (bottom) collisions as a function of the nucleon-nucleon c.m. energy in the range $\sqrt{s_{NN}}$ = 1-20 TeV [21].

Previous results

After an initial report in 2017 providing evidence of light-by-light scattering based on data from ultra-peripheral collisions of heavy ions at the ATLAS experiment [11], further confirmation was obtained in 2018 [20]. The observation of light-by-light scattering was made with nearly three times more data recorded in the ATLAS detector, corresponding to an integrated luminosity of 1.73 nb^{-1} compared to 0.48 nb^{-1} in 2015. A total of 59 events were observed in the data, while an expected number of 30 $\pm$ 4 (syst.) signal events and 12 $\pm$ 1 (stat.) $\pm$ 3 (syst.) background events were predicted. The invariant mass distribution of the diphoton system is illustrated in Figure 1.7.

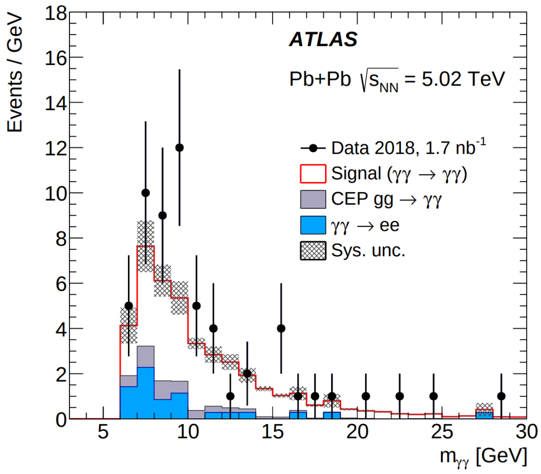

Figure 1.7: Diphoton invariant mass of the events observed after applying all selection criteria in ATLAS. Data (points) are compared to the sum of signal and background expectations (stacked histograms). The statistical uncertainties on the data are shown as vertical bars. Systematic uncertainties of the signal and background processes, excluding that of the luminosity, are shown as shaded bands [20].

In a more focused range of $0 < \text{Aco} < 0.005$, the compatibility of the data with the background-only hypothesis was assessed. Within this range, 42 events were observed, while an expected number of 25 ± 3 (syst.) signal events and 6 ± 1 (stat.) ± 2 (syst.) background events were predicted. The excess in the data was quantified by calculating the background-only p-value using a profile likelihood-ratio test statistic, leading to an observed (expected) statistical significance of 8.2 (6.2) standard deviations.

1.10.4 LbyL scattering beyond SM

In QED, the $\gamma\gamma \to \gamma\gamma$ reaction occurs via virtual one-loop box diagrams involving fermions, which is a process of $O(\alpha_{em}^4)$, which makes it very rare. However, extensions of the Standard Model introduce additional virtual contributions, making the measurement of light-by-light scattering a sensitive probe for new physics. Collider and laser experiments offer valuable opportunities to study these phenomena and search for physics beyond the Standard Model. The LbyL scattering can be very useful to perform many beyond SM searches.

Axion Like Particles

Axions were initially proposed to address the strong CP problem in QCD [51] and are pseudo Nambu-Goldstone bosons associated with the breaking of a new global Peccei-Quinn (PQ) U(1) symmetry. They serve as potential candidates for cold dark matter with small masses. Axion-like particles (ALPs) also arise in theories with spontaneously broken global, approximate, symmetries and can have independent couplings and masses up to the TeV scale. Detecting axions or ALPs is challenging due to their weak interactions with matter and radiation.

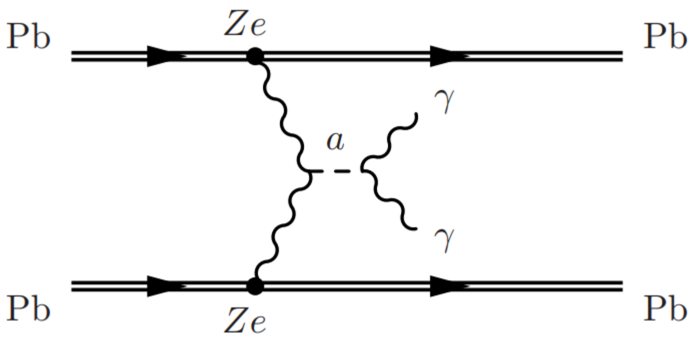

Figure 1.8: Exclusive ALP production in ultra-peripheral Pb-Pb collisions [52].

Light-by-light scattering $\gamma\gamma \rightarrow \gamma\gamma$ is a promising channel for searching for ALPs due to their coupling to photons. In photon-photon collisions, particles that directly interact with photons can be produced via an s-channel process, resulting in a distinctive peak in the invariant mass spectrum. One well-known example of such particles, which can produce narrow diphoton resonances, is axion-like particles (ALPs) [52].

1.10.5 Previous results

In a more recent analysis that combined data from 2015 and 2018, resulting in an increased integrated luminosity of 2.22 nb^{-1}, the light-by-light (LbyL) scattering channel was utilized to search for axion-like particles (ALPs). The measured invariant mass spectrum, depicted in Figure 1.9, was employed to derive constraints on the cross section of the $\gamma\gamma \rightarrow a \rightarrow \gamma\gamma$ reaction, where "a" represents the ALP. The LbyL signal, $\gamma\gamma \rightarrow e^+e^-$, and central exclusive production (CEP) $gg \rightarrow \gamma\gamma$ processes were treated as backgrounds. Monte Carlo (MC) events for the ALP signal were generated using STARlight v2.0.

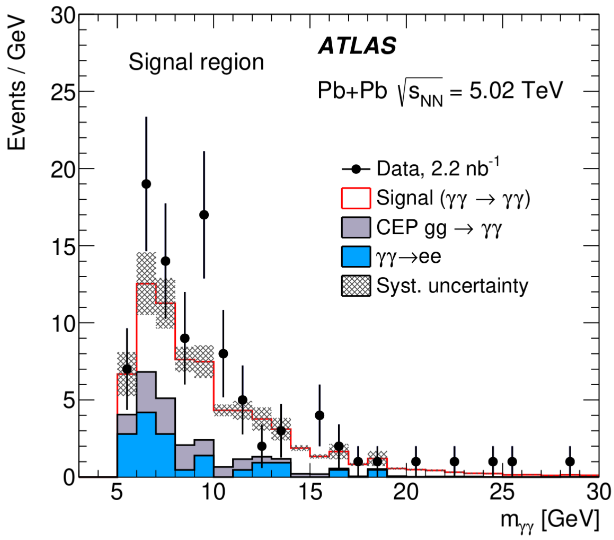

Figure 1.9: Diphoton invariant mass distribution for $\gamma\gamma \to \gamma\gamma$ event candidates. Data (points) are compared with the sum of signal and background expectations (stacked histograms). The signal prediction is normalised to the same integrated luminosity as the data. Systematic uncertainties in the signal and background processes, excluding that in the luminosity, are shown as shaded bands [53].

A maximum likelihood fit was applied to estimate the signal strength μ at a 95% confidence level (CL). The resulting limits on the signal strength μ were then converted to limits on the MC cross section $\sigma_{\gamma\gamma\to a\to\gamma\gamma} = \mu_C Ls \cdot \sigma_{gen}$. The observed and expected 95% CL limits on the ALP production cross section are presented in Figure 1.10. Notably, a local excess of 2.1 standard deviations near a mass of 10 GeV represents the largest deviation from the background-only hypothesis.

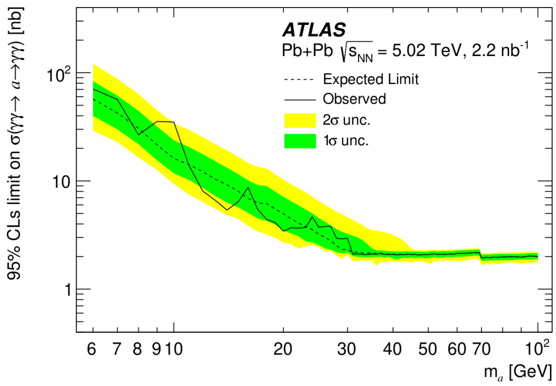

Figure 1.10: The 95% CL upper limit on the ALP cross section $\sigma_{\gamma\gamma\to a\to\gamma\gamma}$ for the $\gamma\gamma \to a \to \gamma\gamma$ process as a function of ALP mass m_a. The observed upper limit is shown as a solid black line and the expected upper limit is shown by the dashed black line with its ± 1 and ± 2 standard deviation bands. The discontinuity at $m_a = 70\ GeV$ is caused by the increase of the mass-bin width which brings an increase in signal acceptance [53].

1.11 Conclusion

The Standard Model of Particle Physics serves as the theoretical framework for our study, providing a precise description of elementary particles fermions (quarks and leptons) and bosons, as well as the fundamental forces that govern the universe and dictate interactions between these particles. However, the model has certain limitations, including the absence of gravity, the observed nonzero masses of neutrinos despite their masslessness in the Standard Model, as well as the inability to explain the presence of dark matter.

These limitations motivate us to explore processes that can potentially shed light on extensions to the standard model. In our research, we focus on ultra-peripheral collisions of heavy ions to gain insights into the phenomenon of two-photon scattering. This light-by-light scattering, which was not possible to study within classical electrodynamics, presents an intriguing opportunity to investigate Quantum Electrodynamics within the framework of the Standard Model. However, it is a rare process that poses challenges for experimental probing. Therefore, we also consider additional contributions from beyond the standard model physics, making it a compelling avenue to explore new physics and potential Beyond the Standard Model (BSM) phenomena.

Chapter 2

The ATLAS Detector

2.1 Introduction

All particle physics experiments aim to understand the fundamental building blocks of our universe, known as elementary particles, and their interactions. To achieve this, high-performance equipment is required to generate and detect high-energy physics processes. In order to explore the smallest scales of matter, we need to investigate the highest frequencies, which correspond to the shortest wavelengths. This necessitates the use of particle accelerators-colliders, such as the Large Hadron Collider, and detectors like the ATLAS detector, which enable us to reach the highest possible energies.

2.1.1 Motivation

The Standard Model of Particle Physics is the most precise model in science, and thus far, it has passed all tests with remarkable precision, providing strong experimental evidence for its validity [54]. Yet, it remains incomplete, this is why the Large Hadron Collider (LHC) was built after the discovery of the Higgs boson, to search for the missing pieces of the puzzle. The LHC program is not only limited to the search for the Higgs boson but also aims to better understand the phenomenon of CP violation and matter-antimatter dominance in the Universe. The LHC [55] is a proton-proton and heavy-ion accelerator designed to provide unprecedented center-of-mass energies and luminosities for the discovery of new physics. The LHC also allows measurements of the Standard Model parameters in inaccessible regions of phase space. It is the most powerful particle accelerator ever built and is the successor of the Large Electron Positron (LEP) accelerator.

2.2 The Acceleration chain

Particle accelerators are machines that accelerate charged particles, such as protons and electrons, to very high speeds close to the speed of light. The accelerating process is achieved through the use of electric and magnetic fields that apply forces on the charged particles, causing them to gain energy and increase their speed.

The interest in accelerating particles stems from the fact that accelerated particles can be utilized to explore the fundamental structure of matter and study the properties of subatomic particles such as protons, neutrons, and electrons. By colliding these particles at high speeds, scientists can generate new particles that are not commonly observed in nature, enabling them to investigate their characteristics and interactions. This in turn contributes to a deeper comprehension of the fundamental laws of physics that govern the behavior of matter and energy.

To produce high energies, particle accelerators use a series of stages that gradually increase the speed of the particles. The first stage typically uses a linear accelerator (LINAC) to bring the particles to a moderate energy level. The particles are then injected into a circular accelerator, such as a synchrotron or cyclotron, where they are subjected to alternating magnetic fields that keep them moving in a circular path while increasing their speed.

As the particles gain energy, they become more massive, which causes their path to bend less in the magnetic field. This requires the magnetic field to be increased to keep the particles on track. The final stage is usually a high-energy collider, where particles are smashed into each other head-on to produce the highest-energy collisions.

To investigate the fundamental structure of matter, it is necessary to overcome the forces that bind subatomic particles together, such as the electromagnetic force and the strong nuclear force. Accelerating particles to high energies is crucial in this regard. Subatomic particles have very short wavelengths, corresponding to high frequencies, which are associated with their inherent quantum nature. By accelerating these particles to high energies, researchers can increase their momentum and access a regime where the quantum nature of matter becomes apparent. This enables them to probe the microscopic structure of matter at increasingly finer scales.

In addition to studying the properties of subatomic particles, high-energy collisions have the potential to generate new particles that are not commonly observed in nature. One such example is the discovery of the Higgs boson, accomplished using the Large Hadron Collider (LHC). These breakthroughs in particle physics can have wide-ranging implications, including the development of new technologies and applications, as well as providing a deeper understanding of the universe and the fundamental laws of physics governing it.

2.2.1 The LHC (Large Hadron Collider)

The acceleration chain, composed of both linear and circular accelerators, culminates with the Large Hadron Collider (LHC), which can achieve a center-of-mass energy of up to 14 TeV for protons and 5.5 TeV per nucleon pair for heavy ions. Protons are initially extracted from ionized hydrogen and brought up to 50 MeV by a linear accelerator, LINAC2 [56]. Then they are injected into the BOOSTER, the first circular accelerator that increases their energy up to 1.4 GeV. The Proton Synchrotron (PS) and Super Proton Synchrotron (SPS) then allow the energy to increase to 26 GeV and 450 GeV, respectively. Protons are finally injected into the LHC, which is the largest accelerator complex (26.7 km in circumference). The LHC can reach an energy of 6.5 TeV per beam (13 TeV total for proton-proton collisions) for protons in its nominal configuration. This is achieved through the use of radio frequency cavities and powerful magnets. The acceleration process takes several minutes to reach the desired energy, typically around 20 minutes, but this can vary depending on the specific configuration. Additionally, the protons circulate in both clockwise and counterclockwise directions within the same vacuum tube, thanks to the use of separate beam pipes within the LHC. The ALICE [57], ATLAS (section 2.3), CMS [58], and LHCb [59] experiments are installed at four points where the beams meet. The high energy is necessary to study subatomic particles, which have a small wavelength and high frequency, requiring high energies to observe their behavior.

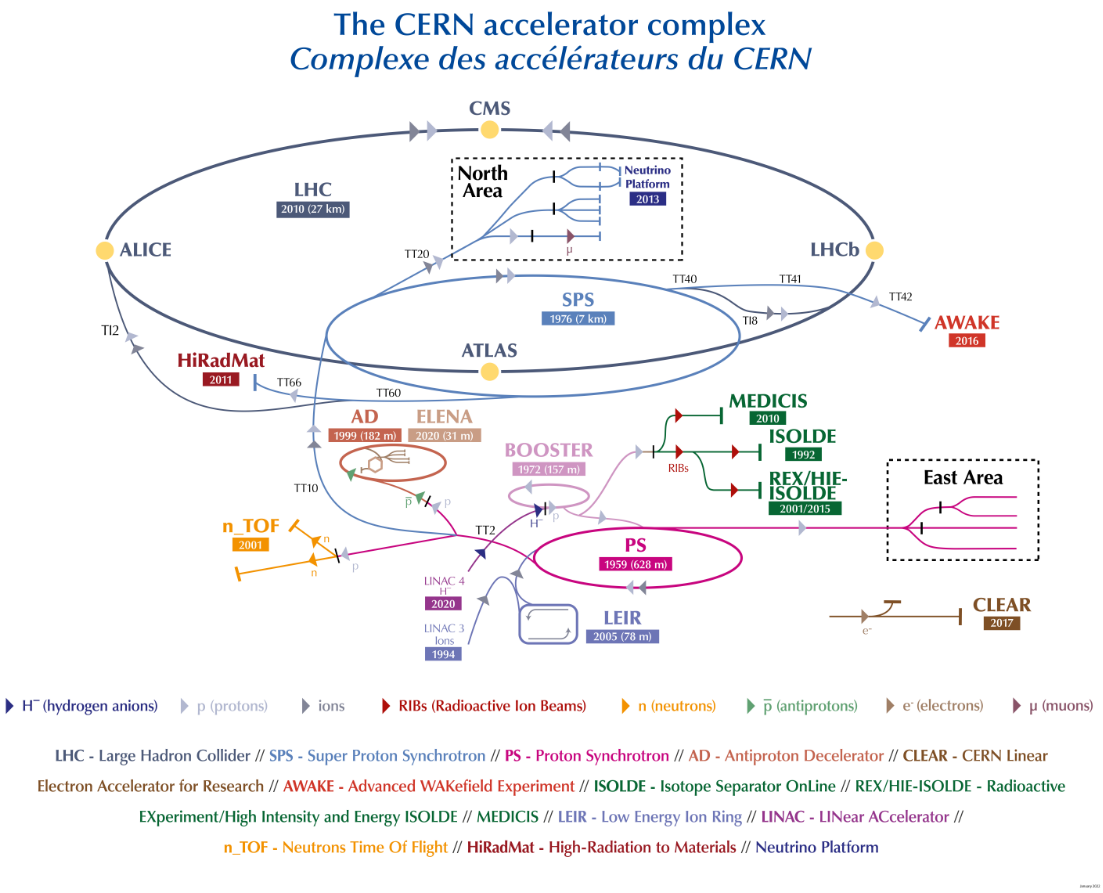

Figure 2.1: Schematic overview of CERN accelerator complex [60].

LHC experiments

Four experiments are recipients of particle collisions delivered by the LHC: ATLAS [61] (A Large Toroidal Lhc ApparatuS) and CMS [58] (Compact Muon Solenoid) which are considered general purpose experiments, and LHCb [59] and ALICE [57] (A Large Ion Colliding Experiment) which are specialized in B physics and heavy ions, respectively.

2.3 The ATLAS Experiment

One of the two versatile detectors installed with the LHC is the ATLAS detector (A Toroidal LHC Apparatus), which has an almost 4π sr acceptance. Like other detectors of its kind, the ATLAS detector is composed of several sub-detectors, including internal detectors dedicated to tracing charged particles, a calorimetric system to measure the energy of most particles, and a system of muon spectrometers that records their trajectories. Additionally, it has a set of solenoid and toroidal magnets used to bend the traces of charged particles and measure their impulse. Despite the variety of sub-detectors, all use the same coordinate system (as shown in Figure 2.2) to determine the position or momentum of an object.

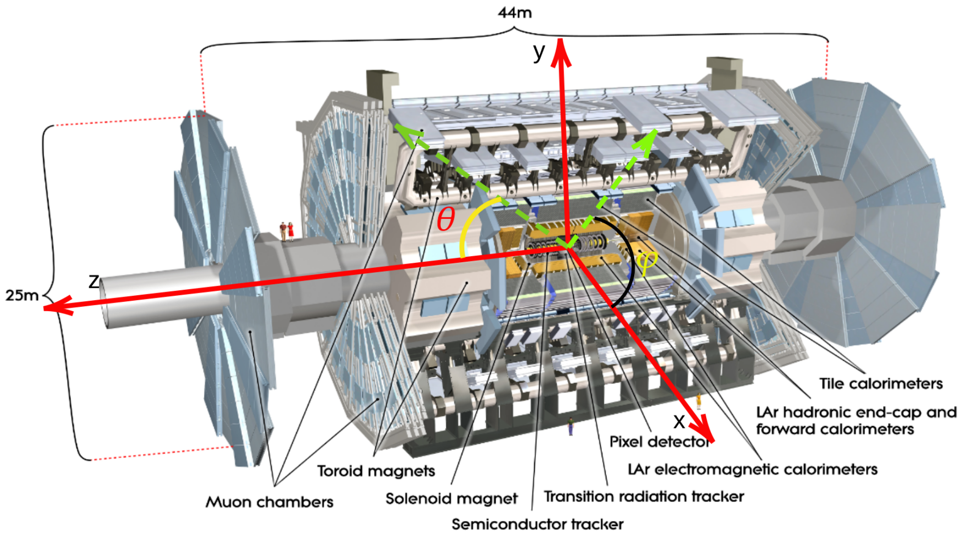

Figure 2.2: Overview of the ATLAS detector [62].

2.3.1 The Coordinate System

ATLAS uses a right-handed coordinate system (as shown in Figure 2.2), where the z-axis aligns with the beam axis, and the x and y axes define the detector's transverse plane. The x-axis conventionally points towards the center of the LHC. The y-axis is slightly tilted with respect to vertical due to the general tilt of the tunnel. The angles θ and φ are used to describe the angle relative to the z and x axes, respectively. However, in later discussions, the variable θ is replaced by η, which is the pseudo-rapidity defined as:

$$\eta = -\ln\left(\tan\frac{\theta}{2}\right) \tag{2.1}$$

This newly introduced quantity helps to overcome one of the inherent uncertainties in hadronic colliders, namely, the longitudinal component of acceleration. In fact, when interacting partons carry only an unknown fraction of the energy of the colliding protons, this can result in an asymmetry of the collision and products that are not at rest in the detector's reference frame, leading to a boost. By contrast, the difference in pseudo-rapidity $\Delta\eta$ is Lorentz invariant under boosts along the longitudinal axis. Furthermore, the difference between two particles in the (η, φ) plane, denoted as ΔR, the angular distance, is defined as:

$$\Delta R = \sqrt{\Delta\varphi^2 + \Delta\eta^2} \tag{2.2}$$

2.3.2 Internal detectors

The measurement of charged particle trajectories and charges is the main function of internal detectors, and they are crucial in identifying particles and reconstructing primary and secondary vertexes. The general structure of internal detectors is shown in Figure 2.3, and they consist of three sub-detectors: the pixel detector, the Semi-Conductor Tracker (SCT), and the Transition Radiation Tracker (TRT), all of which are exposed to the magnetic field generated by the solenoid magnet.

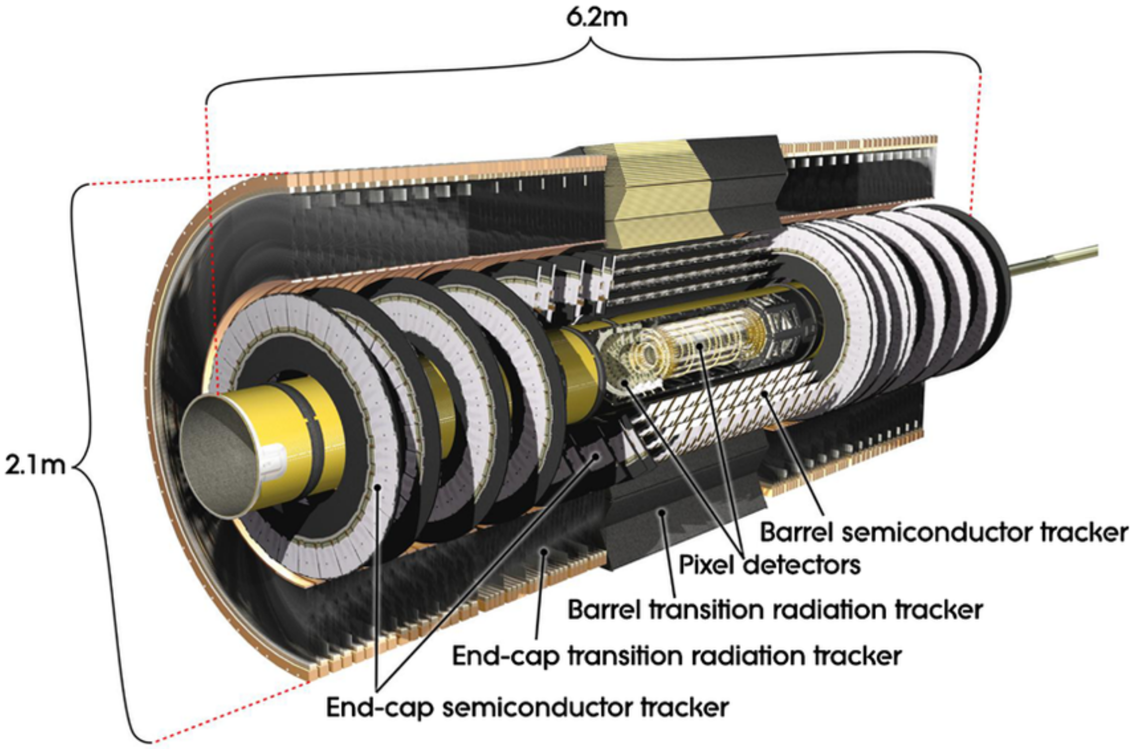

Figure 2.3: Cut-away image of the ATLAS Inner Detector [63].

The Pixel Detector

The pixel detector [64], which is the closest to the beam, plays a crucial role in the measurement of the trajectory and charge of charged particles, as well as in the identification of particles, and is instrumental in the reconstruction of primary and secondary vertices. Its structure is shown in Figure 2.4, and it is composed of two parts, the barrel part and the end-cap part, which provide coverage in the region $|\eta| < 2.5$. The barrel part has three cylindrical pixel layers located between 5 and 12 cm from the collision point, with a total of 13, 22, and 31 million pixels of 50×400 µm^2 each. The end-cap part consists of three discs with a total of 6.6 million pixels. This design ensures that each charged particle emitted within the detector's acceptance generates three pulses, one for each crossed layer. When a particle passes through a pixel, an electron-hole pair is created, and the presence of an electric field applied to the pixel produces a measurable signal that determines the particle's position. The experimental resolution is 115 µm in the longitudinal direction and 10 µm in the direction R - φ. Additionally, this detector is crucial in the reconstruction of secondary vertices necessary for identifying jets from beauty hadrons, but is susceptible to damage from the radiation produced during collisions. The radiation is mainly composed of photons and neutrons, and their fluxes depend on the detector's location. For instance, the innermost layer of the detector closest to the beam undergoes a particle flow of about $40 \times$ 106 Hz/cm^2, compared to 105 Hz/cm^2 for the outermost layer.

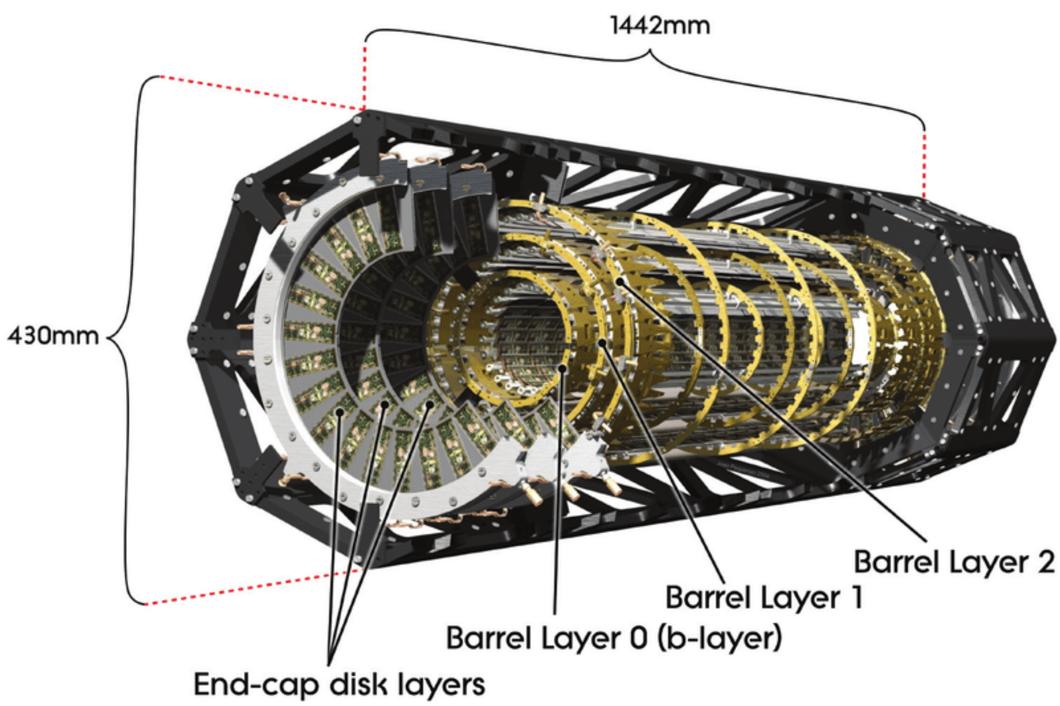

Figure 2.4: Schematic drawing of the ATLAS Pixel Detector. The detector comprises three barrel layers and two endcaps with three discs each. The individual detector modules are mounted on carbon fibre support structures with incorporated cooling circuits [65].

.

The Semi-Conductor Tracker

The technology employed in the Semi-Conductor Tracker (silicon microstrip detector) is quite similar to that used in the pixel detector, with Silicon being the material of choice and comparable geometry. In this case, the barrel part consists of four coaxial cylinders while the end-cap part is formed by nine discs perpendicular to the beam. However, instead of pixels, the sensitive parts are microscopic silicon tracks, measuring 80 µm in width and 126 mm in length. The resolution achieved is 17 µm in the r-φ direction and 580 µm in the longitudinal direction. On average, each charged particle within the geometric acceptance of the detector ($|\eta| < 2.5$) produces four pulses.

The Transition Radiation Tracker

The sub-detector under consideration consists of polyimide tubes with a 4 mm diameter that are filled with a gas mixture (70% Xe - 27% CO2 + 3% O2) with a slight overpressure. The tubes have a gold and tungsten plated anode at their axis of revolution and are surrounded by a material that emits transition radiation. This material allows for the differentiation between low-energy electrons and charged pions $\pi^{\pm}$. Electrons generate more ionization of the gas in the tube and produce a greater signal amplitude than charged pions due to the photons emitted by their passage. The barrel part of the TRT, which is 160 cm long, covers the region $|\eta| < 0.7$, while the endcap part has nine discs orthogonal to the beam in which the tubes are themselves perpendicular. The TRT offers an intrinsic resolution of 160 μm in the R-φ direction.

2.3.3 The calorimeters

A calorimetric system is employed to measure the energy of particles in the region $|\eta| < 4.9$, which is divided into three components (as shown in the left part of Figure 2.5). The first component is the electromagnetic liquid argon calorimeter, which is especially responsive to photons and electrons. The second is the hadronic calorimeter, which detects jets. The third is the forward calorimeter, which uses liquid argon to simultaneously detect both hadrons and electrons/photons.

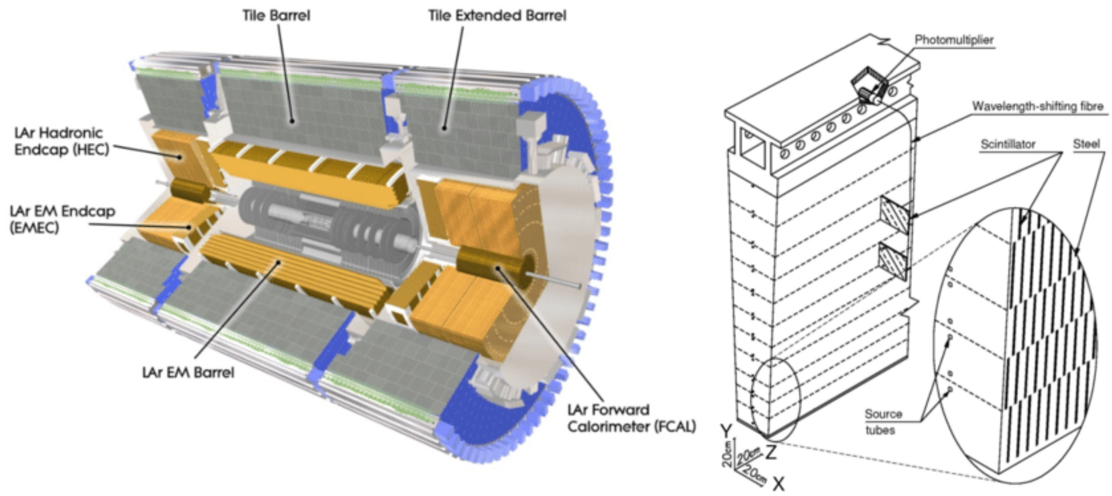

Figure 2.5: (left) ATLAS calorimeter system. (right) Tile calorimeter module internal structure [66].

Electromagnetic liquid argon Calorimeter

The ATLAS electromagnetic calorimeter consists of two parts: a barrel section ($|\eta| < 1.475$) and an endcap section that extends up to $|\eta| < 3.2$, as shown in Figure 2.6. The calorimeter uses a lead/liquid argon arrangement in an accordion structure, which provides complete coverage in φ. The region of the detector where precision measurements are made ($|\eta| < 2.5$) has three detection layers, while beyond that, only two are used [61, 67]. Cryostats are used to maintain the liquid argon at a constant temperature of 90K to prevent bubble formation. The spatial segmentation in the (η, φ) plane depends on the calorimetric layer and the value of $|\eta|$ (Figure 2.7).

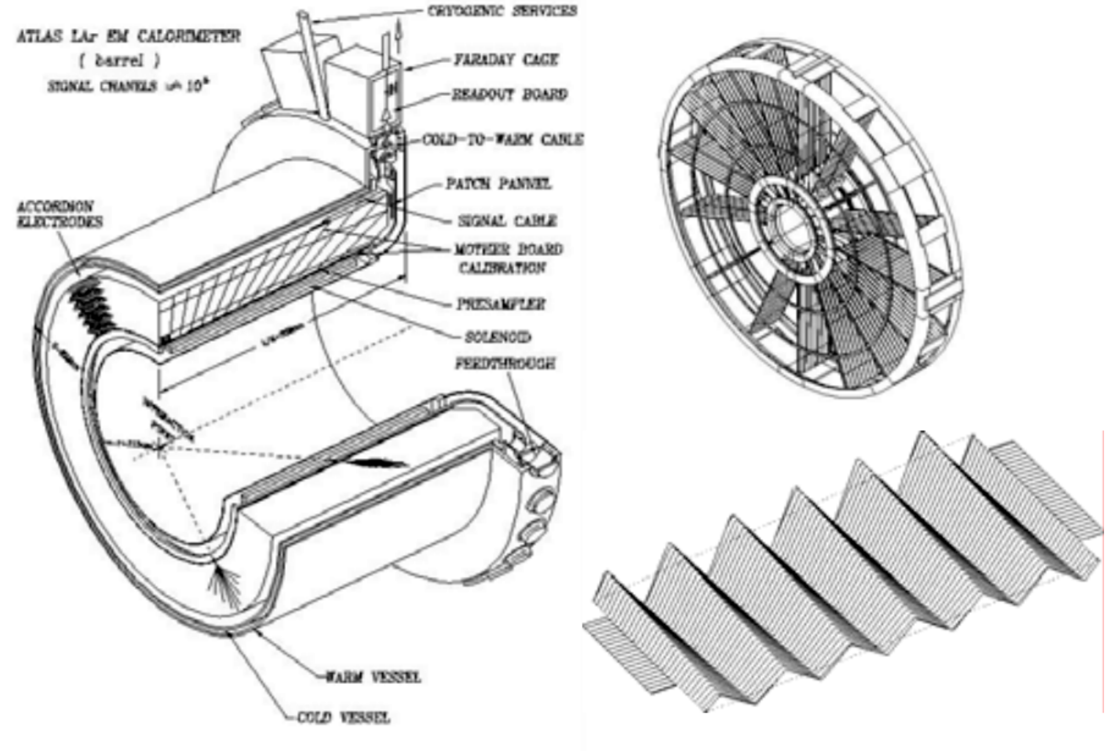

Figure 2.6: View of the Electromagnetic Barrel and Endcap Calorimeters. The left schematic shows a view of a half-barrel assembly of the EMB. The right-hand side shows a skeletal view of an EMEC wheel, and a view of a folded absorber plate for the inner wheel, showing the variable amplitude folds [66].

The first layer has a fine segmentation of $(\Delta\eta \times \Delta\varphi) = (0.0031 \times 0.1)$ to measure the beginnings of the electromagnetic shower development. The second and third layers have coarser segmentations of $(\Delta\eta \times \Delta\varphi) = (0.025 \times 0.025)$ and $(\Delta\eta \times \Delta\varphi) = (0.05 \times 0.025)$, respectively, in the central region. The upstream energy losses of the electromagnetic calorimeter can be corrected using a pre-sampler, which is a portion of the calorimeter made of liquid argon located before the first layer. Its spatial segmentation is $(\Delta\eta \times \Delta\varphi) = (0.025 \times 0.1)$. The design of the electromagnetic calorimeter was optimized for the search for the Higgs boson of the Standard Model in the channels $H \rightarrow \gamma\gamma$ and $H \rightarrow e^+e^-e^+e^-$. The energy resolution in both the barrel and endcap sections is provided in Ref [61] by:

$$\frac{\sigma_E}{E} = \frac{10\%}{\sqrt{E}} \oplus 0.7\%$$

To account for energy loss occurring in front of the electromagnetic (EM) calorimeter, a pre-sampler (Figure 2.7) is employed. The pre-sampler in the barrel and endcap sections is made up of a 1 cm and 5 mm liquid argon active layer, respectively, and is equipped with electrodes that are approximately perpendicular to (in the case of the barrel) or parallel to (in the case of the endcap) the beam axis.

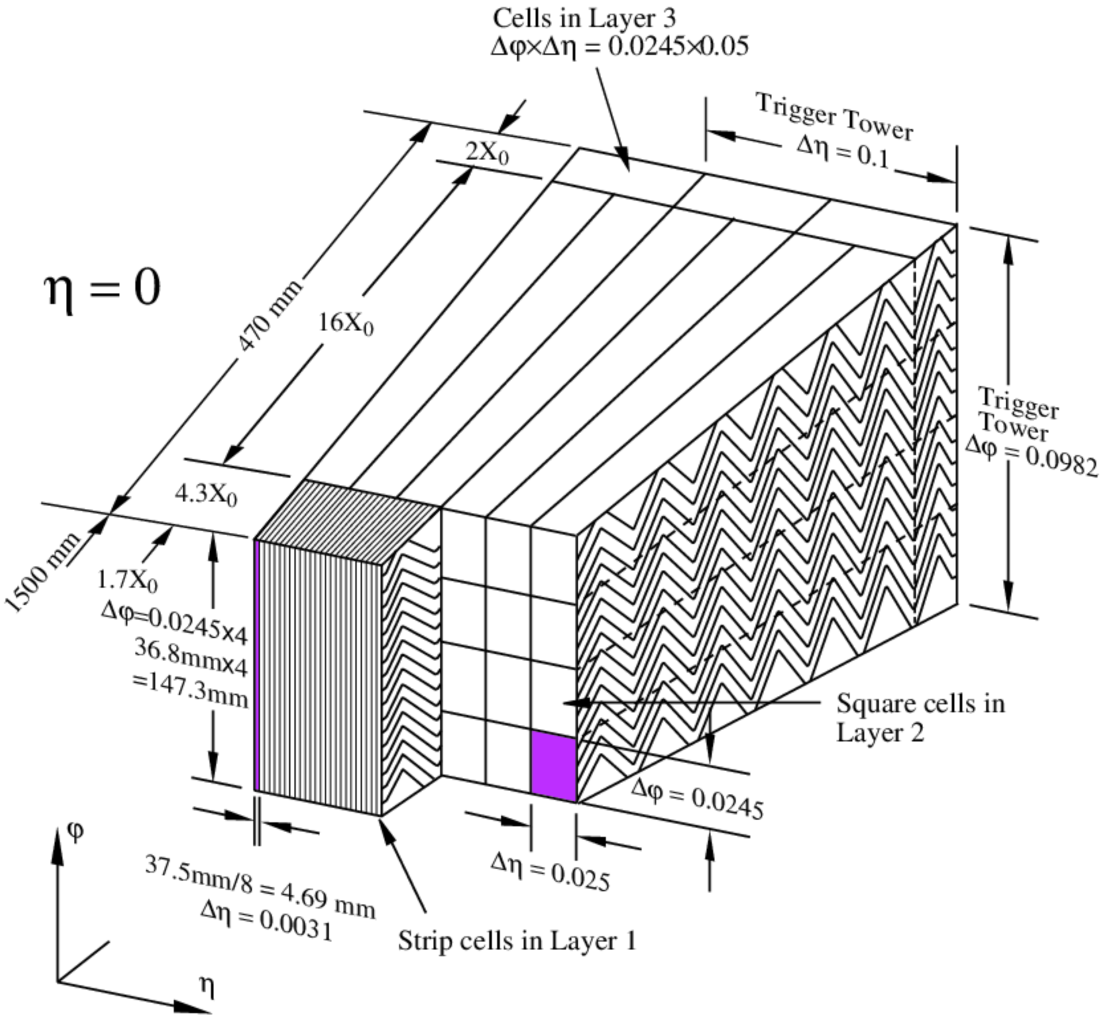

Figure 2.7: Diagram of a LAr EM calorimeter barrel module. It shows the longitudinal segmentation, cell size is shown and the accordion structure [68].

Hadronic Calorimeter

The hadronic calorimeter comprises a barrel part and two endcaps, although different technologies are used for the two components. The barrel part is made of hadronic calorimeter with scintillating tiles, while the endcap part employs copper/liquid argon sampling. This choice of technology was determined by the high sensitivity of the scintillating tiles to radiation in the endcap region and the cost of different configurations. The hadronic tile calorimeter, with a sampling fraction of 4.7 to 1, is a sampling calorimeter made of iron as the absorbing material and polystyrene as the active part. The light produced by particles interacting with iron and scattered in the active material is captured by optical fibers with index shift and processed by photomultiplier tubes. The calorimeter is segmented into four parts, each divided into 64 trapezoidal modules in azimuth (with a segmentation $\Delta\varphi$ of approximately 0.1), and covers the region $|\eta| < 1.7$, with a radial length of 7.4 interaction lengths. Figure 2.8 provides details of a module. The achievable energy resolution for pions is provided in Ref [61] by:

$$\frac{\sigma_E}{E} = \frac{50\%}{\sqrt{E}} \oplus 3\%$$

The hadronic calorimeter based on liquid argon has two end-caps that cover the region of $1.5 < |\eta| < 3.2$. These end-caps are composed of two wheels, each of which contains 64 modules arranged in φ. This calorimeter uses a copper/argon sampling technique, and the granularity in (η, φ) varies depending on the pseudo-rapidity region: $\Delta\varphi = (0.1 \times 0.1)$ for $1.5 < |\eta| < 2.5$ and $(\Delta\eta \times \Delta\varphi) = (0.2 \times 0.2)$ for $2.5 < |\eta| < 3.2$.

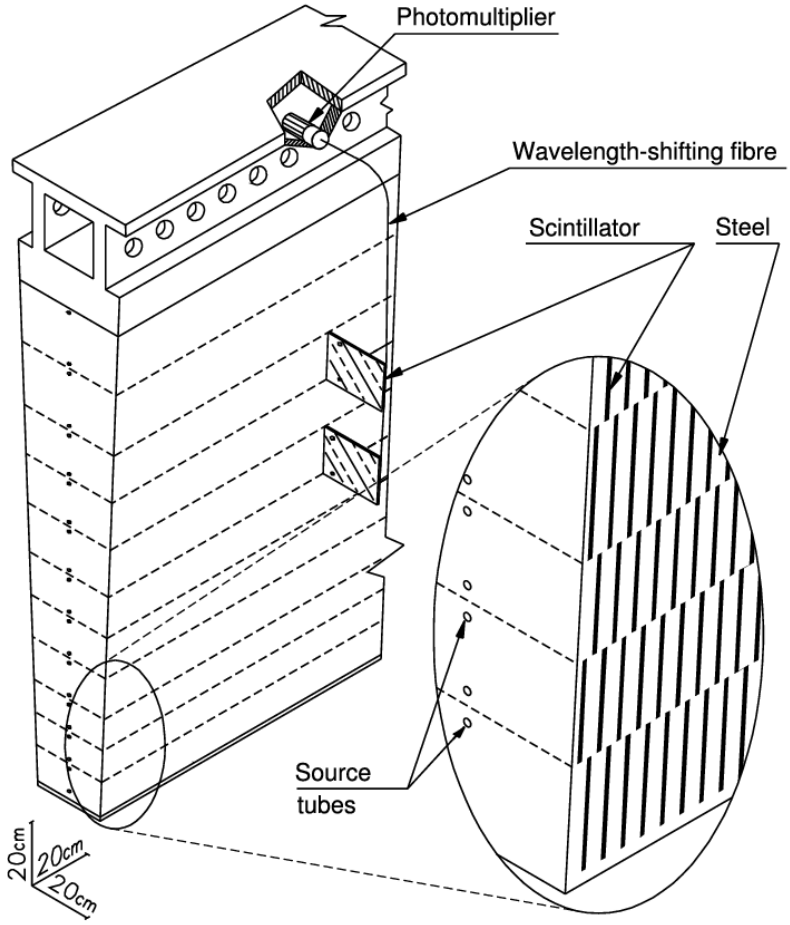

Figure 2.8: Schematic diagram of an ATLAS hadronic tile calorimeter [69].

Muon spectrometers

The muon spectrometers (Figure 2.9) consist of a barrel and an end-cap part, similar to the other sub-detectors mentioned previously. The barrel covers the central regions ($|\eta| < 1$), while the end-cap is designed to detect muons with higher pseudorapidity values up to $|\eta| = 2.7$. These parts are responsible for determining the curved trajectories of the muons caused by the magnetic field generated by the toroidal magnet and measuring their momentum. Two types of detectors are present in each part, including a fast-response detector for the triggering system and a precision detector for measuring muon properties such as pulse and charge. The former type comprises RPC (Resistive Plate Chambers) and TGC (Thin Gap Chambers) detectors, while the latter includes MDT (Monitored Drift Tube) and CSC (Cathode Strip Chambers).

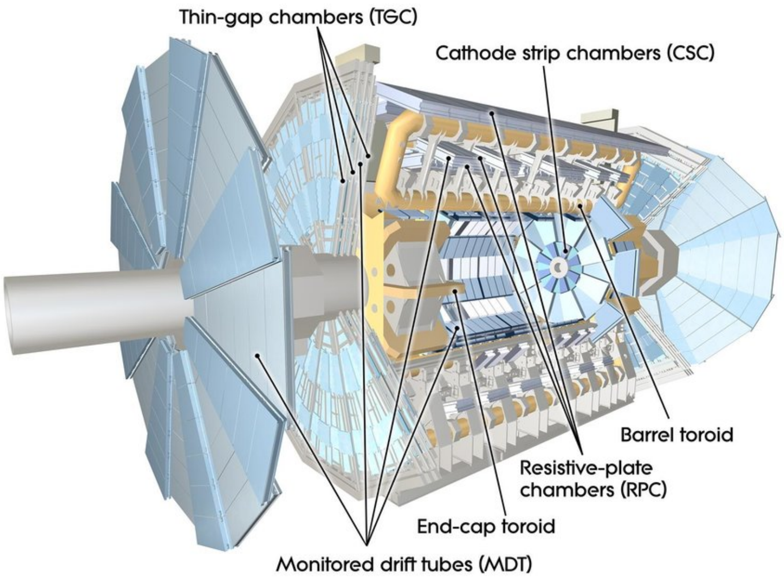

Figure 2.9: Muon spectrometer of the ATLAS detector [70].

2.3.4 Luminosity measurement

Luminosity

The collision of proton bunches involves several quantities, including the instantaneous luminosity L, expressed in units of $cm^{-2}.s^{-1}$ or $fb^{-1}.s^{-1}$. This parameter is used to determine the number of events for a particular process X produced per second, denoted by N_x , which can be calculated as $N_x = L * \sigma_x$, where σ_x represents the total cross-section of process X (measured in fb). However, since new physics phenomena can occur with a low probability, the ATLAS and CMS experiments aim to maximize the number of potential events by requiring a very high instantaneous luminosity. This, in turn, imposes constraints on the proton beam, with L depending solely on its intrinsic properties:

$$L = \frac{N_b^2 n_b f_{\text{rev}} \gamma}{4\pi \varepsilon_n \beta^*} \times F \tag{2.3}$$

This equation involves several parameters that are crucial for understanding proton collisions, including N_b (the number of protons per bunch), n_b (the number of bunches per beam), f_{rev} (the revolution frequency), γ (the Lorentz factor of special relativity), ε_n (the transverse emittance of the beam, which corresponds to the dispersion of the beam in the phase space position-pulse in the transverse plane), β^* (the beta function at the point of collision, which quantifies the amplitude of the envelope of the beam), and F (a geometric factor that depends largely on the crossing angle of the beams). The instantaneous luminosity, which is expressed in $cm^{-2}.s^{-1}$ or $fb^{-1}.s^{-1}$, changes as collisions occur, especially due to a decrease in the number of protons per packet.

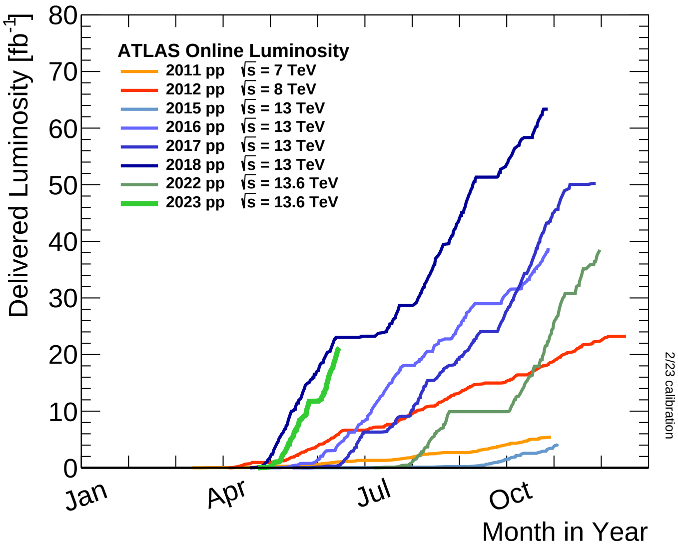

Figure 2.10: Integrated yearly luminosity between 2011 and 2023 for proton operation [71].

Another quantity that is useful in quantifying the amount of data delivered by or recorded by an experiment is the integrated luminosity $\mathcal{L}$. This quantity corresponds to the integral of instantaneous luminosity over time, and is expressed in inverse femtobarns fb^{-1}. The evolution of integrated luminosity for proton collisions between 2011 and 2023 is presented in Figure 2.10, and the evolution for heavy ions in 2015 and 2018 can be seen in Figure 2.11. These values are particularly important for the detection of New Physics, as rare phenomena can occur with low probability, and maximizing the number of potential events requires very large instantaneous luminosities. These high luminosities place constraints on the proton beam that depend primarily on its intrinsic parameters.

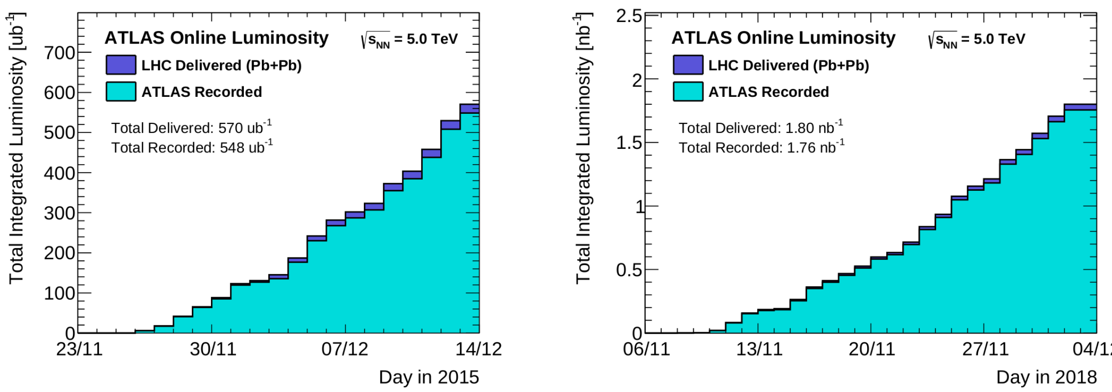

Figure 2.11: Integrated luminosity for 2015 and 2018 for Pb+Pb collision [72]

.

LUCID

The LUCID detector, short for LUminosity measurement using a Cerenkov Integrating Detector, plays a crucial role in measuring the luminosity of the Large Hadron Collider (LHC) during ATLAS experiments. It is the main online luminosity monitor for the ATLAS detector and is located at a distance of 17 meters on each side of the interaction point. This location allows the detector to detect inelastic proton-proton scattering in the forward region.

By measuring the rate of such scattering events, the LUCID detector can provide a precise measurement of the LHC's instantaneous luminosity. This is essential because the luminosity is a fundamental parameter that characterizes the intensity of the collisions occurring in the LHC. The more intense the collisions, the greater the probability of discovering new particles or phenomena.

In addition to LUCID, another detector called ALFA (Absolute Luminosity For ATLAS) is also used to measure luminosity. It is located at a much greater distance from the interaction point, approximately 240 meters on each side. ALFA is designed to measure the absolute luminosity, or the total number of collisions that occur in a given amount of time. This is done by measuring the elastic scattering of protons at very small angles, and then using this measurement to infer the total number of inelastic collisions that occurred during the same time period.

Together, these detectors provide ATLAS with highly accurate measurements of the LHC's luminosity, which is crucial for understanding the results of experiments and for pushing the boundaries of particle physics research.

2.3.5 Trigger system

Collisions between proton packets occur at a nominal rate of 25 ns (50 ns in 2012), resulting in an event frequency of 40 MHz (20 MHz in 2012). However, the majority of these events are not of significant interest since they correspond to events with very little energy in the transverse plane or towards the front. Additionally, the processing, reconstruction, and storage of information from the detectors require more than 25 ns, making it necessary to implement an event filtering system, called the trigger system. [73, 74] This system selects events that are of interest for physics and is based on the information provided by the different ATLAS sub-detectors. The architecture of the trigger system, as illustrated in Figure 2.12, is comprised of two levels, which differ in the nature and precision of the information they use.

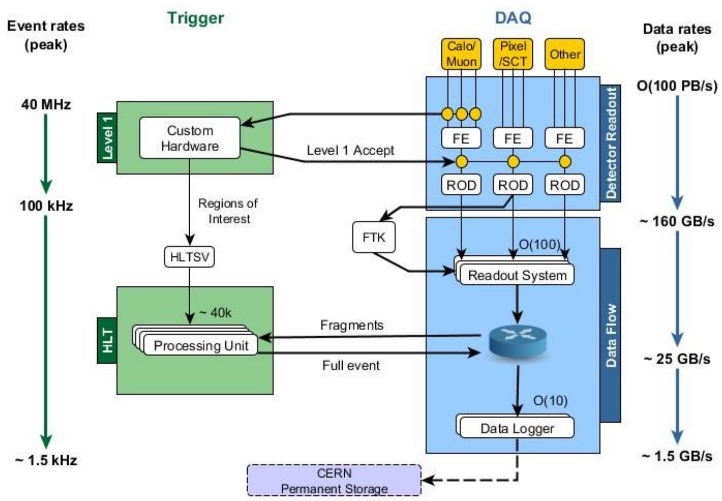

Figure 2.12: The ATLAS Trigger and Data Acquisition (DAQ) System in LHC Run 2 [75].

The Level 1 trigger

The following step [73] in event processing relies on information from calorimeters and muon spectrometers (specifically RPC and TGC). The granularity of the calorimetric information used is coarser than in analyses, with a granularity of 0.1 x 0.1 instead of 0.025 x 0.025 in the (η, φ) plane, such as for the electromagnetic calorimeter. This step identifies regions of interest (ROI), consisting of roughly reconstructed physical objects (e.g. leptons, jets). The number and transverse energy of these objects determine whether or not the event should be transmitted to the HLT. Processing time must not exceed 2.5 µs because collisions occur under nominal conditions every 25 ns, and information is stored in the buffer memory while awaiting processing by the Level 1 system. Delayed decision-making can cause loss of information. This trigger level results in a nominal event frequency of 75 kHz (65 kHz in 2012).

The High Level trigger

The HLT software, a combination of the event filter and HLT used in Run-1 [76], utilizes all detector information [74] for software-based decision-making, and the reconstruction algorithms leverage this increased granularity to refine object reconstruction. In particular, the use of internal detectors improves electron identification. At this stage, event frequency is reduced to approximately 1 kHz. At the HLT, events are partitioned into multiple "streams," each comprising the output from several trigger chains. A single stream may include all events that pass an electron or muon trigger, for example. Events that meet both L1 and HLT trigger requirements may be added to multiple streams. At the outset of a run, the number and contents of the set of streams are determined. There is typically a "debug" stream that is reserved for events that could not be processed in the allotted time for a trigger decision.

2.3.6 Data, Simulation & Object Reconstruction And Selection

Data

The ATLAS experiment collects data in runs, each with a unique identifier, and is further divided into luminosity blocks. These blocks are annotated with data quality information, which can be used to construct a "good run list" (GRL) for use in physics analysis. Once collected, the data undergoes processing using the ATLAS software framework Athena [77], which is the same software used for digitization and reconstruction of simulated events. The processing involves several steps that utilize CERN's computing resources [78] for storage and computation. The final output of this processing is Analysis Object Data (AOD) files, which contain information about physics objects such as electrons and muons, including their properties like energy, momentum, and position. These AOD files can be further processed to produce Derived Analysis Object Data (DAOD) files, such as the ones used in the analysis presented in this work.

Simulation of the ATLAS Detector

Following the event generation stage, the detector simulation aims to model the interaction between the produced particles and the detector material, as well as the response of the detector electronics. Firstly, a geometry of the detector is created by dividing it into basic volumes that represent all parts, whether sensitive or not. In the case of the ATLAS detector, this consists of approximately 4.8 million volumes that are distributed almost uniformly among the internal detectors (38%), the calorimeters (32%), and the muon spectrometers (30%) [79]. The simulated detector is modulated by the real operating conditions of the ATLAS detector, which are recorded in a database resembling Oracle, allowing the simulation of faults and a faithful reproduction of the recorded data.

GEANT4 [80] is the main software used for the complete simulation of the ATLAS detector. This method provides a detailed description of the detector and physical processes but requires significant computational time. Therefore, a simplified version called ATLFASTII [81] is available to speed up the calculation time by a factor of 20 to 40 [79]. ATLFASTII is known as rapid, and its description of the calorimetric system, especially the electromagnetic calorimeter with liquid argon, differs from the complete simulation. A library of electromagnetic and hadronic showers [82] is used instead of simulating particle interactions with the detector material. This library is created using nearly 30 million events with different longitudinal or transverse profiles of the showers, modeled from photons for electromagnetic showers and charged pions for hadronic showers. The objects' properties obtained from this simplified simulation are very similar to those obtained from the complete simulation, with a difference in the energy scale of the jets ranging from 1 to 2%[79].

The response of the simulated detector is then converted into a format that matches the actual data, so the physical object reconstruction phase, including electrons, muons, jets, and missing transverse energy, can be performed in the same way in both simulated and actual data samples.

Object reconstruction

In both Monte Carlo simulation and ATLAS data, the information recorded by the detector's electronics cannot be directly utilized by physicists for analysis purposes. Instead, reconstruction algorithms are employed to obtain physical objects such as electrons, muons, jets, and missing transverse energy. These algorithms make use of the information gathered by all the sub-detectors in the ATLAS detector, including the internal detectors, muon spectrometers, and calorimeters, both electromagnetic and hadronic. The details provided here are mostly based on Ref [83]. Since this work mainly utilizes two objects, electrons and photons. Only those will be described in this section.

Reconstruction of Electrons and Photons

The reconstruction of electrons and photons is carried out in the central region ($|\eta| < 2.5$) using a procedure outlined in Figure 2.13. This procedure replaces the sliding window algorithm [84], which employs fixed-size clusters of calorimeter cells.

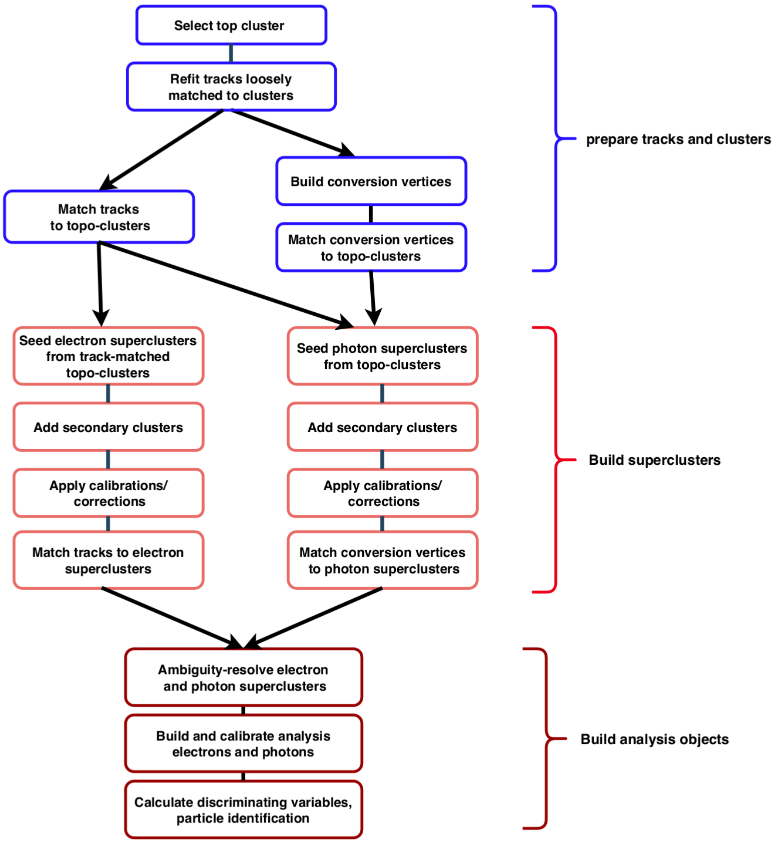

Figure 2.13: Flow diagram for the electron and photon reconstruction based on superclusters [83].

Instead, the new algorithm uses dynamic and variable-size clusters known as superclusters, and can be explained in the following steps:

- **Preparing tracks and clusters:** The initial step in preparing tracks and clusters involves creating topo-clusters in the EM and hadronic calorimeters, using a set of noise thresholds. This requires the cell that initiates the cluster to have a significance $|S^{\text{EM}}_{\text{cell}}| \geq 4$,

$$S^{\text{EM}}_{\text{cell}} = \frac{E^{\text{EM}}_{\text{cell}}}{\sigma^{\text{EM}}_{\text{noise cell}}}$$

  where $E^{\text{EM}}_{\text{cell}}$ is the cell energy at the EM scale and $\sigma^{\text{EM}}_{\text{noise cell}}$ is the expected cell noise. The expected cell noise includes electronic noise and an estimate of the pile-up noise corresponding to the average instantaneous luminosity expected for Run 2, and is specified for each cell. Once a seed cell is found, neighboring cells of the seed are iteratively added if their energy is twice as high as their noise level. After this step, all neighboring cells with energy above their noise level are added to form a topological calorimeter cluster. The next step involves selecting electromagnetic topology, followed by matching the reconstructed tracks and conversion-vertex from the inner detector to the electromagnetic using a similar method to the one used in the sliding windows algorithm [84]. The reconstruction of the electron and photon proceeds simultaneously, assuming a photon and an electron.

- **Building superclusters** The reconstruction process of electron and photon superclusters occurs independently. To identify a photon, a seed cluster must have a minimum energy of 1.5 GeV. Meanwhile, for electrons, a seed cluster must have a minimum energy of 1GeV and a corresponding track that has at least four hits in the SCT. Once a seed cluster is identified, satellite clusters are added from all remaining clusters that have not been used. These satellite clusters are assumed to represent secondary electromagnetic showers from the same physical object, and their energy must be lower than that of the seed cluster. Typically, a cluster is added as a satellite cluster if it is located within a $\Delta\eta \times \Delta\varphi = 0.075 \times 0.125$ window around the barycenter of the seed cluster. In the case of converted photons, additional clusters are added that share the same conversion vertex or any track from the conversion vertex of the seed cluster. For electrons, satellite clusters are searched for within a $\Delta\eta \times \Delta\varphi = 0.125 \times 0.3$ window, and they must have the same best-matched track as that of the seed cluster.

- **Building analysis objects:**

  Once a supercluster is formed, the algorithm searches for the next seed cluster and repeats the process until all electromagnetic topological clusters are examined. Then, the energy of the supercluster is calculated using only the cells in the ECAL that are associated with this cluster. The size of the supercluster is limited to three or five cells in the η direction in the barrel or end-cap region, respectively, centered around the barycenter. This limitation excludes cells that do not contain a significant portion of the particles' energy, but may contain energy from other physics objects. After that, the energy of the supercluster is calibrated using an MVA technique and the position of the barycenter is corrected [83]. The algorithm then matches reconstructed tracks and conversion vertices to the superclusters to determine the particle type. As the superclusters for photons and electrons are formed simultaneously, there may be ambiguities, which the algorithm attempts to resolve through a dedicated procedure. If an ambiguity cannot be resolved, the physics object is discarded in this analysis. Finally, the energy is recalibrated based on the particle type using the procedure described in Ref [83].

2.4 Conclusion

This chapter provides an overview of the experimental setup that was used to collect the data analyzed in this thesis. The LHC accelerator complex is capable of accelerating and colliding protons and heavy ions at four interaction points, generating vast amounts of data for the four experiments. The ATLAS detector is a highly versatile instrument that is composed of multiple sub-detectors, each of which has a specific function. This chapter describes these sub-detectors and their functions in detail. Additionally, we provide an overview of the data collection and simulation techniques that were employed in the context of the ATLAS experiment.

Chapter 3

Light-by-light Analysis

3.1 Introduction

To initiate the analysis of our process, the first step involves selecting the Data and Monte Carlo samples for our study. We then examine the cut-flow applied to both sets, which provides a comprehensive overview of the selection criteria implemented to obtain clearer information for analysis. Additionally, we apply various scale factor corrections to ensure accurate results.

Next, we address the crucial aspect of determining the major systematic uncertainties, as they significantly impact subsequent steps of the analysis. Subsequently, we present the obtained results, which primarily include kinematic distributions for different variables. Additionally, we showcase the fiducial cross section, the correction factor, and the contribution of systematic uncertainties. Another noteworthy result pertains to the differential cross sections, specifically focusing on three distributions: diphoton invariant mass, diphoton absolute rapidity, and diphoton $|\cos(\theta^*)|$.

In order to derive these differential cross sections, we employ a bin-by-bin unfolding technique, which allows us to reconstruct the data distribution at the particle-level and compare it with the true distributions predicted by the theory. Furthermore, we perform a fit to our data on the signal-plus-background using a profile likelihood function. The software used for the fitting is TRExFitter as it is providing a detailed analysis of the fit by presenting important plots such as Pre-fit, Ranking plots, Post-fit, and more. Then, we report the significance of our Light-by-light signal as a measure of its statistical significance. Finally, we set limits on the cross section for the production of ALPs.

3.2 Data & Monte Carlo samples used

The data used for this analysis was obtained from Pb+Pb collisions at a center-of-mass energy of $\sqrt{s_{NN}} = 5.02$ TeV, recorded with the ATLAS detector at the LHC. The data was recorded in 2015 with an integrated luminosity of 0.48 nb^{-1} and in 2018 with an integrated luminosity of 1.73 nb^{-1}, resulting in a full set of data equivalent to an integrated luminosity of 2.2 nb^{-1}, with an uncertainty of 3.2 % [53]. The 2015 data underwent reprocessing using release 21 of the Athena software [79] to ensure compatibility for its combination with the 2018 data. The Table 3.1 presents the number of runs for each year, along with the integrated luminosity and the corresponding GRL (Good Run List) used in each data set.

Run numbers	Year (Integrated Luminosity)	GRL used
00286711, 00286717, 00286748, 00286767, 00286834, 00286854, 00286908, 00286967, 00286990, 00286995, 00287038, 00287044, 00287068, 00287222, 00287224, 00287259, 00287270, 00287281, 00287321, 00287330, 00287334, 00287378, 00287380, 00287382, 00287560, 00287594, 00287632, 00287706, 00287728, 00287827, 00287843, 00287866, 00287924, 00287931.	2015 (0.48 nb^{-1})	data15_hi.periodAllYear _DetStatus-v105-pro22-13_Unknown_PHYS_) HeavyIonP_All_Good.xml
00365602, 00365678, 00365681, 00365709, 00365752, 00365834, 00365914, 00365932, 00366011, 00287706, 00366029, 00366092, 00366337, 00366383, 00366476, 00366526, 00366627, 00366805, 00366878, 00366994, 00367134, 00367165, 00367170, 00365498, 00365502, 00365512, 00365573, 00365627, 00366142, 00366268, 00366413, 00366528, 00366691, 00366754, 00366860, 00366919, 00366931, 00367023, 00367099, 00367233.00367273, 00367318, 00367321, 00367363, 00367364, 00367365, 00367384.	2018 (1.73 nb^{-1})	data18_hi.periodAllYear _DetStatus-v106-pro22-14_Unknown_PHYS_ HeavyIonP_All_Good _ignore_TOROIDSTATUS.xml

Table 3.1: 2015 and 2018 Pb+Pb stable beam runs [85].

Light-by-light signal events were generated at leading order (LO) using SuperChic v3.0 , which is a Fortran-based Monte Carlo event generator for a wide range of final states, via QCD and photon-initiated production, with pp, pA, and AA beams, in our case, we use PbPb beams [86]. These signal events take into account box diagrams with leptons and quarks (such as the diagram in Figure 1.5) and $W^{\pm}$ bosons, including interference effects. However, next-to-leading-order QCD and QED corrections were not considered. These corrections contribute to the theoretical uncertainty and are of the order $1-3$ % in the corresponding invariant mass range [87, 88].

Another sample of LbyL signal was generated by using calculations from the reference [89], where cross sections for diphoton production in (semi)exclusive PbPb collisions, relevant to the LHC, were calculated and then convoluted with the Pb+Pb photon flux from the STARlight 2.0 Monte Carlo (MC) generator [90, 91], which is a simulation program for ultra-peripheral collisions of relativistic ions. The main source of theoretical uncertainty in the cross-section is the limited understanding of the nuclear electromagnetic form-factors and their associated initial photon fluxes. An estimated uncertainty of 10 % has been determined for the measurement within a defined fiducial phase space [19, 92].

The main difference between the nominal and alternative signal predictions lies in the implementation of the non-hadronic overlap condition of the Pb ions. In SuperChic v3.0, for Pb+Pb impact parameters between 15-20 fm, the probability of exclusive $\gamma\gamma$ interactions increases gradually without abrupt changes while it becomes maximal for larger values. The alternative prediction, on the other hand, fully suppresses these interactions for impact parameters below 14 fm when two nuclei overlap during the collision. This results in a much higher cross sections in PbPb collisions than in the nominal signal calculation.

The exclusive diphoton final state can also be produced via the strong interaction through a quark loop in the exchange of two gluons in a colour-singlet state. This process is called central exclusive production (CEP). Its background contribution, gg $\rightarrow \gamma\gamma$, was generated with SuperChic v3.0 [86] and has a large theoretical uncertainty, O(100%), related to the modelling of the rapidity gap survival probability [93]. This is a result that pertains solely to leading order (LO), and we anticipate that higher order corrections will increase the cross-section by a correction of this order [86]. Furthermore, additional limitations on the normalisation of this background process were determined using a specific control region directly from the data.

The production of exclusive dielectron pairs from the reaction Pb+Pb ($\gamma\gamma$) $\rightarrow$ Pb ($*$) + Pb ($*$) e^+e^- are used for various calibration studies in the analysis, in particular to validate the electromagnetic calorimeter energy scale and resolution. The $\gamma\gamma \rightarrow e^+e^-$ process is a potential background, when both leptons are reconstructed as photons. It was modelled with the STARlight v2.0 MC generator [90, 91], where the cross section is computed by combining the Pb+Pb photon flux with the leading-order (LO) formula for $\gamma\gamma \rightarrow e^+e^-$.

Other background with lesser contributions were also generated. The background from two-photon production of quark-antiquark pairs was estimated using Herwig++ 2.7.1 [94] where the Equivalent Photon Approximation (EPA) formalism in pp collisions was implemented. This process was computed at leading order in perturbation theory. The sample was then normalised to cover the fluctuations in equivalent photon fluxes between the Pb+Pb and pp cases. The background contribution from a related process to the production of exclusive dielectron pairs, $\gamma\gamma \rightarrow \tau^+\tau^-$, was modelled using STARlight v2.0 interfaced with Pythia 8.212 [95] for the simulation of τ-lepton decays. It is a lowest order calculation yet the result includes room for an additional contribution to the cross-section, due to higher order corrections.

STARlight v2.0 was used to produce ALP signal events across ALP mass values (m_a) spanning from 5 to 100 GeV, utilizing a mass increment of 1 GeV for $5 < m_a < 30$ GeV, and 10 GeV increment for $m_a > 30$ GeV. Across all simulated samples, the detector resolution surpasses the width of the ALP resonance [53].

All generated events were passed through a GEANT4 [80] based detector simulation [79] and were reconstructed with the standard ATLAS reconstruction software.

The Table 3.2 presents the data and Monte Carlo samples used, along with their sources, the order of correction, and the associated uncertainties.

Data & MC samples	Source	Order of correction/uncertainty
Data 2018 + 2015 (2.2 nb^{-1})	Pb+Pb collisions with $\sqrt{s_{NN}}$ = 5.02 TeV in 2015 & 2018 at the LHC (Run 2)	total uncertainty of 3.2%
LbyL signal	SuperChic v3.0	Leading order (LO) Next-to-leading order (NLO) corrections for uncertainties
Alternative LbyL signal	STARlight 2.0	- 10% Uncertainty (Higher-order corrections)
CEP gg $\to \gamma\gamma$ background	SuperChic v3.0	LO
QED $\gamma\gamma \to e^+e^-$ background	STARlight 2.0	LO
$\gamma\gamma \to q\bar{q}$ background (lesser contribution)	Herwig++ 2.7.1	LO
$\gamma\gamma \to \tau^+\tau^-$ background (lesser contribution)	STARlight v2.0 interfaced w/ Pythia 8.212	LO
ALP signal	STARlight 2.0	-

Table 3.2: Data & MC samples details.

3.3 Event Selection

In this section, we outline the various criteria used to select events that meet the requirements for the light-by-light signal region. A typical cut-flow for this analysis is presented in Figure 3.1, illustrating the sequential application of these criteria. The Table 3.4 shows the number of events after each step of that cut-flow.

3.3.1 Trigger

The trigger strategy [96] is different between 2015 and 2018 data

2015 data: For 2015, the trigger configuration was:

- HLT_gg_upc_L1TE5_VTE200

  and it is based on the following requirements:

- A Level-1 seed requires total E_T between 5 and 200 GeV in the entire calorimeter,
- MBTS veto, i.e. maximum one hit in the inner ring of the MBTS detector,
- Low activity in the ID, defined by a maximum number of 10 hits in the Pixel Detector (imposed in hi_gg_upc)

2018 data: Candidate diphoton events were recorded in the Pb+Pb run in 2018 using a dedicated trigger for events with moderate activity in the calorimeter but little additional activity in the entire detector. The primary trigger for low-E_T diphoton events uses a logical OR of two dedicated triggers having different Level-1 seeds and the same HLT selection. These two triggers are:

- HLT_hi_upc_FgapAC3_hi_gg_upc_L1TAU1_TE4_VTE200
- HLT_hi_upc_FgapAC3_hi_gg_upc_L12TAU1_VTE50

  They include three sets of requirements:

- A Level-1 seed is one of the following:
  – L1_TAU1_TE4_VTE200, requiring coincidence of minimum one EM cluster of $E_T > 1$ GeV and total E_T between 4 and 200 GeV in the entire calorimeter,
  – L1_2TAU1_VTE50, requiring at least 2 EM clusters of $E_T > 1$ GeV and total E_T in the entire calorimeter below 50 GeV,
- FCal veto, i.e. rejection of events with $\Sigma\ E_T^{FCal} > 3$ GeV on any side of FCal (imposed in hi_upc_FgapAC3),
- Low activity in the ID, defined by a maximum number of 15 hits in the Pixel Detector (imposed in hi_gg_upc).

3.3.2 Final Selection

The preselected events in this analysis require the presence of exactly two photons that satisfy the previously mentioned selection criteria [96]. Additionally, the diphoton invariant mass must be greater than 5 GeV. To suppress the background from the process $\gamma\gamma \rightarrow e^+e^-$, a veto is imposed on charged-particle tracks that meet specific requirements ($p_T >$ 100 MeV, $|\eta| < 2.5$, at least one hit in the Pixel detector, and at least six silicon hits in total).

To further constrain poorly reconstructed electron tracks, candidate events must not have any "pixel tracks," which are reconstructed solely using information from the Pixel detector. Candidate pixel tracks must have $p_T > 50$ MeV, $|\eta| < 2.5$, and at least three hits in the Pixel detector. To avoid fake pixel tracks due to noise, only pixel tracks within $\Delta\eta < 0.5$ from the photons are considered.

These requirements significantly reduce the background from fake photons originating from the dielectron final state, as demonstrated by simulation. They have minimal impact on the $\gamma\gamma \rightarrow \gamma\gamma$ signal events, with an efficiency of 93% for the track veto and 99% for the pixel track veto. This is because the probability of photon conversion in the Pixel detector is relatively low, and converted photons are initially suppressed at low transverse energy (E_T) due to the presence of low-momentum electron tracks.

To further suppress other sources of fake photon backgrounds, such as calorimeter noise and cosmic-ray muons, the transverse momentum of the diphoton system ($p_T^{\gamma\gamma}$) is required to be below 1 GeV for $m_{\gamma\gamma} < 12$ GeV and below 2 GeV for $m_{\gamma\gamma} > 12$ GeV. An additional requirement on acoplanarity (Aco = $(1 - |\frac{\Delta\Phi_{\gamma\gamma}}{\pi}|)$ is used to reduce the real photon background from CEP gg $\rightarrow \gamma\gamma$ reactions, which is expected to be the dominant source of background with two photons in the final state [11, 19].

For the purpose of validating the electromagnetic (EM) calorimeter energy scale and resolution, exclusive dielectron pairs from the reaction Pb+Pb $(\gamma\gamma) \rightarrow$ Pb $(*)$ + Pb $(*)$ e^+e^- are used in the analysis. These $\gamma\gamma \rightarrow e^+e^-$ candidates are selected by applying the same trigger as in the diphoton selection. Electrons are reconstructed from EM energy clusters in the calorimeter matched to tracks in the inner detector [84]. The electrons must have transverse energy $E_T > 2.5$ GeV, pseudorapidity $|\eta| < 2.47$ (excluding the calorimeter transition region $1.37 < |\eta| < 1.52$), and meet loose identification criteria based on shower shape and track-quality variables [84]. The $\gamma\gamma \rightarrow e^+e^-$ events are selected by requiring exactly two oppositely charged electrons, no additional charged-particle tracks from the interaction region, and a dielectron acoplanarity (Aco) less than 0.01.

The table below (Table 3.3) summarizes the selections applied.

Signal/Background	Selections
Signal region	2 photons with E_T > 2.5 GeV and $\mid \eta \mid$ < 2.37 & Invariant mass $m_{\gamma\gamma}$ >5 GeV
QED background	Track veto p_T > 100 MeV & pixel veto p_T > 50 MeV
CEP background	Diphoton transverse momentum: $p_{\gamma\gamma}$ < 1 GeV for $m_{\gamma\gamma}$ < 12 GeV $p_{\gamma\gamma}$ < 2 GeV for $m_{\gamma\gamma}$ > 12 GeV Acoplanarity < 0.01

Table 3.3: Selections table.

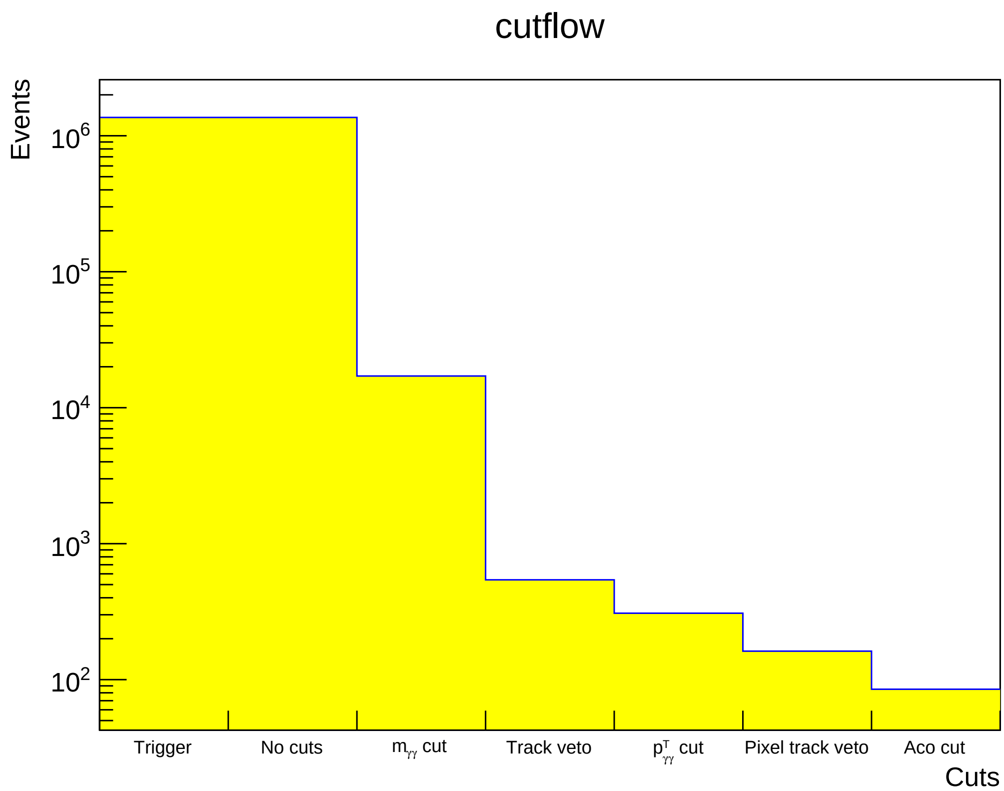

Figure 3.1: Cut-flow applied to the 2018 Data.

Cuts	Trigger	No cuts	$m_{\gamma\gamma}$ cut	Track veto	$p^T_{\gamma\gamma}$ cut	Pixel track veto	Aco cut
Events	1363476	1363476	17100	542	308	162	85

Table 3.4: Number of events remaining after each selection applied to the 2018 data.

3.4 Scale factor corrections

3.4.1 Photon reconstruction

Photons are reconstructed by utilizing electromagnetic (EM) clusters in the calorimeter and tracking information obtained from the inner detector (ID), which aids in identifying photon conversions [97]. To ensure the selection of high-quality photons, certain requirements are imposed to exclude EM clusters with excessive energy from malfunctioning calorimeter cells. Additionally, a timing requirement is imposed to discard out-of-time photon candidates. To account for energy loss upstream and both lateral and longitudinal shower leakage, a photon-specific energy calibration [83] is applied to the candidates. Furthermore, in order to address any potential discrepancies in modeling the properties of associated EM showers, a dedicated correction [83] is implemented for photons in Monte Carlo (MC) samples.

3.4.2 Photon particle-identification

Photon particle identification (PID) in this analysis relies on various shower-shape variables [53]. Only photons with transverse energy (E_T^{γ}) greater than 2.5 GeV and a pseudorapidity ($|\eta|$) within the range of $|\eta| < 2.37$ are considered. The exclusion of the calorimeter transition region, $1.37 < |\eta| < 1.52$, ensures that the photon candidates pass through the regions of the electromagnetic (EM) calorimeter where the first layer is segmented into narrow strips. This segmentation enables effective discrimination between genuine prompt photons and photons originating from the decay of neutral hadrons. A consistent photon PID efficiency of 95% is maintained across different pseudorapidity regions with respect to reconstructed photon candidates.

The photon identification is based on a neural network trained using background photons extracted from data and photons from the signal Monte Carlo (MC) samples as previously utilized in the prior ATLAS measurement [21]. This PID methodology enables the rejection of EM energy clusters caused by calorimeter noise and cosmic-ray muons with an efficiency of 95%. It also helps choosing a purer sample of photons compared to the cut-based photon PID used in pp collisions [79].

Figures 3.2 and 3.3 present the kinematic distributions of the dielectron system after applying the e^+e^- event selection for the 2018 and 2015 data, respectively. The shaded band represents the uncertainties in the egamma resolution and scale, as provided by the EGamma CP group. The observed data show reasonable agreement with the STARlight prediction. In total, approximately 30,000 candidate events were observed in the 2018 data and 7,000 in the 2015 data.

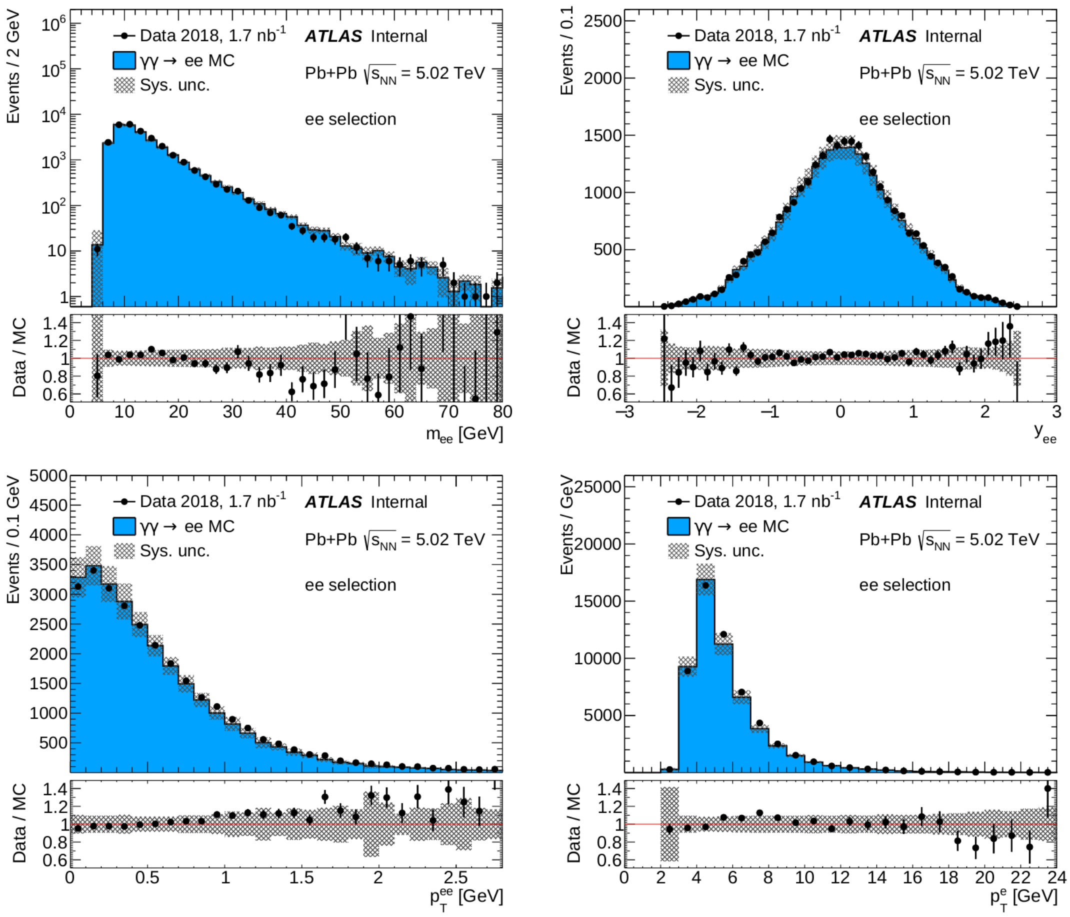

Figure 3.2: Kinematic distributions for event candidates of $Pb + Pb(\gamma\gamma) \rightarrow Pb(*) + Pb(*)e^+e^-$ in the 2018 data set are shown: dielectron mass (top-left), dielectron rapidity (top-right), dielectron p_T (bottom-left), and electron transverse energy (bottom-right). The data points are compared to the MC expectations represented by histograms. The simulation prediction is scaled to the same integrated luminosity as the data. Shaded bands indicate the systematic uncertainties arising from electron energy scale and resolution, electron reconstruction and identification, and trigger efficiency. The lower panels illustrate the ratio of data to MC predictions. Note that some values lie outside the range of the plot [53].

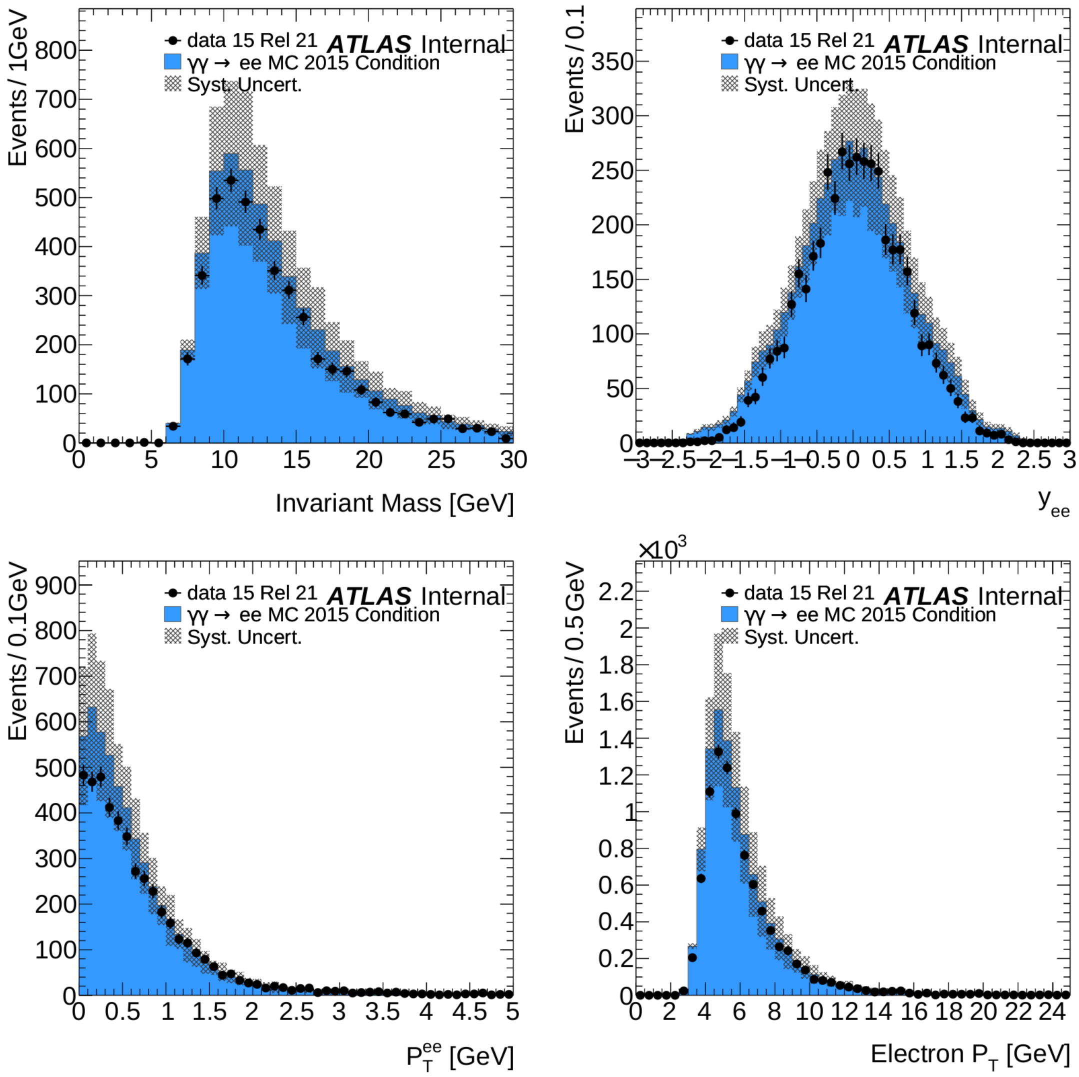

Figure 3.3: Kinematic distributions for event candidates of $Pb + Pb(\gamma\gamma) \rightarrow Pb(*) + Pb(*)e^+e^-$ in the 2015 data set are shown: dielectron mass (top-left), dielectron rapidity (top-right), dielectron p_T (bottom-left), and electron transverse energy (bottom-right). The data points are compared to the MC expectations represented by histograms. The simulation prediction is scaled to the same integrated luminosity as the data. Shaded bands indicate the systematic uncertainties arising from electron energy scale and resolution, electron reconstruction and identification, and trigger efficiency. The lower panels illustrate the ratio of data to MC predictions. Note that some values lie outside the range of the plot [53].

3.5 Systematic Uncertainties

3.5.1 Trigger efficiency

The efficiency of the trigger has been determined by analyzing $\gamma\gamma \to e^+e^-$ events produced from exclusive e^+e^- production [96]. To estimate the mean value of the trigger efficiency and its systematic uncertainty, three event selection criteria are employed: nominal, loose, and tight. For each selection, two tracks with opposite signs, two egamma clusters matched to tracks, and $\Sigma\ E_T^{FCal}$ lower than the noise level plus 4σ on each side of FCal are required.

3.5.2 Photon reconstruction and PID efficiency

The uncertainty associated with photon reconstruction and PID efficiencies is evaluated by parameterizing the scale factors as a function of the photon pseudorapidity, rather than the photon transverse momentum [96]. This introduces a 1.69% impact on the C factor for photon reconstruction corrections and a 1% impact for photon PID corrections, which is considered as a systematic uncertainty. To cross-validate the results, the photon PID efficiency correction factors obtained from the FSR photon sample are compared to the correction factors derived from $\gamma\gamma \to e^+e^-$ (γ) bremsstrahlung photons. The difference between them, when propagated to the overall correction factor, is found to be below 1% and is treated as a systematic uncertainty. The statistical uncertainty associated with photon reconstruction and PID efficiency corrections is propagated using the pseudo-experiment method, wherein the correction factors are randomly varied in a set of pseudo-experiments based on their mean and standard deviation. This variation has a negligible impact on the C factor.

3.5.3 Photon energy scale and energy resolution

The uncertainties associated with the photon energy scale and resolution are obtained from the official EGamma CP tool [98]. The impact of these variations on the simulated signal yield is estimated to be 1% for energy scale variations and 1% for energy resolution variations.

3.5.4 Alternative signal MC sample

The uncertainty arising from the selection of the signal Monte Carlo (MC) generator is evaluated by utilizing an alternative signal MC sample, as described in subsection 3.2. A discrepancy of 1% in the C-factor value between these samples is considered as the systematic uncertainty.

3.6 Results

3.6.1 Kinematic distributions

Upon applying the signal selection criteria, a total of 97 events are observed in the dataset. The expected number of signal events is 45 ± 2, while the expected number of background events is 27 ± 5. Figure 3.4 display the photon kinematic distributions for events that meet all selection criteria. The ratio of data to MC demonstrates that our model is in good agreement with the data, although there are some slight excesses observed at certain points around the peaks. These excesses can be attributed to one of two factors:

- Either we have insufficient data to accurately account for the observed excesses.
- or we need to consider contributions from beyond the standard model to explain these deviations.

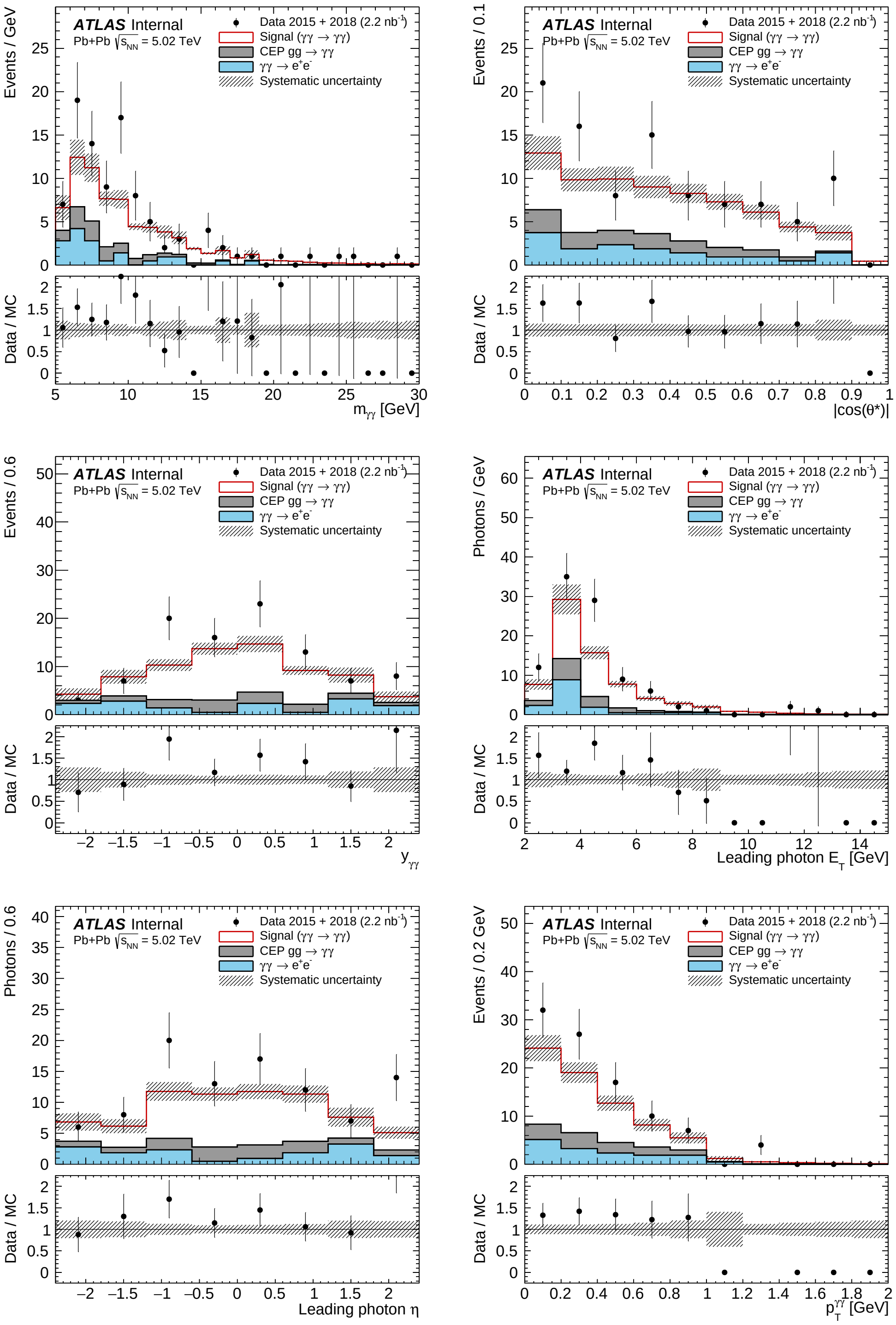

Figure 3.4: Kinematic distributions for $\gamma\gamma \to \gamma\gamma$ event candidates: diphoton invariant mass (top-left), diphoton $| cos(\theta^*) |$ (top-right), diphoton rapidity (mid-left), leading photon transverse energy (mid-right), photon pseudorapidity (bottom-left), diphoton transverse momentum (bottom-right). Data (points) are compared to the sum of signal and background expectations (histograms). Systematic uncertainties on the signal and background processes, excluding that on the luminosity, are denoted as shaded bands.

3.6.2 Fiducial cross section

The cross section for the $\gamma\gamma \to \gamma\gamma$ process is measured within a fiducial phase space, defined by the following criteria applied at the reconstruction level for the diphoton final state: Invariant mass $m_{\gamma\gamma}$ >5 GeV both photons are required to have $|\ \eta\ | < 2.37$ and a transverse momentum (p_T) greater than 2.5 GeV. The invariant mass of the diphoton system must be greater than 5 GeV, with a transverse momentum ($p^T_{\gamma\gamma}$) below 1 GeV. Additionally, the photons must satisfy an acoplanarity requirement of Aco < 0.01.

The calculation of the integrated fiducial cross section, experimentally, is performed using the following formula:

$$\sigma_{\text{fid}} = \frac{N_{\text{data}} - N_{\text{bkg}}}{C \times \int L\ \text{d}t} \tag{3.1}$$

where N_{data} = 97 represents the number of selected events in the data, N_{bkg} = 27 ± 5 corresponds to the number of background events, $\int L\ \text{d}t = 2.22 \pm 0.07\ nb^{-1}$ represents the integrated luminosity of the data sample, and C is the overall correction factor that considers efficiencies and resolution effects. The C factor is defined as the ratio of the number of reconstructed MC signal events passing the selection to the number of generated MC signal events that satisfy the fiducial requirements.

$$C = \frac{N^{\text{Reco}}}{N^{\text{Truth}}} \tag{3.2}$$

The calculated value of C is found to be: C = 0.2605 ± 0.0120. The primary source of inefficiency is attributed to the trigger and photon reconstruction inefficiencies. The uncertainty in C is estimated by varying the data/MC correction factors within their respective uncertainties, particularly for the photon reconstruction/PID efficiency, photon energy scale/resolution, and trigger efficiency, as detailed in section 3.5.

Table 3.5 provides a summary of the different uncertainties associated with the C factor.

The measured integrated fiducial cross section is σ^{fid} = 121.53 ± 17.03 (stat.) ± 9.51 (syst.) ± 3.83 (lumi.) nb, while the theoretical predicted values for our nominal (SuperChic 3.0 generated) and alternative (STARlight 2.0 generated) signals are respectively 78 ± 5.93 and 80 ± 8 nb.

The main source of theoretical uncertainty in the cross section arises from the limited knowledge of nuclear (EM) form-factors and the associated initial photon fluxes. This uncertainty is extensively studied in reference [92], and it is estimated to be around 10% within the fiducial phase space of the measurement. Importantly, this uncertainty does not exhibit a dependence on the diphoton mass for masses below 100 GeV. Another component of the theoretical uncertainty stems from higher-order corrections, which are not accounted for in the calculations. These corrections contribute to an additional uncertainty of approximately 1-3% in the relevant invariant mass range [87, 88].

Figure 3.5 shows the measured fiducial cross section for the $\gamma\gamma \to \gamma\gamma$ process and the predicted values for different MC generators.

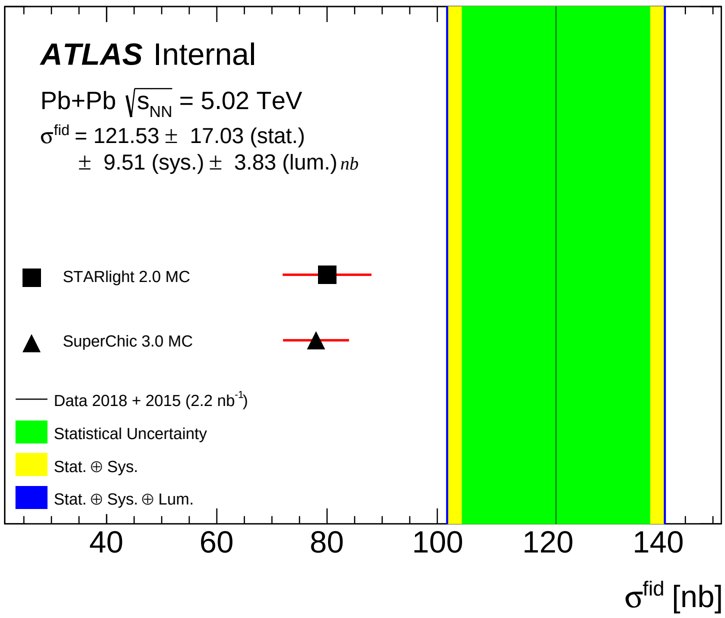

Figure 3.5: Measured fiducial cross-section with various theoretical predictions. Theoretical predictions are indicated as points with the error bar denoting uncertainties. The central value of the measured cross-section is indicated by a vertical line with the green band showing the statistical uncertainty, the yellow band showing the statistical and systematic uncertainties and the blue band the total uncertainty including the statistical, systematic and luminosity uncertainty

Source of Uncertainty	Detector correction (C)
	0.2605 ± 0.0120
Trigger efficiency	3.7611%
Photon reco. efficiency	1.6853%
Photon PID efficiency	0.7706%
Photon energy scale	0.9820%
Photon energy resolution	0.9823%
Alternative signal MC	0.9835%
Signal MC Statistics	0.8995%
Total	4.6136%

Table 3.5: The correction factor for the detector, C, and its associated uncertainties.

3.6.3 Differential cross sections

Differential fiducial cross sections related to the diphoton invariant mass, diphoton absolute rapidity, and diphoton $|\cos(\theta^*)|$, are unfolded to the particle level within the fiducial phase space outlined in the previous section.

Unfolding

The unfolding process aims to compensate for detector-related effects, including inefficiencies and limited resolution, in the distribution of kinematic variables. The corrected cross section measurements pertain to the fiducial kinematic region, which closely aligns with the phase space defined by the kinematic selection at the detector level [99].

In order to obtain the true value of a measured observable, the observed distribution must be adjusted to account for experimental factors like detector efficiency, resolution, and limited acceptance. These effects are accounted for by using Monte Carlo (MC) simulations, which involve a comprehensive modeling of the particle interactions with the detector material.

The bin-by-bin correction is a commonly used method for data unfolding. It involves determining the ratio of the Monte Carlo (MC) particle-level (true) distribution to the MC reconstructed distribution and applying this ratio bin-by-bin to correct the measured observable. However, this technique may not be suitable when there are significant migrations between bins, as it does not adequately account for such cases. Therefore, the validity of the bin-by-bin correction method relies on the assumption that bin migrations are small.

Let's denote the expected number of events in bin i of the truth-level distribution of our variable X as T_i. Similarly, the number of events in bin i of the reconstructed-level distribution is labeled R_i. Using these quantities, we can calculate correction factors for each bin i using the following equation:

$$C_i = \frac{R_i}{T_i} \tag{3.3}$$

If we now consider a measured distribution D, where D_i represents the number of entries in bin i, we can obtain the unfolded spectrum U by applying the correction factors from Equation 3.3 as follows:

$$U_i = \frac{D_i}{C_i} \tag{3.4}$$

Binning determination for distributions

The bin edges are optimized to strike a balance between having an adequate number of bins to capture the features of the distribution shapes and minimizing significant migrations between bins.

In order to determine the binning of the different distributions, several factors were taken into account. However, due to the small number of events in the data, there was a limitation on the number of bins that could be used.

variable	bin edges
absolute diphoton rapidity	$0, 0.6, 1.2, 1.8, 2.4$
invariant mass $m_{\gamma\gamma}$	0, 5, 10, 15, 20, 30 GeV
$\lvert\cos\theta^*\rvert$	$0, 0.25, 0.5, 0.75, 1$

Table 3.6: Binnings used for the unfolding

Derivation of Uncertainties

The following sources of systematic uncertainty were accounted for during the unfolding procedure:

- Photon Reconstruction Efficiency: Uncertainty arising from the photon reconstruction process.
- Photon PID Efficiency: Uncertainty arising from the photon particle identification process.
- Energy Resolution Efficiency: Uncertainty associated with the photon energy resolution from the EGamma CP Tool.
- Energy Scale Efficiency: Uncertainty associated with the photon energy scale from the EGamma CP Tool.
- Trigger Efficiency: Uncertainty related to the trigger efficiency.

The systematic uncertainties were incorporated into the unfolding procedure by computing the correction factors for each bin i. This process was performed separately for each systematic variation. The results were then combined quadratically to determine the total systematic uncertainty for each bin i.

Tables 3.7, 3.8 and 3.9 show the relative systematic uncertainties for the unfolding of the following kinematic distributions: diphoton $|\cos\theta^*|$, rapidity $y_{\gamma\gamma}$ and $m_{\gamma\gamma}$.

Bin	0 - 0.25	0.25 - 0.5	0.5 - 0.75	0.75 - 1
$d\sigma/dx$	200.875	120.153	81.903	81.764
Stat. (Data)	0.2217	0.2789	0.3308	0.3386
Photon reco.	0.0595	0.0252	0.0317	0.0143
Photon PID	0.0146	0.0008	0.0093	0.0391
Res. down	0.0031	0.0006	0.0016	0.0037
Res. up	0.0189	0.0064	0.0113	0.0235
Scale down	0.0217	0.0029	0.0058	0.0169
Scale up	0.0158	0.0026	0.0054	0.0100
Trig. down	0.0316	0.0135	0.0223	0.0314
Trig. up	0.0397	0.0186	0.0271	0.0390

Table 3.7: Relative systematic uncertainties associated with the unfolding of the diphoton $|\cos\theta^*|$ are presented. In cases where the systematic variations result in symmetrical uncertainties, the combined values are shown.

Bin	0 - 0.6	0.6 - 1.2	1.2 - 1.8	1.8 - 2.4
dσ/dx	74.226	81.146	22.697	19.574
Stat. (Data)	0.1996	0.2071	0.6566	0.6005
Photon reco.	0.0383	0.0210	0.0270	0.0589
Photon PID	0.0044	0.0110	0.0204	0.0435
Res. down	0.0019	0.0011	0.0026	0.0140
Res. up	0.0121	0.0150	0.0171	0.0091
Scale down	0.0051	0.0035	0.0137	0.0208
Scale up	0.0055	0.0073	0.0088	0.0202
Trig. down	0.0234	0.0232	0.0244	0.0241
Trig. up	0.0288	0.0272	0.0299	0.0337

Table 3.8: Relative systematic uncertainties associated with the unfolding of the diphoton rapidity $y_{\gamma\gamma}$ are presented. In cases where the systematic variations result in symmetrical uncertainties, the combined values are shown.

Bin [GeV]	5 - 10	10 - 15	15 - 20	20 - 30
dσ/dx	20.435	3.158	1.273	0.426
Stat. (Data)	0.1781	0.3196	0.4295	0.4647
Stat. (MC)	0.0895	0.1715	0.3333	0.4814
Photon reco.	0.0296	0.0064	0.0071	0.0061
Photon PID	0.0107	0.0156	0.0128	0.0162
Res. down	0.0045	0.0049	0.0116	0.0249
Res. up	0.0136	0.0135	0.0284	0.0174
Scale down	0.0041	0.0120	0.0273	0.0167
Scale up	0.0043	0.0094	0.0133	0.0153
Trig. down	0.0221	0.0126	0.0037	0.0014
Trig. up	0.0288	0.0093	0.0027	0.0015

Table 3.9: Relative systematic uncertainties associated with the unfolding of the diphoton invariant mass $m_{\gamma\gamma}$ are presented. In cases where the systematic variations result in symmetrical uncertainties, the combined values are shown.

Results

We compute the differential cross section for each kinematic distribution by applying the correction factors derived from the truth and reconstructed distributions for each bin i. The following formula is employed for our calculations:

$$\frac{d\sigma_{\mathrm{i}}}{dx} = \frac{\frac{N^{i}_{\mathrm{data}} - N^{i}_{\mathrm{bkg}}}{C_{\mathrm{i}} \times \int L \ \mathrm{d}t}}{\text{bin width}} \tag{3.5}$$

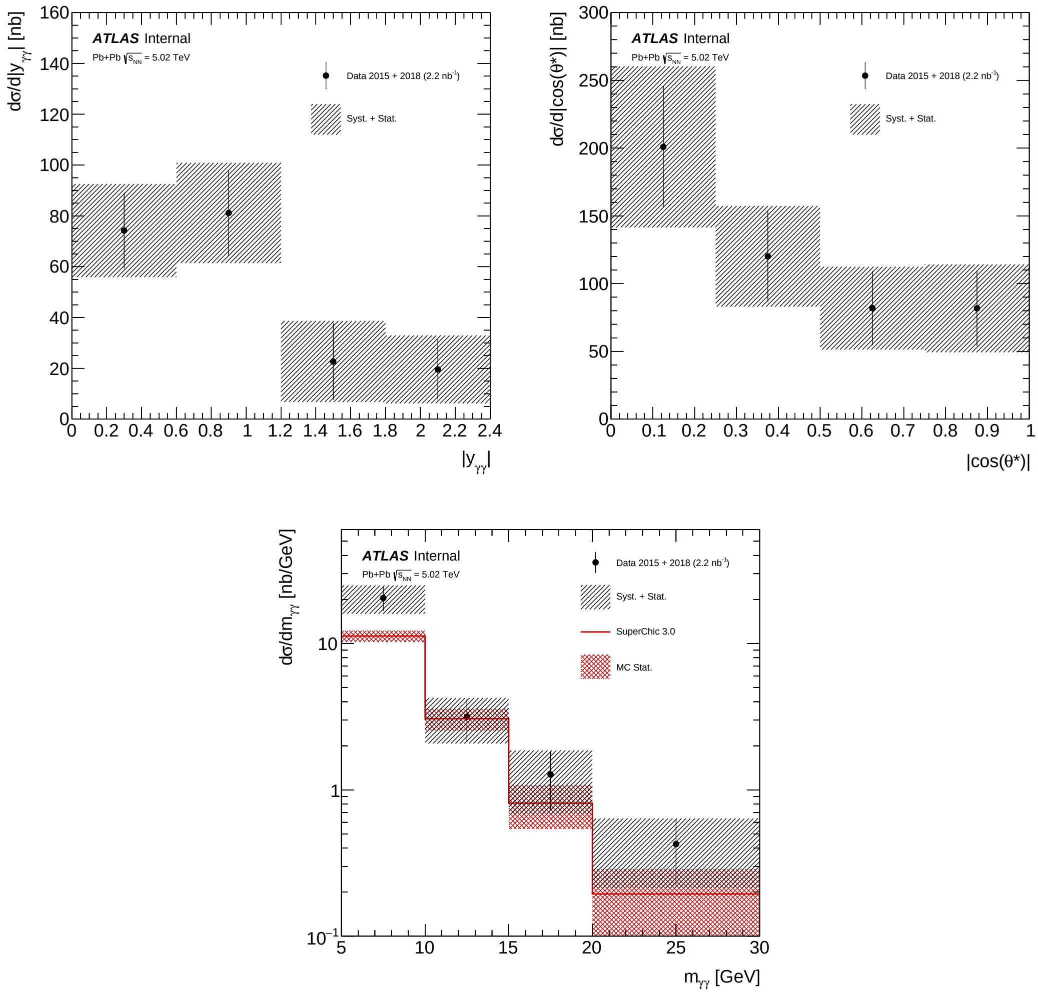

Figure 3.6: Measured differential fiducial cross sections of $\gamma\gamma \to \gamma\gamma$ production in Pb+Pb collisions at $\sqrt{s_{NN}} = 5.02$ TeV for three observables (from left to right and top to bottom): diphoton absolute rapidity, diphoton $|\cos(\theta^*)|$ and diphoton invariant mass. The measured cross-section values are shown as points with error bars giving the statistical uncertainty and grey bands indicating the size of the total uncertainty. The results are compared with the prediction from the SuperChic v3.0 MC generator (solid line) with bands denoting the uncertainty.

In this section, we present the results obtained from the unfolding process. Figure 3.6 compares the differential cross-sections with predictions from SuperChic v3.0. However, it should be noted that we have access to the truth distributions only for the diphoton invariant mass, while for the other kinematic variables, we only have the reconstructed distributions. To calculate the relative uncertainties for those kinematic distributions, we relied on the values of the differential cross-sections $\frac{d\sigma_i}{dx}$ from the most recent study [96].

Analyzing the differential cross-section for the diphoton invariant mass, we observe that, apart from overall normalization differences, the predictions provide a good description of the data. Additionally, we note that the statistical uncertainties are the most dominant in these measurements.

3.6.4 Fitting and Significance

Calculating the significance of a process is a common method to assess the level of evidence or discovery in particle physics experiments. The significance quantifies the level of agreement or deviation between the observed data and the expected background, allowing researchers to determine the compatibility of their models with the theoretical predictions.

In our specific case, where the process of interest is $\gamma\gamma \rightarrow \gamma\gamma$, the significance calculation can provide insights into whether the observed data supports the hypothesis and whether the model is consistent with the theory.

Using a profile likelihood function to fit the data and Monte Carlo (MC) samples is a common approach in statistical analyses. This method allows for parameter estimation and determination of the likelihood of observing the data under different scenarios, such as signal-plus-background or background-only hypotheses. By comparing the likelihoods, researchers can derive the significance of their findings.

Profile Likelihood function

The likelihood function [100] is constructed by combining multiple Poissonian probability terms, each representing a counting experiment in a specific bin of a distribution:

$$\mathcal{L}_{\text{phys}}(\mathrm{N} \mid \mu) = \mathcal{L}_{\text{phys}}(\mu) = \prod_{i \in \text{bins}} \mathcal{P}\left(N_i \mid \mu s_i + b_i\right) \tag{3.6}$$

where N_i is the number of observed data events in bin i, and s_i and b_i are the expected signal and background counts, respectively. The likelihood is introduced here with only one signal strength parameter μ.

The systematic uncertainties are incorporated into the likelihood function through a set of nuisance parameters (NPs), denoted as θ, which modify the expected signal and background yields. This means that the values of the signal and background in each bin are represented as $s_i,\ b_i \rightarrow s_i(\theta),\ b_i(\theta)$. The central value and uncertainty of each NP θ are typically determined in advance through auxiliary measurements. Consequently,

$$\mathcal{L}_{\text{aux}}\left(\vec{\theta}\right) = \prod_{j \in \text{NP}} \mathcal{G}\left(\theta_j^0 \mid \theta_j, \Delta\theta_j\right) \tag{3.7}$$

Based on first principles, the penalty terms should ideally follow Poissonian distributions. However, in the analysis being presented, it is observed that the fit result remains unchanged when Gaussian penalty terms are used instead. This choice helps to expedite the convergence of the fit to a minimum. The complete likelihood can be represented schematically as follows:

$$\mathcal{L}(\underbrace{N, \theta^0}_{\text{Observable}} ; \underbrace{\mu, \theta}_{parameters}) = \prod_{i \in \text{bins}} \mathcal{P}\left(N_i \mid \mu, \theta\right) \times \prod_{j \in NP} \mathcal{G}\left(\theta_j^0 \mid \theta_j, \Delta\theta_j\right) \tag{3.8}$$

The signal estimate is obtained by minimizing the negative logarithm of the likelihood function, denoted as $-\ln \mathcal{L}$, with respect to all parameters (μ, θ). However, analytical solutions are not feasible in this case, so a gradient-descent-based method is employed. This method is implemented using the MINUIT package [101].

The likelihood is also utilized to evaluate the background-only hypothesis ($\mu = 0$). A profile likelihood ratio, denoted as $\lambda(\mu)$, is defined analogous to the Neyman-Pearson ratio. It is given by:

$$\lambda(\mu) = \frac{\mathcal{L}(\mu, \hat{\hat{\theta}})}{\mathcal{L}(\hat{\mu}, \hat{\theta})} \tag{3.9}$$

The values that maximize the likelihood overall, denoted as $\mu, \hat{\hat{\theta}}$, and the ones that maximize L for a chosen value of μ, represented as $\hat{\mu}, \hat{\theta}$, are utilized in the following analysis. In this particular case, the chosen value of μ is θ. Based on this ratio, the discovery test statistic q_0 is constructed as:

$$q_0 = \begin{cases} -2\ln(\lambda(0)) & \hat{\mu} \geq 0 \\ 2\ln(\lambda(0)) & \hat{\mu} < 0 \end{cases} \tag{3.10}$$

Under the assumption of the null hypothesis, the p-value quantifies the probability of observing data that is less compatible with the null hypothesis compared to the measured data. It is determined as:

$$p_0 = \int_{q_{0,\mathrm{obs.}}}^{\infty} f\left(q_0 \mid \mu = 0\right) dq_0 \tag{3.11}$$

Here, $f\left(q_0 \mid \mu = 0\right)$ represents the probability density function (PDF) of the test statistic assuming the hypothesis μ = 0 is true. This PDF is not known a priori and can be estimated using Monte Carlo (MC) simulations. In the case of large sample sizes, it tends to approximate a χ^2 distribution with one degree of freedom.

In the subsequent analysis, the p-value is expressed in terms of Gaussian standard deviations Z, calculated as:

$$Z = \Phi^{-1}\left(1 - p_0\right) = \sqrt{q_0} \tag{3.12}$$

Here, Φ^{-1} refers to the inverse Gaussian cumulative distribution function (CDF).

In the field of particle physics, a significance level of Z = 5, corresponding to a p-value of 2.87×10^{-7}, has been commonly accepted as the threshold to establish a discovery when rejecting the background hypothesis. This signifies a high level of confidence. On the other hand, when it comes to excluding a signal hypothesis, a threshold p-value of 0.05 (equivalent to a 95% confidence level) is often used, corresponding to Z = 1.64.

It is important to note that in a scientific context, rejecting the background-only hypothesis statistically is just one aspect of discovering a new phenomenon. The level of confidence in the presence of a new process depends on other factors, such as the plausibility of the signal hypothesis and its ability to explain the observed data. In this analysis, our focus is solely on determining the p-value of the background-only hypothesis, and if it falls below a specified threshold, it is considered a "discovery."

Parameter of Interest

In the binned maximum likelihood fit, the parameter of interest is the signal strength denoted by μ, which represents the ratio between the measured cross section and the predicted cross section in the Standard Model.

$$\mu = \frac{\sigma^{fid}}{\sigma^{pred}} = \frac{N_{\text{data}} - N_{\text{bkg}}}{N_{\text{sig}}} \tag{3.13}$$

Thence:

$$N_{\text{data}} = \mu \times N_{\text{sig}} + N_{\text{bkg}} \tag{3.14}$$

TRExFitter setup

The TRExFitter software package [102], which includes the Histfactory tools, is utilized for the fitting process. This software allows for the simultaneous fitting of signal and control regions. It offers various functionalities, such as histogram smoothing, pruning, and symmetrization of systematic uncertainties. In the fitting process, TRExFitter combines all the provided histograms and performs a profile likelihood fit.

The likelihood function is constructed by taking the product of Poisson probability terms for each bin. The signal prediction is scaled by the parameter μ, which is extracted from the fit. Systematic uncertainties are incorporated into the likelihood function through the use of nuisance parameters θ. The value $\theta = 0$ represents the nominal MC prediction, while $\theta = \pm 1$ corresponds to the $\pm 1\sigma$ variation.

Results

Performing a profile likelihood fit helped produce many plots for our study. In this section, we present the results of the fit.

- Pre-fit plot & Pruning:

Figure 3.7 displays the pre-fit distribution of the diphoton invariant mass ($m_{\gamma\gamma}$) in the signal region, using the specified binning. This distribution is directly used as input for the fit. It is evident from the figure that there is a good agreement between the total prediction and the observed data in the signal region. The overall discrepancy is primarily attributed to the normalization rather than the shape. All systematic uncertainties are kept after the pruning process (refer to Figure 3.8) are considered and accounted for in the uncertainty bands shown in the figure.

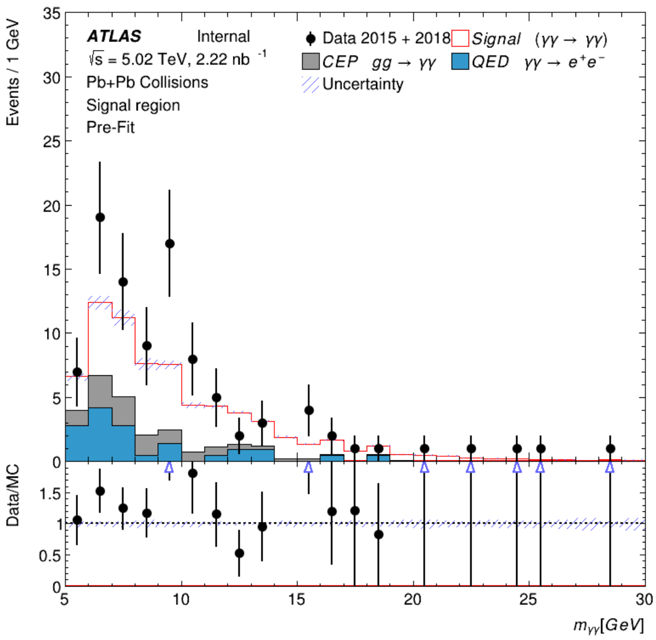

Figure 3.7: Pre-fit distributions of the diphoton invariant mass $m_{\gamma\gamma}$ for the fit in our signal region. The systematic uncertainty is shown.

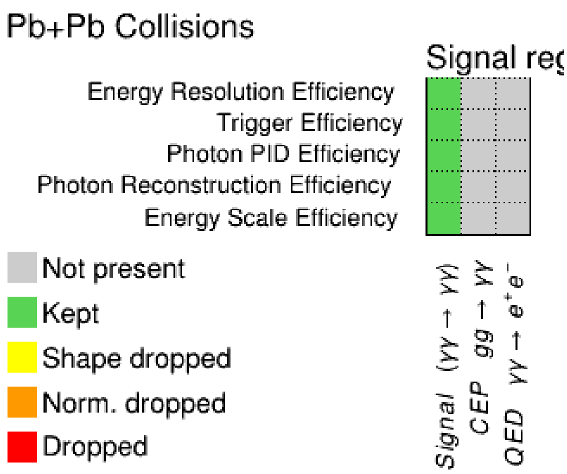

Figure 3.8: Pruning for the systematic uncertainties before applying the fit.

- Nuissance parameters:

A data and signal-plus-background model fit is performed. The pulls and constraints of the NPs are shown in Fig. 3.9. The pulls of the nuisance parameters are within 1σ (0.2σ at most). Since the data include the signal, these pulls are consistent with the expectation.

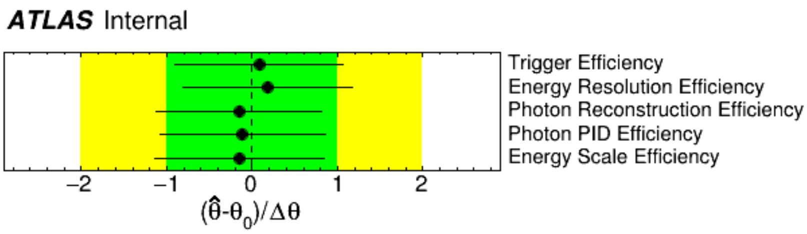

Figure 3.9: Pulls and constraints on the fitted nuisance parameters considered in the fit under the signal-plus-background hypothesis. For each NP, the fitted value represents the preferred shift with respect to the prediction in a unit of its prior uncertainty, and the fitted error represents the uncertainty after the fit in a unit of its prior uncertainty

Figure 3.10 shows the correlation matrix among the nuisance parameters in the fit and the signal strength. The nuisance parameters are almost uncorrelated among each other. The photon reconstruction efficiency and the trigger efficiency have respectively 23.8% and -22.9% correlation (anti-correlation) with the signal strength.

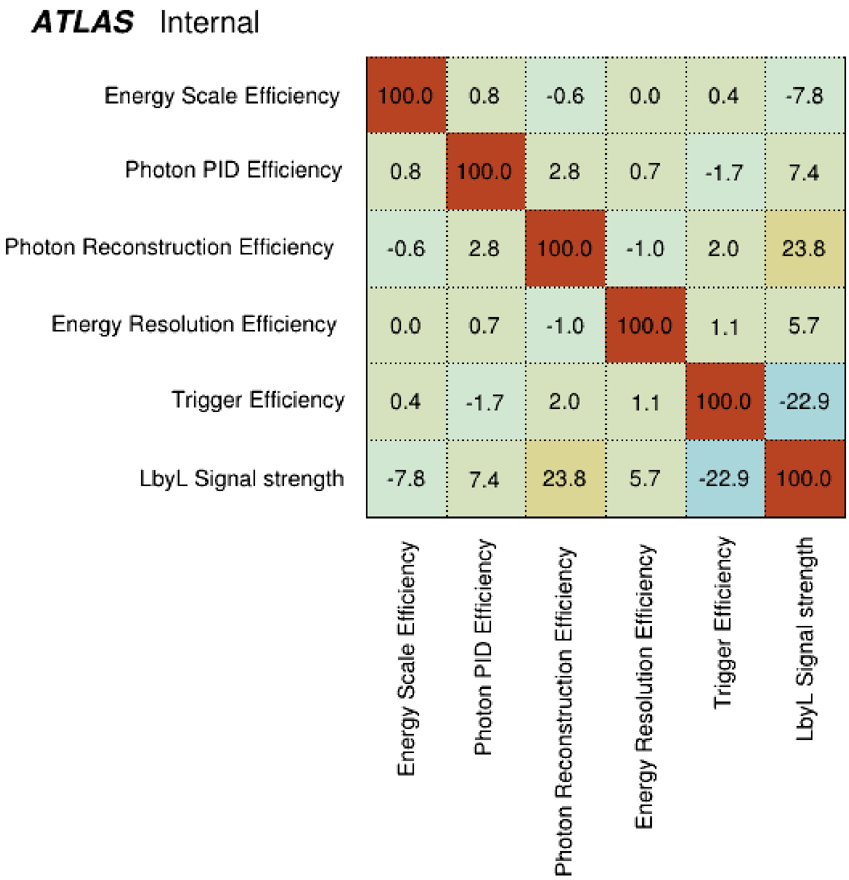

Figure 3.10: Correlation matrix among the nuisance parameters, in the fit to the data, and the signal strength.

To understand the impact of each NP on the signal strength μ, a fit to the Asimov dataset generated under the background-only hypothesis is performed under the signal-plus-background hypothesis and evaluate the impact from the variation of μ when each NP varies by $\pm 1\sigma$ with respect to its prior uncertainty. Figure 3.11 shows the systematic uncertainties and their impact on μ after the fit. The leading uncertainties are those related to photon reconstruction efficiency and the trigger efficiency respectively.

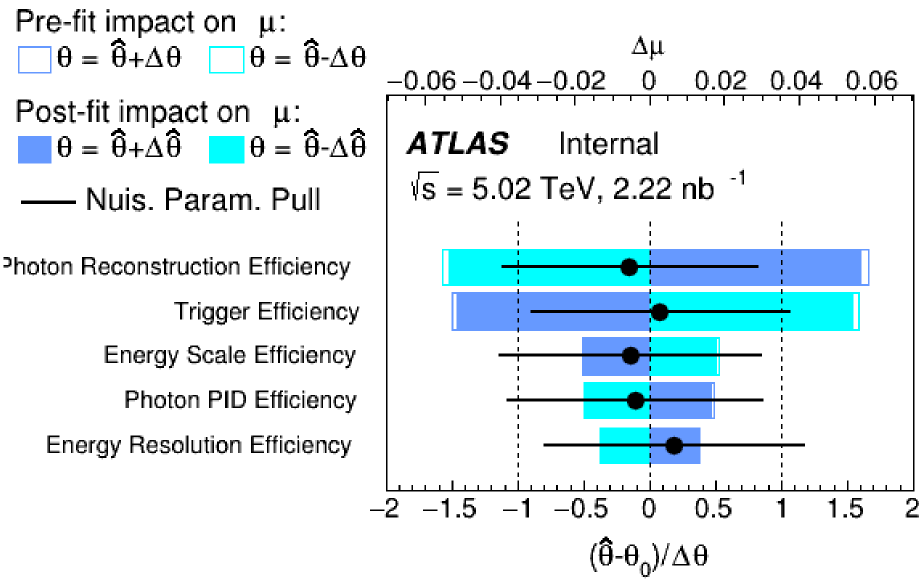

Figure 3.11: Impact on the signal strength μ of each uncertainty obtained from the fit under the signal-plus-background hypothesis to the Asimov dataset generated under the background-only hypothesis. In the figure, there are two independent x-axes in the top and bottom. Black points which are plotted according to the bottom x-axis represent the deviation of each fitted nuisance parameter $(\hat{\theta})$ from the nominal value (θ_0) in a unit of its prior uncertainty $(\Delta\theta)$. The uncertainties are ranked according to their impact on the signal strength μ after the fit (hashed blue area) plotted according to the top x-axis. The impact of each uncertainty on μ is calculated by the difference of μ when a fit is performed with the corresponding nuisance parameter fixed at $\theta_0 \pm \sigma_\theta$.

Plots for systematic variations on the nominal signal are shown in Appendix A

- Signal Strength & Post-fit plot:

Figure 3.12 shows an estimation of our signal strength μ according to the signal-plus-background fit. If the data include the signal, the fitted μ value is estimated to be non-zero value with an uncertainty. As it is our case, the best-fit value of the signal strength μ is estimated to be $1.57^{+0.24}_{-0.22}$.

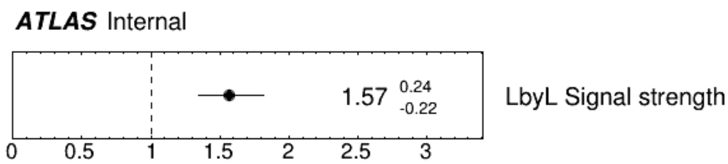

Figure 3.12: Estimation of the Light-by-Light signal strength by the fit.

The distribution of the fitted $m_{\gamma\gamma}$ variable is shown in Figure 3.13. The dashed band represents the post-fit uncertainties. The expected yields after the fit describe the data well.

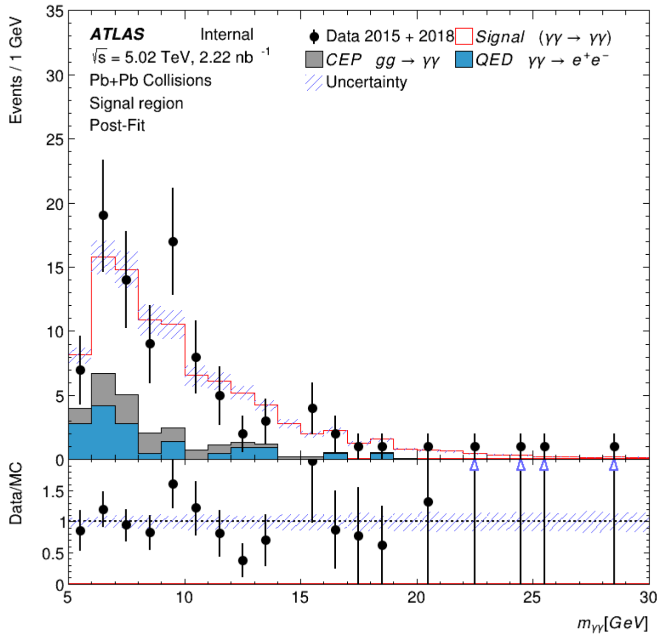

Figure 3.13: Post-fit predicted and observed $m_{\gamma\gamma}$ distributions in the signal region. The uncertainty band represents the post-fit uncertainties.

- Significance:

The assessment of the compatibility between the data and the background-only hypothesis involved the use of a test statistic, denoted as t_μ. This statistic was based on the asymptotic approximation of the profile likelihood ratio [100] and was employed to evaluate the signal strength parameter, μ, which represents the scaling of the signal histogram that yields the best agreement with the data.

The profile likelihood scan of $-2\Delta ln(L)$ is depicted in Figure 3.14, showcasing its variation as a function of μ for both the observed data and the signal and background expectations.

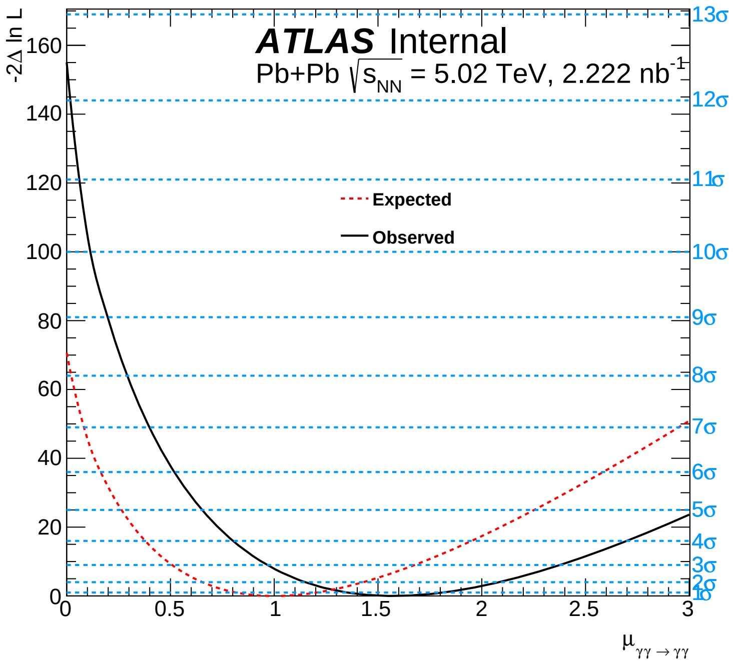

Figure 3.14: The profile likelihood scan as a function of the signal strength μ on the likelihood for the process $\gamma\gamma \to \gamma\gamma$. The observed significance under the background-only hypothesis (μ = 0) stands at 12.45σ, while the anticipated significance is 8.42σ.

The p-value associated with the null hypothesis (background-only) was found to be approximately 0, corresponding to $\mu = 0$ and a significance of 12.45σ. Additionally, the expected significance was determined to be 8.42σ. We can further claim that the Light-by-light scattering is indeed observed in heavy-ion collisions with the ATLAS detector at the LHC.

3.6.5 ALPs search

Light-by-light scattering is an intriguing photon-photon interaction process that serves as a probing ground for new physics beyond the Standard Model (BSM), in our case, precisely Axion-Like-Particles.

In the realm of physics beyond the Standard Model, Axion-Like Particles (ALPs) emerge as prominent contenders for generating diphoton resonances as direct coupling to photons occurs which mean we can track their production in S-channel processes in photon-photon collisions through a resonance peak in the invariant mass spectrum. This spectrum (Figure 3.4), is used to extract limits on the cross section of the process $\gamma\gamma \to a \to \gamma\gamma$, where a represents the ALP. The Light-by-Light signal, QED pair production process $\gamma\gamma \to e^{+}e$ and CEP $gg \to \gamma\gamma$ process are considered as backgrounds.

We employed fully simulated STARLIGHT samples encompassing various ALP masses ranging from 5 to 100 GeV to construct an analytical model of the hypothetical ALP signal within the analysis. In the mass range of $5 < m_a < 30$ GeV, a 1 GeV mass spacing was utilized, while for $m_a > 30$ GeV, a 10 GeV mass spacing was adopted. For each targeted bin, a 'cut and count' experiment was executed to assess the projected number of background events, signal events, and measured data events. This information enabled the fitting of the signal contribution through a profile likelihood fit, employing the TRExFitter package [100, 102]. This process facilitated the estimation of the signal strength limit μ at a 95% confidence level (CL). The bin width was carefully chosen to encompass at least 80% of the anticipated ALP signal events as determined by the signal model in the given mass bin. The bin width ranges from 3 GeV at lower masses to 20 GeV at $m_{\gamma\gamma}$ = 100 GeV.

Systematic uncertainties impacting the ALP signal model's accuracy stem from sources such as trigger, PID, photon reconstruction efficiencies, and photon energy scale and resolution. These uncertainties are assessed following the same methodology as applied in the integrated cross-section measurement, elucidated in Subsection 3.6.2. Theoretical uncertainty associated with the calculated ALP signal cross section amounts to 10% across the entire mass range, due to the limited precision of initial photon fluxes [92]. This uncertainty is treated as uncorrelated with other sources of uncertainties. The luminosity uncertainty associated with the recorded data set is 3.2% [103].

ALPs Limits: Results

The obtained limits on the signal strength μ are converted into limits on the MC cross section, denoted as $\sigma(\gamma\gamma \to a \to \gamma\gamma) = \mu_{CLs}\sigma_{gen}^{MC}$. Furthermore, limits on the photon ALP coupling ($\frac{1}{\Lambda_a^{CLs}}$) are computed according to the formula $\frac{1}{\Lambda_a^{CLs}} = \sqrt{\mu_{CLs}}\frac{1}{\Lambda_a^{gen}}$. σ_{gen}^{MC} represents the cross section and Λ_a^{gen} the coupling employed in the MC generator, and all MC samples are produced using a fixed Λ_a^{gen} value of 1 TeV.

The observed and expected 95% upper limits on the ALP production cross section and the ALP coupling to photons are illustrated in Figure 3.15. Notably, the most significant deviation from the background-only assumption, amounting to a local excess of 2.3 standard deviations, is identified near a mass of 9 GeV.

The established limits on the cross section $\sigma(\gamma\gamma \to a \to \gamma\gamma)$ for an ALP mass spanning 6–100 GeV vary from 200 nb to 2 nb. The deduced bounds on $\frac{1}{\Lambda_a^{CLs}}$ span from 1 TeV^{-1} to 0.06 TeV^{-1}. This analysis's exclusion limits represent the most robust findings within the mass range of $6 < m_a < 100$ GeV.

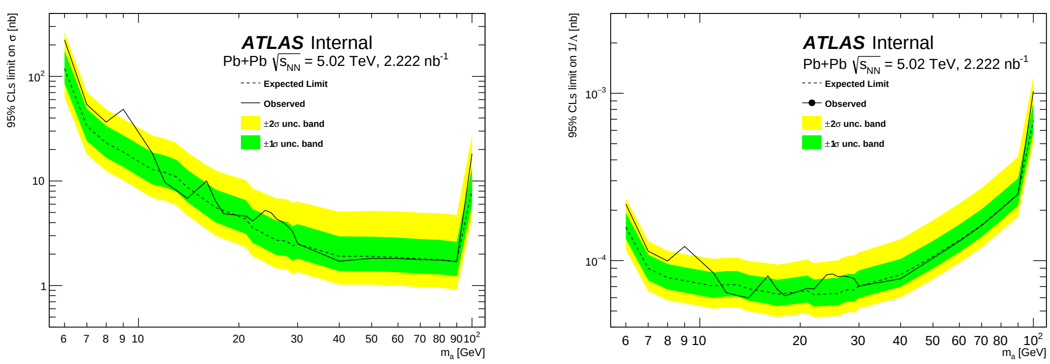

Figure 3.15: The upper limit at a 95% confidence level (CL) on the ALP cross section $\sigma(\gamma\gamma \to a \to \gamma\gamma)$ (left) and the ALP coupling $\frac{1}{\Lambda_a^{CLs}}$ (right) for the $\gamma\gamma \to a \to \gamma\gamma$ process is depicted as a function of the ALP mass m_a. The observed upper limit is illustrated with a solid black line, while the expected upper limit is indicated by a dashed black line accompanied by its ±1 and ±2 standard deviation uncertainty bands.

3.7 Conclusion

To conclude, we have provided a general overview of the analysis of a high-energy physics process, specifically the light-by-light scattering within the ATLAS experiment. We have covered various stages, including the cutflow and selection process, assessment of systematic uncertainties, and obtaining important distributions. These distributions have allowed us to calculate cross sections, both fiducial and integrated. In order to extract meaningful results from the data, we have employed statistical techniques such as Unfolding and Profile Likelihood Fitting. The software TRExFitter played a crucial role in performing a profile likelihood fit to the data, enabling us to conduct a detailed analysis on the Light-by-Light scattering process. It was also useful to search for axion-like particles (ALP) as it was used to set limits on the cross section for their production.

Conclusion

This memorandum was conducted within the ATLAS collaboration and focuses on light-by-light scattering, a quantum-mechanical process initially established theoretically in the early stages of QED by Euler and Heisenberg. The analysis was performed in the context of ultra-peripheral heavy-ion collisions (UPC) using data sets recorded with the ATLAS detector in 2015 and 2018, at a center-of-mass energy of $\sqrt{s_{NN}} = 5.02$ TeV. The analysis involved the observation of the process, measurement of its fiducial and differential cross sections, and interpretation in the context of Axion-Like Particles (ALPs) production.

The first chapter described the theoretical context that sets up the study for our particle physics process, starting from the most fundamental model, the Standard Model of particle physics, and moving to specific aspects of our process, such as heavy ions physics, ultra-peripheral collisions, and evidence of light-by-light scattering.

The second chapter provided a detailed account of the experimental setup used for the study, from the LHC acceleration chain at CERN to various compartments and detectors within the ATLAS experiment, where our process was observed.

In the third and final chapter, we presented the results of our data analysis. First, we explained the analysis process, the sources of our data and Monte Carlo (MC) samples, the selections applied, and the obtained cut flow. Then, we presented plots for kinematic distributions of γ variables using data and MC samples. These plots show that the analysis combined the 2015 and 2018 data sets, resulting in 97 observed events, with an expected 45 ± 4 signal events and 27 ± 5 background events.

Next, we calculated the fiducial cross-section by first determining the correction factor and various uncertainties. The measured fiducial cross-section was 121.53 ± 17.03 (stat.) $\pm$ 9.51 (syst.) $\pm$ 3.83 (lumi.) nb, with a calculated value for the correction factor of C = 0.2605 ± 0.0120.

We then conducted a more in-depth study of our process by calculating the differential cross-sections using a statistical approach called bin-by-bin unfolding. The differential cross-sections were measured as a function of various variables related to the final-state photons and compared with theoretical predictions.

Finally, we applied a profile likelihood fit to compare the likelihood of observing our data under different hypotheses: a null hypothesis for background-only and a signal-plus-background hypothesis. This provided us with valuable information on our parameter of interest, the light-by-light signal strength, and the various nuisance parameters, which we used to evaluate the significance of our process. The statistical significance against the background-only hypothesis was found to be 12.45 standard deviations, indicating that we indeed observed light-by-light scattering at the LHC using the ATLAS detector. The diphoton invariant mass distribution was analyzed to search for axion-like particles and establish new exclusion limits on their production. Currently, the derived exclusion limits are the most stringent within the mass range of $6 < m_a < 100$ GeV.

The 2018 heavy-ion data taking marked the final stage of LHC Run 2. Following that, the LHC underwent a long shutdown phase during which all detectors, as well as the LHC itself, were upgraded in preparation for Run 3. Run 3 started in 2021, ushering in the HL-LHC era with an expected luminosity twice as high as Run 2.

While the LHC data has provided numerous answers and precise measurements of Standard Model processes, such as light-by-light scattering, it also raises questions regarding physics beyond the standard model, such as dark matter and supersymmetry. With the anticipation of new data from Run 3 and the HL-LHC, we hope to further illuminate these unknown aspects of our universe.

Looking ahead and with the availability of new data, it would be worthwhile to rerun the analysis using the data from Run 3. These new measurements can be leveraged to interpret other predictions of Beyond the Standard Model (BSM) theories, such as Magnetic Monopoles or any other BSM extensions.

Bibliography

[1] F. Carmona, J.R. Lalanne, and L. Servant. *Optical Spectroscopies Of Electronic Absorption*. World Scientific Series In Contemporary Chemical Physics. World Scientific Publishing Company, 1999. isbn: 9789813105485. url: https://books.google.co.ma/books?id=Fo9IDQAAQBAJ.

[2] W. Heisenberg and H. Euler. *Consequences of Dirac Theory of the Positron*. 2006. arXiv: physics/0605038 [physics.hist-ph].

[3] Robert R. Wilson. "Scattering of 1.3^3 Mev Gamma-Rays by an Electric Field". In: *Phys. Rev.* 90 (4 May 1953), pp. 720–721. doi: 10.1103/PhysRev.90.720. url: https://link.aps.org/doi/10.1103/PhysRev.90.720.

[4] G. Jarlskog et al. "Measurement of Delbrück Scattering and Observation of Photon Splitting at High Energies". In: *Phys. Rev. D* 8 (11 Dec. 1973), pp. 3813–3823. doi: 10.1103/PhysRevD.8.3813. url: https://link.aps.org/doi/10.1103/PhysRevD.8.3813.

[5] M. Schumacher et al. "Delbrück scattering of 2.75 MeV photons by lead". In: *Physics Letters B* 59.2 (1975), pp. 134–136. issn: 0370-2693. doi: https://doi.org/10.1016/0370-2693(75)90685-1. url: https://www.sciencedirect.com/science/article/pii/0370269375906851.

[6] Sh. Zh. Akhmadaliev et al. "Delbrück scattering at energies of 140–450 MeV". In: *Phys. Rev. C* 58 (5 Nov. 1998), pp. 2844–2850. doi: 10.1103/PhysRevC.58.2844. url: https://link.aps.org/doi/10.1103/PhysRevC.58.2844.

[7] Sh. Zh. Akhmadaliev et al. "Experimental Investigation of High-Energy Photon Splitting in Atomic Fields". In: *Phys. Rev. Lett.* 89 (6 July 2002), p. 061802. doi: 10.1103/PhysRevLett.89.061802. url: https://link.aps.org/doi/10.1103/PhysRevLett.89.061802.

[8] . "SEARCH FOR AXION-LIKE PARTICLES USING STRONG PULSED MAGNETS AT SPRING-8". PhD thesis. University of Tokyo(), 2016. doi: 10.15083/00073282. url: https://cir.nii.ac.jp/crid/1110845735138598400.

[9] Xing Fan et al. "The OVAL experiment: a new experiment to measure vacuum magnetic birefringence using high repetition pulsed magnets". In: *The European Physical Journal D* 71.11 (Nov. 2017). doi: 10.1140/epjd/e2017-80290-7. url: https://doi.org/10.1140/epjd/e2017-80290-7.

[10] Julian Schwinger. "On Gauge Invariance and Vacuum Polarization". In: *Phys. Rev.* 82 (5 June 1951), pp. 664–679. doi: 10.1103/PhysRev.82.664. url: https://link.aps.org/doi/10.1103/PhysRev.82.664.

[11] "Evidence for light-by-light scattering in heavy-ion collisions with the ATLAS detector at the LHC". In: *Nature Physics* 13.9 (Aug. 2017), pp. 852–858. doi: 10.1038/nphys4208. url: https://doi.org/10.1038/Fnphys4208.

[12] Enrico Fermi. "On the Theory of Collisions between Atoms and Electrically Charged Particles". In: *Electromagnetic Probes of Fundamental Physics*. WORLD SCIENTIFIC, Sept. 2003. doi: 10.1142/9789812704214_0026. url: https://doi.org/10.1142/9789812704214_0026.

[13] C. F. von Weizsacker. “Radiation emitted in collisions of very fast electrons”. In: *Z. Phys.* 88 (1934), pp. 612–625. doi: 10.1007/BF01333110.

[14] E. J. Williams. “Nature of the High Energy Particles of Penetrating Radiation and Status of Ionization and Radiation Formulae”. In: *Phys. Rev.* 45 (10 May 1934), pp. 729–730. doi: 10.1103/PhysRev.45.729. url: https://link.aps.org/doi/10.1103/PhysRev.45.729.

[15] A.J. Baltz et al. “The physics of ultraperipheral collisions at the LHC”. In: *Physics Reports* 458.1 (2008), pp. 1–171. issn: 0370-1573. doi: https://doi.org/10.1016/j.physrep.2007.12.001. url: https://www.sciencedirect.com/science/article/pii/S0370157307004462.

[16] Spencer R. Klein and Peter Steinberg. “Photonuclear and Two-Photon Interactions at High-Energy Nuclear Colliders”. In: *Annual Review of Nuclear and Particle Science* 70.1 (2020), pp. 323–354. doi: 10.1146/annurev-nucl-030320-033923. eprint: https://doi.org/10.1146/annurev-nucl-030320-033923. url: https://doi.org/10.1146/annurev-nucl-030320-033923.

[17] *Measurement of light-by-light scattering in ultraperipheral PbPb collisions at $\sqrt{s_{\mathrm{NN}}}$ = 5.02 TeV*. Tech. rep. Geneva: CERN, 2018. url: https://cds.cern.ch/record/2319158.

[18] ALICE Collaboration. “Measurement of the cross section for electromagnetic dissociation with neutron emission in Pb-Pb collisions at sNN =2.76 TeV”. In: *Physical Review Letters* 109.25 (Dec. 2012). doi: 10.1103/physrevlett.109.252302. url: https://doi.org/10.1103/physrevlett.109.252302.

[19] The CMS Collaboration. “Evidence for light-by-light scattering and searches for axion-like particles in ultraperipheral PbPb collisions at sNN=5.02TeV”. In: *Physics Letters B* 797 (2019), p. 134826. issn: 0370-2693. doi: https://doi.org/10.1016/j.physletb.2019.134826. url: https://www.sciencedirect.com/science/article/pii/S0370269319305404.

[20] The ATLAS Collaboration. “Observation of Light-by-Light Scattering in Ultraperipheral Pb + Pb Collisions with the ATLAS Detector”. In: *Phys. Rev. Lett.* 123 (5 July 2019), p. 052001. doi: 10.1103/PhysRevLett.123.052001. url: https://link.aps.org/doi/10.1103/PhysRevLett.123.052001.

[21] David d’Enterria and Gustavo G. da Silveira. “Observing Light-by-Light Scattering at the Large Hadron Collider”. In: *Phys. Rev. Lett.* 111 (8 Aug. 2013), p. 080405. doi: 10.1103/PhysRevLett.111.080405. url: https://link.aps.org/doi/10.1103/PhysRevLett.111.080405.

[22] Sheldon L. Glashow. “Partial-symmetries of weak interactions”. In: *Nuclear Physics* 22.4 (1961), pp. 579–588. issn: 0029-5582. doi: https://doi.org/10.1016/0029-5582(61)90469-2. url: https://www.sciencedirect.com/science/article/pii/0029558261904692.

[23] Steven Weinberg. “Stephen Weinberg”. In: *Quantum Algebra and Symmetry* (2010), p. 665.

[24] Salam Abdus. “Weak and electromagnetic interactions, conf”. In: *Proc. C* 680519 (1968), pp. 367–377.

[25] Z. Physik. “On the Connexion between the Completion of Electron Groups in an Atom with the Complex Structure of Spectra”. In: 2010.

[26] Krzysztof A. Meissner and Hermann Nicolai. “Standard Model Fermions and Infinite-Dimensional *R* Symmetries”. In: *Phys. Rev. Lett.* 121 (9 Aug. 2018), p. 091601. doi: 10.1103/PhysRevLett.121.091601. url: https://link.aps.org/doi/10.1103/PhysRevLett.121.091601.

[27] David Griffiths. *Introduction to elementary particles*. John Wiley & Sons, 2020.

[28] Particle Data Group et al. "Review of Particle Physics". In: *Progress of Theoretical and Experimental Physics* 2022.8 (Aug. 2022). 083C01. issn: 2050-3911. doi: 10.1093/ptep/ptac097. eprint: https://academic.oup.com/ptep/article-pdf/2022/8/083C01/49175539/ptac097.pdf. url: https://doi.org/10.1093/ptep/ptac097.

[29] Geoffrey T J Arnison et al. "Experimental observation of isolated large transverse energy electrons with associated missing energy at $\sqrt{s} = 540 GeV$". In: *Phys. Lett. B* 122 (1983), pp. 103–116. doi: 10.5170/CERN-1983-004.123. url: https://cds.cern.ch/record/142059.

[30] G. Arnison et al. "Experimental Observation of Lepton Pairs of Invariant Mass Around 95-GeV/c**2 at the CERN SPS Collider". In: *Phys. Lett. B* 126 (1983), pp. 398–410. doi: 10.1016/0370-2693(83)90188-0.

[31] The ATLAS Collaboration. "Observation of a new particle in the search for the Standard Model Higgs boson with the ATLAS detector at the LHC". In: *Physics Letters B* 716.1 (Sept. 2012), pp. 1–29. doi: 10.1016/j.physletb.2012.08.020. url: https://doi.org/10.1016/Fj.physletb.2012.08.020.

[32] J. Clerk Maxwell. "A Dynamical Theory of the Electromagnetic Field". In: *Philosophical Transactions of the Royal Society of London* 155 (1865), pp. 459–512. issn: 02610523. url: http://www.jstor.org/stable/108892 (visited on 06/19/2023).

[33] R.P. Feynman. *Quantum Electrodynamics (1st ed.)*. CRC Press, 1998. doi: 10.1201/9780429493249.

[34] Andrey Grozin. *Quantum Chromodynamics*. 2012. arXiv: 1205.1815 [hep-ph].

[35] Guido Altarelli and James Wells. "QCD: The Theory of Strong Interactions". In: *Collider Physics within the Standard Model: A Primer*. Ed. by James Wells. Cham: Springer International Publishing, 2017, pp. 27–96. isbn: 978-3-319-51920-3. doi: 10.1007/978-3-319-51920-3_2. url: https://doi.org/10.1007/978-3-319-51920-3_2.

[36] Chris Quigg. *The Electroweak Theory*. 2002. arXiv: hep-ph/0204104 [hep-ph].

[37] Sarthak Satapathy et al. "Higgs in Quark Gluon Plasma". In: Jan. 2020.

[38] Matts Roos. *Dark Matter: The evidence from astronomy, astrophysics and cosmology*. 2010. arXiv: 1001.0316 [astro-ph.CO].

[39] Johann Rafelski. "Connecting QGP-heavy ion physics to the early universe". In: *Nuclear Physics B-Proceedings Supplements* 243 (2013), pp. 155–162.

[40] Carlos A. Bertulani, Spencer R. Klein, and Joakim Nystrand. "PHYSICS OF ULTRA-PERIPHERAL NUCLEAR COLLISIONS". In: *Annual Review of Nuclear and Particle Science* 55.1 (Dec. 2005), pp. 271–310. doi: 10.1146/annurev.nucl.55.090704.151526. url: https://doi.org/10.1146/annurev.nucl.55.090704.151526.

[41] Fairouz Malek. *Ultra-Peripheral Collisions physics with ATLAS*. Tech. rep. Geneva: CERN, 2022. url: https://cds.cern.ch/record/2836458.

[42] Kyrre Skjerdal. "Photoproduction of ρ^0 in ultra–peripheral nuclear collisions at ALICE". In: *J. Phys.: Conf. Ser.* 455 (2013). Comments: 8 pages, 8 figures, prepared for the Proceedings of the International Workshop On Physics At The LHC (Kruger 2012) December 3 - 7, 2012 Protea Hotel, Kruger Gate South Africa, p. 012010. doi: 10.1088/1742-6596/455/1/012010. arXiv: 1304.6850. url: https://cds.cern.ch/record/1544220.

[43] Mikhail G. Kozlov. *Next to leading order QED corrections to the process $\gamma\gamma \to \mu^+\mu^-\gamma$*. 2019. arXiv: 1712.07896 [hep-ph].

[44] Hans Euler. "On the scattering of light by light according to Dirac's theory". In: *Annalen Phys.* 26.5 (1936), pp. 398–448. doi: 10.1002/andp.19364180503.

[45] S. I. Vavilov. *Remarks on the empirical accuracy of the optical superposition principle [Engl. transl. of Zh. Russk. Fiz.-Khim. Obshch., Ch. Fiz. 60(1928)555]*. 2017. arXiv: 1708.06817 [physics.hist-ph].

[46] A. L. Hughes and G. E. M. Jauncey. "An Attempt to Detect Collisions of Photons". In: *Phys. Rev.* 36 (4 Aug. 1930), pp. 773–777. doi: 10.1103/PhysRev.36.773. url: https://link.aps.org/doi/10.1103/PhysRev.36.773.

[47] E. Lundström et al. "Using High-Power Lasers for Detection of Elastic Photon-Photon Scattering". In: *Phys. Rev. Lett.* 96 (8 Mar. 2006), p. 083602. doi: 10.1103/PhysRevLett.96.083602. url: https://link.aps.org/doi/10.1103/PhysRevLett.96.083602.

[48] Karnig O. Mikaelian. "Detection of elastic light-by-light scattering at SLAC". In: *Physics Letters B* 115.3 (1982), pp. 267–269. issn: 0370-2693. doi: https://doi.org/10.1016/0370-2693(82)90660-8. url: https://www.sciencedirect.com/science/article/pii/0370269382906608.

[49] H. N. Brown et al. "Precise Measurement of the Positive Muon Anomalous Magnetic Moment". In: *Physical Review Letters* 86.11 (Mar. 2001), pp. 2227–2231. doi: 10.1103/physrevlett.86.2227. url: https://doi.org/10.1103/physrevlett.86.2227.

[50] Robert S. Van Dyck, Paul B. Schwinberg, and Hans G. Dehmelt. "New high-precision comparison of electron and positron g factors". In: *Phys. Rev. Lett.* 59 (1 July 1987), pp. 26–29. doi: 10.1103/PhysRevLett.59.26. url: https://link.aps.org/doi/10.1103/PhysRevLett.59.26.

[51] R. D. Peccei and Helen R. Quinn. "CP Conservation in the Presence of Pseudoparticles". In: *Phys. Rev. Lett.* 38 (25 June 1977), pp. 1440–1443. doi: 10.1103/PhysRevLett.38.1440. url: https://link.aps.org/doi/10.1103/PhysRevLett.38.1440.

[52] Simon Knapen et al. "Searching for Axionlike Particles with Ultraperipheral Heavy-Ion Collisions". In: *Physical Review Letters* 118.17 (Apr. 2017). doi: 10.1103/physrevlett.118.171801. url: https://doi.org/10.1103/physrevlett.118.171801.

[53] The ATLAS collaboration. "Measurement of light-by-light scattering and search for axion-like particles with 2.2 nb^1 of Pb+Pb data with the ATLAS detector". In: *Journal of High Energy Physics* 2021.3 (Mar. 2021), p. 243. issn: 1029-8479. doi: 10.1007/JHEP03(2021)243. url: https://doi.org/10.1007/JHEP03(2021)243.

[54] X. Fan et al. "Measurement of the Electron Magnetic Moment". In: *Phys. Rev. Lett.* 130 (7 Feb. 2023), p. 071801. doi: 10.1103/PhysRevLett.130.071801. url: https://link.aps.org/doi/10.1103/PhysRevLett.130.071801.

[55] Ana Lopes and Melissa Loyse Perrey. "FAQ-LHC The guide". 2022. url: https://cds.cern.ch/record/2809109.

[56] C.E. Gerber. "LHC highlights and prospects". en. In: *CERN Yellow Reports: School Proceedings* Vol. 2 (2021 2021), 13–26 March 2019. doi: 10.23730/CYRSP-2021-002.161. url: https://e-publishing.cern.ch/index.php/CYRSP/article/view/1314.

[57] The ALICE Collaboration. "The ALICE experiment at the CERN LHC". In: *Journal of Instrumentation* 3.08 (Aug. 2008), S08002. doi: 10.1088/1748-0221/3/08/S08002. url: https://dx.doi.org/10.1088/1748-0221/3/08/S08002.

[58] The CMS Collaboration. "The CMS experiment at the CERN LHC". In: *Journal of Instrumentation* 3.08 (Aug. 2008), S08004. doi: 10.1088/1748-0221/3/08/S08004. url: https://dx.doi.org/10.1088/1748-0221/3/08/S08004.

[59] The LHCb Collaboration. "The LHCb Detector at the LHC". In: *Journal of Instrumentation* 3.08 (Aug. 2008), S08005. doi: 10.1088/1748-0221/3/08/S08005. url: https://dx.doi.org/10.1088/1748-0221/3/08/S08005.

[60] Ewa Lopienska. "The CERN accelerator complex, layout in 2022. Complexe des accélérateurs du CERN en janvier 2022". In: (2022). General Photo. url: https://cds.cern.ch/record/2800984.

[61] The ATLAS Collaboration. "The ATLAS Experiment at the CERN Large Hadron Collider". In: *Journal of Instrumentation* 3.08 (Aug. 2008), S08003. doi: 10.1088/1748-0221/3/08/S08003. url: https://dx.doi.org/10.1088/1748-0221/3/08/S08003.

[62] *Glossary*. http://opendata.atlas.cern/books/current/get-started/_book/GLOSSARY.html. Accessed: 2023-06-12.

[63] The ATLAS Collaboration. "The ATLAS Inner Detector commissioning and calibration". In: *The European Physical Journal C* 70 (Dec. 2010), pp. 787–821. doi: 10.1140/epjc/s10052-010-1366-7.

[64] M.S Alam et al. "The ATLAS silicon pixel sensors". In: *Nuclear Instruments and Methods in Physics Research Section A: Accelerators, Spectrometers, Detectors and Associated Equipment* 456.3 (2001), pp. 217–232. issn: 0168-9002. doi: https://doi.org/10.1016/S0168-9002(00)00574-X. url: https://www.sciencedirect.com/science/article/pii/S016890020000574X.

[65] Markus Keil. "Operational Experience with the ATLAS Pixel Detector at the LHC". In: *Physics Procedia* 37 (Dec. 2012), pp. 907–914. doi: 10.1016/j.phpro.2012.02.431.

[66] Georges Blanchot et al. "The Cesium source calibration and monitoring system of the ATLAS Tile Calorimeter: design, construction and results". In: *Journal of Instrumentation* 15 (Mar. 2020), P03017–P03017. doi: 10.1088/1748-0221/15/03/P03017.

[67] *ATLAS liquid-argon calorimeter: Technical Design Report*. Technical design report. ATLAS. Geneva: CERN, 1996. doi: 10.17181/CERN.FWRW.FOOQ. url: https://cds.cern.ch/record/331061.

[68] Carlos Solans Sanchez, Juan Ferrer, and Emilio Higon-Rodriguez. "Implementation of the ROD Crate DAQ Software for the ATLAS Tile Calorimeter and a Search for a MSSM Higgs Boson decaying into Tau pairs". In: (Jan. 2010).

[69] The ATLAS Collaboration. "Readiness of the ATLAS Tile Calorimeter for LHC collisions". In: *European Physical Journal C* (Jan. 2010).

[70] Jessica Metcalfe et al. "Development of Planar and 3D Silicon Sensor Technologies for the ATLAS Experiment Upgrades and Measurements of Heavy Quark Production Fractions with Fully Reconstructed D-star Mesons with ATLAS". In: (June 2023).

[71] *Luminosity Public Results Run 3*. https://twiki.cern.ch/twiki/bin/view/AtlasPublic/LuminosityPublicResultsRun3. Accessed: 2023-06-14.

[72] *Luminosity Public Results Run 2*. https://twiki.cern.ch/twiki/bin/view/AtlasPublic/LuminosityPublicResultsRun2. Accessed: 2023-06-14.

[73] *ATLAS level-1 trigger: Technical Design Report*. Technical design report. ATLAS. Geneva: CERN, 1998. url: http://cds.cern.ch/record/381429.

[74] Peter Jenni et al. *ATLAS high-level trigger, data-acquisition and controls: Technical Design Report*. Technical design report. ATLAS. Geneva: CERN, 2003. url: https://cds.cern.ch/record/616089.

[75] Jose Guillermo Panduro Vazquez. "The ATLAS Data Acquisition System in LHC Run 2". In: *Journal of Physics: Conference Series* 898 (Oct. 2017), p. 032017. doi: 10.1088/1742-6596/898/3/032017.

[76] The ATLAS TDAQ Collaboration. "The ATLAS Data Acquisition and High Level Trigger system". In: *Journal of Instrumentation* 11.06 (June 2016), P06008. doi: 10.1088/1748-0221/11/06/P06008. url: https://dx.doi.org/10.1088/1748-0221/11/06/P06008.

[77] *ATLAS Computing: technical design report*. Technical design report. ATLAS. Geneva: CERN, 2005. url: https://cds.cern.ch/record/837738.

[78] K. Bos et al. *LHC computing Grid: Technical Design Report. Version 1.06 (20 Jun 2005)*. Technical design report. LCG. Geneva: CERN, 2005. url: https://cds.cern.ch/record/840543.

[79] The ATLAS Collaboration. "The ATLAS Simulation Infrastructure". In: *The European Physical Journal C* 70.3 (Sept. 2010), pp. 823–874. doi: 10.1140/epjc/s10052-010-1429-9. url: https://doi.org/10.1140/epjc/s10052-010-1429-9.

[80] S. Agostinelli et al. "Geant4—a simulation toolkit". In: *Nuclear Instruments and Methods in Physics Research Section A: Accelerators, Spectrometers, Detectors and Associated Equipment* 506.3 (2003), pp. 250–303. issn: 0168-9002. doi: https://doi.org/10.1016/S0168-9002(03)01368-8. url: https://www.sciencedirect.com/science/article/pii/S0168900203013688.

[81] Elzbieta Richter-Was, D Froidevaux, and Luc Poggioli. *ATLFAST 2.0 a fast simulation package for ATLAS*. Tech. rep. Geneva: CERN, 1998. url: https://cds.cern.ch/record/683751.

[82] E Barberio et al. "Fast shower simulation in the ATLAS calorimeter". In: *Journal of Physics: Conference Series* 119.3 (July 2008), p. 032008. doi: 10.1088/1742-6596/119/3/032008. url: https://dx.doi.org/10.1088/1742-6596/119/3/032008.

[83] The ATLAS Collaboration. "Electron and photon performance measurements with the ATLAS detector using the 2015–2017 LHC proton-proton collision data". In: *Journal of Instrumentation* 14.12 (Dec. 2019), P12006. doi: 10.1088/1748-0221/14/12/P12006. url: https://dx.doi.org/10.1088/1748-0221/14/12/P12006.

[84] The ATLAS Collaboration. "Electron reconstruction and identification in the ATLAS experiment using the 2015 and 2016 LHC proton–proton collision data at \sqrt{s} = 13 \text {TeV}". In: *The European Physical Journal C* 79.8 (Aug. 2019). doi: 10.1140/epjc/s10052-019-7140-6. url: https://doi.org/10.1140/epjc/s10052-019-7140-6.

[85] Hassane Hamdaoui. "Observation of light-by-light scattering in heavy-ion collisions with the ATLAS detector at the LHC. Observation de la diffusion lumière par lumière dans les collisions d'ions lourds avec le détecteur ATLAS du LHC". Presented 20 Feb 2021. 2021. url: https://cds.cern.ch/record/2752826.

[86] L. A. Harland-Lang, V. A. Khoze, and M. G. Ryskin. "Exclusive LHC physics with heavy ions: SuperChic 3". In: *The European Physical Journal C* 79.1 (Jan. 2019). doi: 10.1140/epjc/s10052-018-6530-5. url: https://doi.org/10.1140/epjc/s10052-018-6530-5.

[87] Zvi Bern et al. "QCD and QED corrections to light-by-light scattering". In: *Journal of High Energy Physics* 2001.11 (Nov. 2001), p. 031. doi: 10.1088/1126-6708/2001/11/031. url: https://doi.org/10.1088/1126-6708/2001/11/031.

[88] Mariola Kłusek-Gawenda, Wolfgang Schäfer, and Antoni Szczurek. "Two-gluon exchange contribution to elastic $\gamma\gamma \to \gamma\gamma$ scattering and production of two-photons

in ultraperipheral ultrarelativistic heavy ion and proton–proton collisions". In: *Physics Letters B* 761 (Oct. 2016), pp. 399–407. doi: 10.1016/j.physletb.2016.08.059. url: https://doi.org/10.1016/j.physletb.2016.08.059.

[89] Mariola Kłusek-Gawenda, Piotr Lebiedowicz, and Antoni Szczurek. "Light-by-light scattering in ultraperipheral Pb-Pb collisions at energies available at the CERN Large Hadron Collider". In: *Physical Review C* 93.4 (Apr. 2016). doi: 10.1103/physrevc.93.044907. url: https://doi.org/10.1103/physrevc.93.044907.

[90] Spencer R. Klein and Joakim Nystrand. "Photoproduction of Quarkonium in Proton-Proton and Nucleus-Nucleus Collisions". In: *Physical Review Letters* 92.14 (Apr. 2004). doi: 10.1103/physrevlett.92.142003. url: https://doi.org/10.1103/physrevlett.92.142003.

[91] Spencer R. Klein et al. "STARlight: A Monte Carlo simulation program for ultra-peripheral collisions of relativistic ions". In: *Computer Physics Communications* 212 (Mar. 2017), pp. 258–268. doi: 10.1016/j.cpc.2016.10.016. url: https://doi.org/10.1016/j.cpc.2016.10.016.

[92] C. Azevedo, V. P. Gonçalves, and B. D. Moreira. "Exclusive dilepton production in ultraperipheral PbPb collisions at the LHC". In: *The European Physical Journal C* 79.5 (May 2019). doi: 10.1140/epjc/s10052-019-6952-8. url: https://doi.org/10.1140/Fepjc/s10052-019-6952-8.

[93] L. Frankfurt et al. "Generalized parton distributions and rapidity gap survival in exclusive diffractive *pp* scattering". In: *Phys. Rev. D* 75 (5 Mar. 2007), p. 054009. doi: 10.1103/PhysRevD.75.054009. url: https://link.aps.org/doi/10.1103/PhysRevD.75.054009.

[94] Manuel Bähr et al. "Herwig++ physics and manual". In: *The European Physical Journal C* 58.4 (Nov. 2008), pp. 639–707. doi: 10.1140/epjc/s10052-008-0798-9. url: https://doi.org/10.1140/epjc/s10052-008-0798-9.

[95] Torbjörn Sjöstrand et al. "An introduction to PYTHIA 8.2". In: *Computer Physics Communications* 191 (June 2015), pp. 159–177. doi: 10.1016/j.cpc.2015.01.024. url: https://doi.org/10.1016/j.cpc.2015.01.024.

[96] Iwona Grabowska-Bold et al. *Measurement of light-by-light scattering with 2.2 nb^1 of Pb+Pb data in the ATLAS detector – Supporting Note*. Tech. rep. Geneva: CERN, 2019. url: https://cds.cern.ch/record/2703499.

[97] The ATLAS Collaboration. "Measurement of the photon identification efficiencies with the ATLAS detector using LHC Run 2 data collected in 2015 and 2016". In: *The European Physical Journal C* 79.3 (Mar. 2019). doi: 10.1140/epjc/s10052-019-6650-6. url: https://doi.org/10.1140/epjc/s10052-019-6650-6.

[98] *Electron Photon Four Momentum Correction*. https://twiki.cern.ch/twiki/bin/viewauth/AtlasProtected/ElectronPhotonFourMomentumCorrection. Accessed: 2023-07-26.

[99] Stefan Schmitt. "Data Unfolding Methods in High Energy Physics". In: *EPJ Web of Conferences* 137 (2017). Ed. by Y. Foka, N. Brambilla, and V. Kovalenko, p. 11008. doi: 10.1051/epjconf/201713711008. url: https://doi.org/10.1051/epjconf/201713711008.

[100] Glen Cowan et al. "Asymptotic formulae for likelihood-based tests of new physics". In: *The European Physical Journal C* 71.2 (Feb. 2011). doi: 10.1140/epjc/s10052-011-1554-0. url: https://doi.org/10.1140/epjc/s10052-011-1554-0.

[101] F. James and M. Roos. "Minuit - a system for function minimization and analysis of the parameter errors and correlations". In: *Computer Physics Communications* 10.6 (1975), pp. 343–367. issn: 0010-4655. doi: https://doi.org/10.1016/0010-

4655(75)90039-9. url: https://www.sciencedirect.com/science/article/pii/0010465575900399.

[102] Georgiy Ivannikov. "Evaluation of Analysis Frameworks in the ATLAS Experiment at CERN and Design of an Optimized Framework for the Search and Determination of Properties of New Particles". Presented 02 Feb 2021. 2021. url: https://cds.cern.ch/record/2753951.

[103] The ATLAS Collaboration. "Luminosity determination in pp collisions at \sqrt{s} s = 8 TeV using the ATLAS detector at the LHC". In: *The European Physical Journal C* 76.12 (Nov. 2016). doi: 10.1140/epjc/s10052-016-4466-1. url: https://doi.org/10.1140/epjc/s10052-016-4466-1.

Appendix A

Systematic Uncertainties Plots

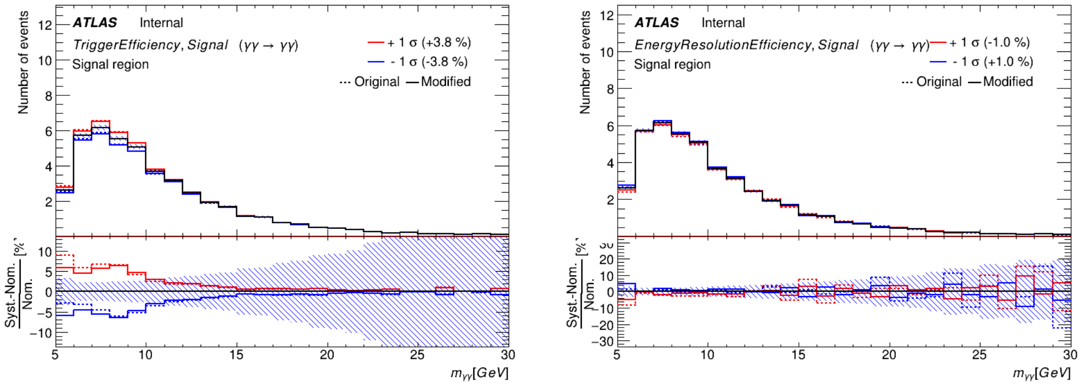

Figure A.1: Systematic uncertainties variation on the nominal signal for Trigger Efficiency (left) and Energy Resolution Efficiency (right)

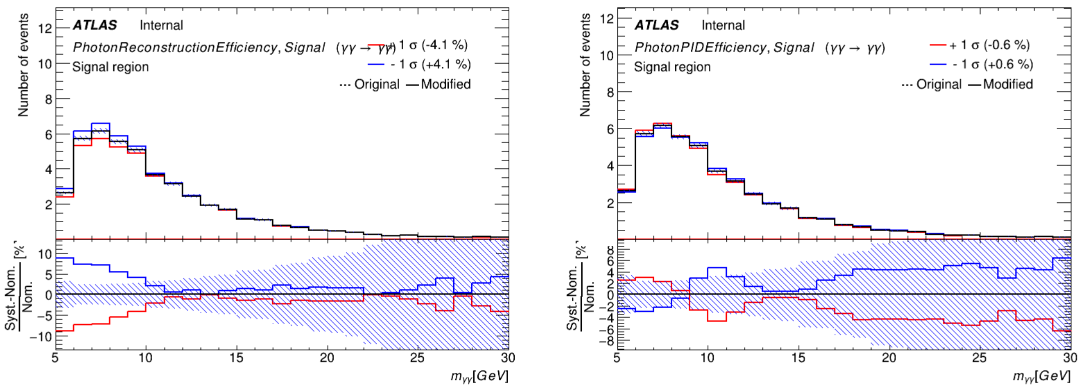

Figure A.2: Systematic uncertainties variation on the nominal signal for Photon Reconstruction Efficiency (left) and Photon PID Efficiency (right)

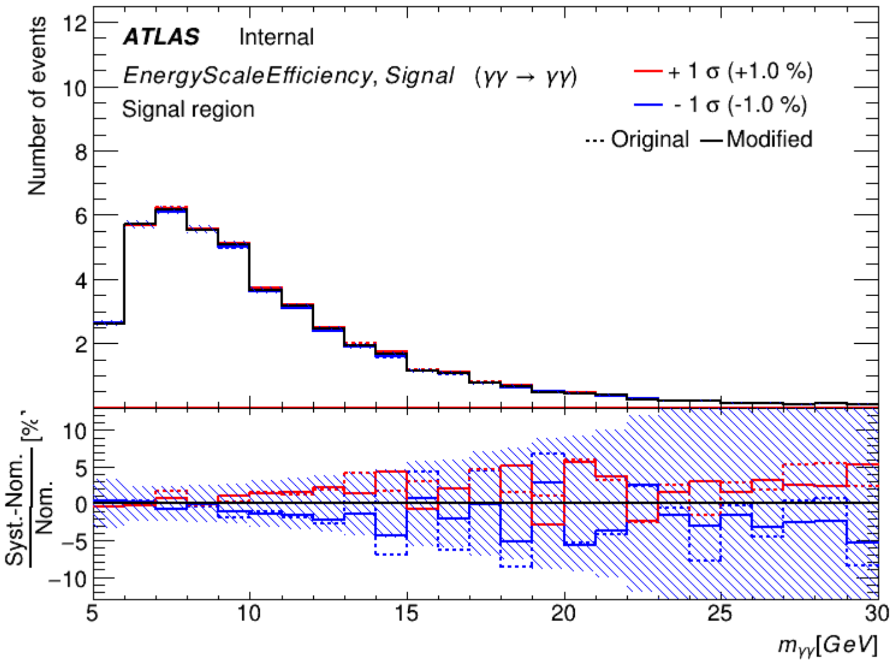

Figure A.3: Systematic uncertainties variation on the nominal signal for Energy Scale Efficiency